



# Contents

<b>1</b>	<b>Introduction to <math>\gamma</math>-Ray Astronomy .....</b>	<b>5</b>
1.1	Cosmic-ray physics .....	6
1.2	Acceleration mechanisms .....	7
1.2.1	Electric field acceleration .....	10
1.2.2	Stochastic acceleration .....	10
1.2.3	Diffusive Shock Acceleration .....	12
1.3	Production of $\gamma$ -rays .....	12
1.3.1	Bremsstrahlung .....	13
1.3.2	Inverse Compton scattering .....	15
1.3.3	Synchrotron emission .....	15
1.3.4	Curvature radiation .....	16
1.3.5	Matter-Antimatter annihilation .....	16
1.3.6	Hadronic collisions .....	17
1.4	$\gamma$ -ray Absorption mechanisms .....	18
1.4.1	Interaction with electrons: Compton effect .....	18
1.4.2	Pair production processes .....	18
1.4.3	The Extragalactic Background Light .....	18
1.5	Dark Matter and $\gamma$ -rays: WIMP annihilation .....	20
1.6	$\gamma$ -ray sources .....	23
1.6.1	Galactic sources .....	23
1.6.2	Extragalactic sources .....	30
1.6.3	Potential Dark Matter annihilation emission sources .....	35

<b>2</b>	<b>Detection of <math>\gamma</math>-rays .....</b>	<b>39</b>
<b>2.1</b>	<b>Space detectors .....</b>	<b>40</b>
2.1.1	Compton detectors .....	41
2.1.2	Pair production detectors .....	41
<b>2.2</b>	<b>Extensive Air Showers .....</b>	<b>44</b>
2.2.1	Electromagnetic Showers .....	44
2.2.2	Hadronic showers .....	47
2.2.3	Electronic showers .....	48
<b>2.3</b>	<b>Cherenkov radiation .....</b>	<b>48</b>
<b>2.4</b>	<b>Ground-based detectors .....</b>	<b>51</b>
2.4.1	Particle detectors .....	52
2.4.2	Atmospheric Cherenkov Telescopes .....	52
<b>3</b>	<b>The Cherenkov Telescope Array .....</b>	<b>59</b>
<b>3.1</b>	<b>Introduction .....</b>	<b>59</b>
<b>3.2</b>	<b>CTA Requirements and Performance .....</b>	<b>60</b>
<b>3.3</b>	<b>CTA Telescopes .....</b>	<b>64</b>
3.3.1	Large Size Telescope (LST) .....	64
3.3.2	Medium Size Telescope (MST) .....	67
3.3.3	Small Size Telescope (SST) .....	70
<b>3.4</b>	<b>Reconstruction and Analysis tools .....</b>	<b>72</b>
3.4.1	Monte Carlo simulations .....	72
3.4.2	Low level analysis: ctapipe .....	75
3.4.3	Science analysis: ctools .....	76
<b>4</b>	<b>Analysis chain of Single Telescope data and...</b>	<b>79</b>
<b>4.1</b>	<b>Introduction .....</b>	<b>79</b>
<b>4.2</b>	<b>The LST1 analysis chain overview .....</b>	<b>79</b>
4.2.1	Calibration .....	80
4.2.2	Image cleaning and parameterization .....	82
4.2.3	Reconstruction of energy and source position .....	84
4.2.4	$\gamma$ -hadron separation .....	85
<b>4.3</b>	<b>Sensitivity of the LST1 .....</b>	<b>87</b>
4.3.1	Reweighting .....	88
4.3.2	Cut optimization .....	90
4.3.3	Expected LST1 Performance .....	90

<b>4.4</b>	<b>Expectation-Maximization method for Hillas Parameters...</b>	<b>93</b>
4.4.1	The Expectation-Maximization algorithm .....	95
4.4.2	Comparison of EM without cleaning and tailcuts cleaning .....	97
<b>4.5</b>	<b>Results on real data</b>	<b>99</b>





During many centuries humanity has looked towards the skies and wondered about the mysteries of the universe. At first, with the naked eye, our ancestors measured the movements of astronomical objects and used them as calendars and guidance. We can say that modern Astronomy was born with the invention of the optical telescope by Galileo in 1609 AD. However, we were looking only to a small part of the universe, being only able to study the starts through the visible light they were emitting. Like an incomplete symphony where we can only listen to the melody of one instrument, our knowledge of the physics of the cosmos was purely limited to the thermal emission of stars. It was not until the first half of the XX century that we could start talking about the *multiwavelength* astronomy with the first infrared, radio, ultraviolet and X-ray observations. The most energetic part of the electromagnetic spectrum,  $\gamma$ -rays, were first detected in the 1960s. Along with the multiwavelength astronomy, other messengers from the sky were discovered: In 1912 the Austrian physicist Victor Hess found that the puzzling source of high levels of ionizing radiation in the atmosphere were actually charged particles coming from space. These particles were later named Cosmic Rays (CRs) by Millikan, and as will be explained later, their origin was thought to be closely related to the origin of  $\gamma$ -rays. The emission of this high energy radiation (above 100 keV), and the origin of such energetic particles as CRs were, could not be explained by means of thermal processes, thus other physical phenomena came into play, mostly involving interactions of relativistic particles.

The Astroparticle physics field studies the relation between  $\gamma$ -rays and CRs, combining astrophysics and particle physics, and includes other cosmic messengers, as neutrinos, to face unresolved problems like the origin and acceleration mechanisms of CRs, towards the completion of the cosmic symphony that is the Universe.

This chapter will be an overview of the basic concepts of CR and  $\gamma$ -ray physics, their production, acceleration and absorption, and their known sources of emission in

the universe.

## 1.1 Cosmic-ray physics

CRs are relativistic charged particles arriving to the atmosphere from the outer space. Their origin and the mechanisms that accelerate them to reach such high energies are still being debated. However, there are arguments pointing towards that they are accelerated in very violent events in the universe, such as supernova explosions. Several measurements strongly support that galactic CRs are in fact accelerated in Supernova Remnants (SNRs) [1], [2], [3].

As they are charged particles, they suffer from the effects of the magnetic fields (both interstellar and Earth magnetic fields) which divert their trajectories and make it very difficult to trace back their original direction. Nevertheless, they can interact with the medium close to their sources producing  $\gamma$ -rays through processes such as Inverse Compton (IC) scattering or neutral pion decay. Observing  $\gamma$ -rays, which travel in straight lines from their origin, can provide information on how and where do CRs are produced and interact with the medium.

The composition of CRs arriving to the Earth is mainly protons (86%), alpha particles (11%), electrons (2%) and other heavy nuclei (1%). We can distinguish between two types of cosmic-rays: Those reaching the Earth unaltered from their source, known as *primary CRs*; and those resulting from inelastic collisions of the primary CRs with the Interstellar Medium (ISM), called *secondary CRs*.

The spectrum of CRs is shown in figure 1.1. Mostly it can be described as a piecewise Power Law with a spectral index  $\gamma$  that changes along different regions of the spectrum [4]:

$$\frac{dN(E)}{dE} \propto E^{-\gamma} \quad (1.1)$$

Where N is the differential flux of CRs and E is the energy. The different parts that can be observed are:

- From few keV to less than 10 GeV: CRs are produced locally in solar flares and coronal mass ejections from the Sun [5], with a spectral index  $\sim 5$  [6].
- Up to the *knee* (below  $10^6$  GeV): CRs follow a simple power law with spectral index  $\gamma \sim 2.7$ . In this region CRs are considered to have a galactic origin, accelerated in SNRs.
- From the *knee* to the *second knee* (at  $10^8$  GeV) the spectral index becomes  $\sim 3.1$ .
- Between the *second knee* (at  $10^8$  GeV) and the *ankle* the spectral index is  $\sim 3.3$ .
- Energies above the *ankle* ( $\sim 10^9$  GeV): CRs coming from extragalactic sources are predominant, with a hardening in the spectrum back to an index  $\sim 2.7$ . At

such high energies, particles are no more confined by galactic magnetic fields so they travel with their trajectories almost unperturbed [7], allowing to estimate their direction. These kind of very energetic CRs can be produced in Active Galaxy Nuclei (AGN), Gamma Ray Bursts (GRBs), radio galaxy lobes and intra-cluster medium in galaxy clusters [8].

- At energies above  $\sim 4-5 \times 10^{10}$  GeV a strong suppression is observed, interpreted as the GZK cutoff, which sets a theoretical upper limit on the energy carried by CR from distant sources.

As already mentioned, it is possible to differentiate two CR origins: galactic CR and extragalactic CR. Below the *knee*, CRs are produced in galactic accelerators (SNRs) and their maximum energy can be considered a limit on the acceleration that is possible to gain from these kind of objects. CRs with energies above the *ankle* are thought to come from extragalactic sources and so, their higher acceleration must come from different phenomena, more violent and energetic (AGN, GRBs, etc.). The Larmor radius defines the curved trajectory of charged particles moving perpendicular to a magnetic field. The "Hillas condition" [10] sets a minimum requirement for the accelerators to reach certain energies, stating that a necessary condition to accelerate particles to ultrahigh energy is that of confinement, meaning that they can stay in the acceleration region as long as their Larmor radius is smaller than the size of the accelerator. For energies over the *ankle*, the Larmor radius starts to become larger than galactic scales, hence extragalactic CRs propagate almost linearly and unaffected by the galactic magnetic field, while galactic (less energetic) CRs propagate diffusively through the ISM. Figure 1.2 shows the Hillas diagram, where different source classes are presented as function of their characteristic size and magnetic field strength.

The transition in the spectrum between galactic and extragalactic accelerators, although still not well understood, can be explained by the effect of the galactic magnetic field in the trajectories of CRs, and the effect of galactic wind termination shocks as a re-acceleration process [4].

The chemical composition of galactic CRs is very similar to that of the Solar System (see figure 1.3), suggesting a similar origin (stellar interiors) but with some discrepancies in certain elements. The most noticeable difference regards Li, Be and B, and to a lesser extent sub iron elements Mn, Cr, V, Ti and Se. The abundances of these elements are small in stars because they are rapidly consumed by nuclear reactions, but they are present in secondary CRs due to *spallation* of carbon and oxygen nuclei [11] and other abundant heavy nuclei as Fe and Ni [12].

## 1.2 Acceleration mechanisms

Acceleration mechanisms take place in astrophysical plasmas which in general consists on thermal plasma components, a magnetic field and non-thermal distributions of fast particles. Within the plasma, turbulence and plasma waves take place, having an important role in particle acceleration. The mechanisms that accelerate CRs to the huge energies observed, that can reach up to  $10^{20}$  eV are still a topic of debate and

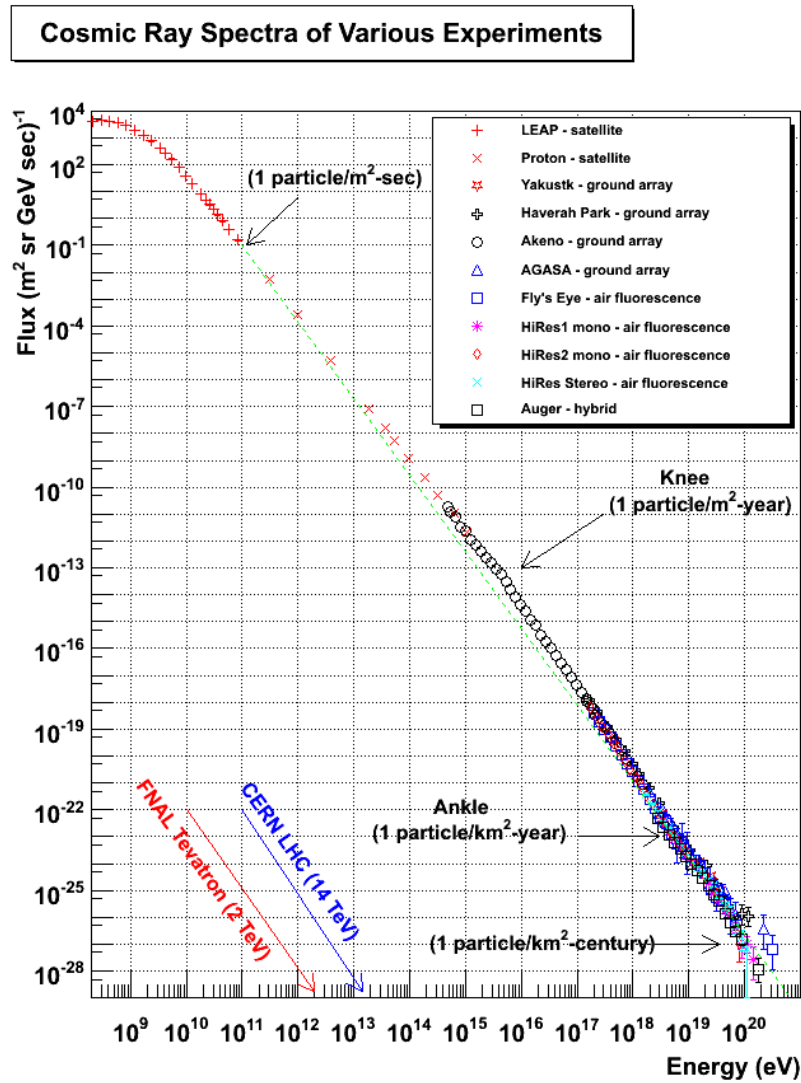


Figure 1.1: Cosmic ray spectrum from [9] built with data from several experiments. Red and blue lines represent the energy spectrum covered by Tevatron and LHC accelerators. Green line shows the fit to a power law with spectral index 2.7.

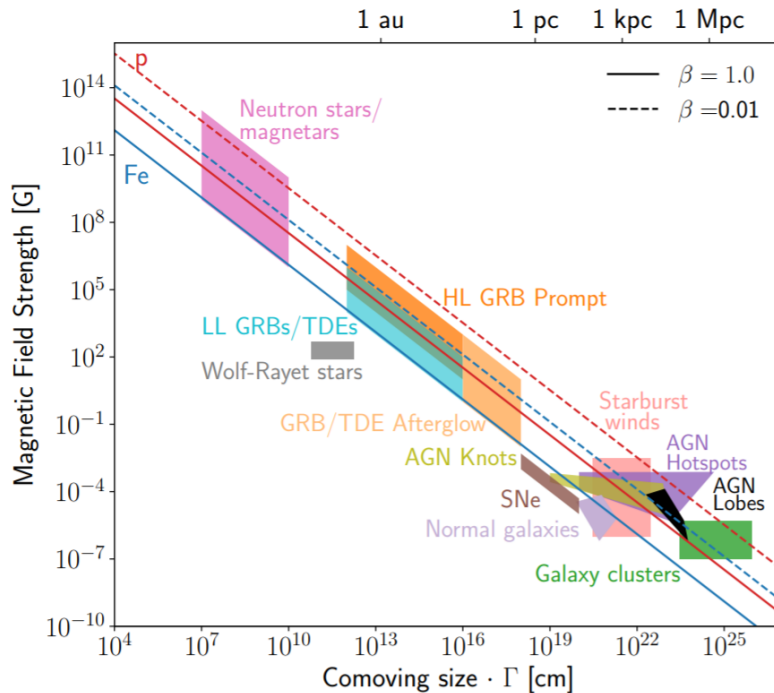


Figure 1.2: Hillas diagram, from [8]. Source classes as a function of their characteristic radius  $R$ , given as the comoving size of the source times the Lorentz factor  $\Gamma$ , and the magnetic field  $B$  in the comoving frame of the source. Solid (dashed) lines indicate the product of  $B \times R$  beyond which confinement of protons (red) and iron (blue) nuclei with energy  $10^{20}$  eV are possible for outflows with velocity  $\beta_{ish} = 1$  ( $\beta_{ish} = 0.01$ ).

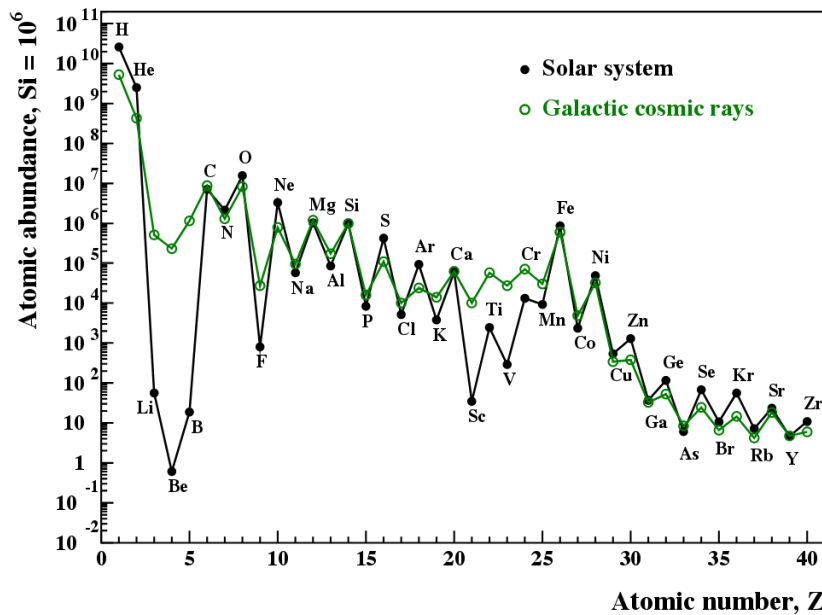


Figure 1.3: Abundances of elements of galactic CRs compared to the Solar System, from [12].

research in the high energy astrophysics field. Several particle acceleration mechanisms are proposed to explain the CR spectrum, which should be able to achieve the highest energies measured for CR and reproduce the spectral shape of a power law with an index  $\sim 2.7$ , and the abundances of elements measured [13], [14], [15].

### 1.2.1 Electric field acceleration

Electric fields parallel to magnetic fields can accelerate charged particles and can arise during magnetic field reconnection (the breaking and reconnecting of oppositely magnetic field lines in a plasma). Because ideal Magnetohydrodynamics (MHD) of plasmas require the parallel component of electric field to be null  $E_{\parallel} = 0$ , non-ideal MHD effects are needed to explain the development of  $E_{\parallel} = 0$ , such as resistivity or inertial effects on Alfvén waves (a type of MHD wave where ions oscillate in response to a restoring force provided by an effective tension on the magnetic field lines) [15]. This kind of acceleration is believed to take place in magnetic reconnection of the Earth's magnetotail, accelerating auroral electrons; Also, reconnection in pulsar gaps (see section 1.6.1) could produce this kind of acceleration which should involve large oscillations in  $E_{\parallel}$ .

### 1.2.2 Stochastic acceleration

Stochastic acceleration is also known as *Second Order Fermi acceleration* or simply *Fermi process*. This idea was developed by Enrico Fermi in 1949 [16] as a mechanism

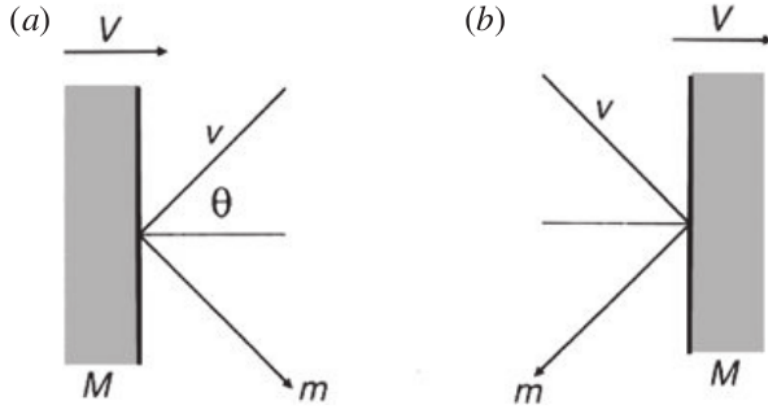


Figure 1.4: Collision of a particle of mass  $m$  with velocity  $v$  against a cloud of mass  $M$  and velocity  $V$ . a) head-on. b) head-tail. From [17].

to explain acceleration of galactic CRs. The basic concept is that particles can gain velocity after being reflected several times by randomly moving magnetized clouds in the ISM. Fermi showed that after a characteristic time  $\tau_{esc}$ , the spectrum of the accelerated particles would follow a power law. If the particle is moving with a pitch angle  $\theta$  (the angle between the particle velocity vector and the local magnetic field), the gain in energy after a collision with a cloud moving with velocity  $V$  will be [17]:

$$\Delta E = E \left[ \frac{2V \cos \theta}{c^2} + 2 \left( \frac{V^2}{c} \right) \right] \quad (1.2)$$

Where  $E$  is the energy of the particle before the collision. Between collisions the particle will be moving inside a plasma and will suffer scattering due to hydrodynamic waves, the total gain in energy has to be averaged over a set of random  $\theta$  angles. The probability of a collision is proportional to the relative velocities of the particle ( $v$ ) and the cloud ( $V$ ). If  $v \approx c$  the probability of a head-on collision  $P \propto 1 + (V/c)\cos\theta$  is slightly higher than the probability of head-tail collision  $P \propto 1 - (V/c)\cos\theta$  (see figure 1.4) hence the total, averaged in all  $\theta$  angles between 0 and  $\pi$ , gain in energy will be positive:

$$\left\langle \frac{\Delta E}{E} \right\rangle = \frac{8}{3} \left( \frac{V}{c} \right)^2 \quad (1.3)$$

Being the increase in energy *second order* proportional to  $V/c$ . However, this process cannot be the main source of particle acceleration: the velocities of interstellar clouds in the ISM is too low ( $V/c \simeq 10^{-4}$ ), the mean free path of CRs in the ISM is too high (the number of collisions would be  $\sim 1\text{yr}^{-1}$ ) and the particles should be

injected in the acceleration region with already high velocities (this is known as the *injection problem* and actually is present in every acceleration mechanism).

### 1.2.3 Diffusive Shock Acceleration

The most popular acceleration mechanism in astrophysical plasmas, which is believed to take place in SNRs (the best candidates for galactic CR production) is known as Diffusive Shock Acceleration (DSA) or *First Order Fermi acceleration*. This mechanism revisits the original idea formulated by Fermi of particles colliding with randomly moving "magnetic mirrors" in the ISM, but with all the collisions happening always head-on. For example, when two clouds are approaching each other and the particle bounces back and forth [15]. This process can happen in the presence of strong supersonic shock waves propagating through a diffuse medium, like the ones produced after a Supernova (SN) explosion (see figure 1.5). A flux of relativistic particles is assumed to exist in both sides of the shock, which are moving much faster than the latter. Each time a particle crosses to one side or the other, their velocity becomes isotropic in the frame of reference of the moving fluid. Since on every crossing the particle encounters gas moving towards it at a velocity proportional to the shock velocity ( $U$ ), which for a fully ionized plasma composed by monoatomic perfect gas is  $\sim 3/4U$  [17] it will receive a boost in energy of the order  $\sim U/c$ . That is why this process is called *first order* in counterpart to the classical second order Fermi acceleration where the energy gain in each collision is proportional to  $\sim (U/c)^2$ . DSA is able to predict a spectral index of  $\sim 2$ , very close to the observed for galactic CR. Also, is the only acceleration mechanism efficient enough to transfer the observed amount of energy in SNR to particles. On the other hand, it exists an upper limit on the maximum energy that a particle can gain through DSA which is set to  $\sim 10^{14}$  eV [18], so is still not enough to explain the full CR spectrum, which reaches up to  $\sim 10^{20}$  eV.

## 1.3 Production of $\gamma$ -rays

Although CRs have been known for many decades, it is difficult to make conclusions about their origin and acceleration mechanisms. As they are charged particles, their trajectories are deflected while travelling through the ISM, hence their incoming direction does not point towards the source of origin. Nevertheless, CRs can interact with the medium producing  $\gamma$ -rays through several mechanisms, which reach the Earth undeflected, offering a way to indirectly study CR origin, acceleration and diffusion in the ISM. When we talk about radiation production, we can distinguish between two main mechanisms which involve very different physical phenomena: thermal and non-thermal processes. A large fraction of the low energy radiation emitted by stars or interstellar dust is produced by thermal processes following a black body spectrum. To produce radiation as energetic as  $\gamma$ -rays a temperature of the order of  $10^{10}$  K would be needed, which is something that was only reachable in the Big Bang conditions. Therefore, to understand the production of  $\gamma$ -rays we must study

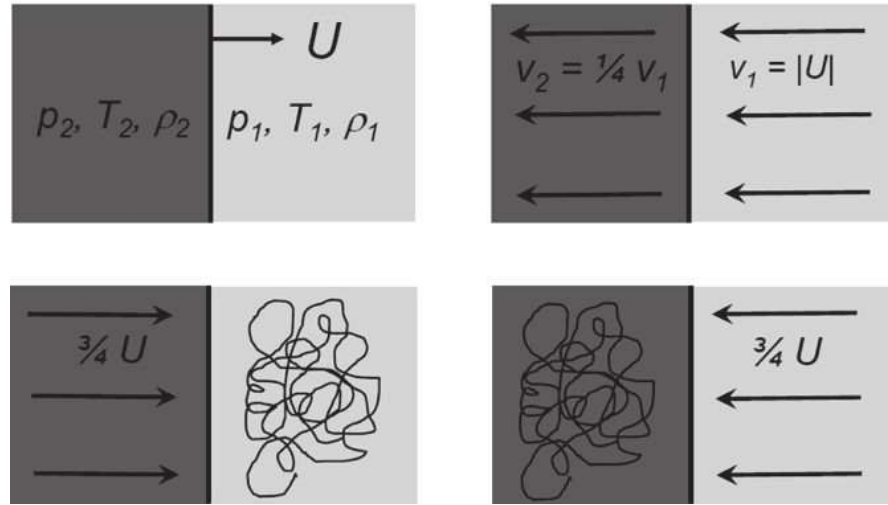


Figure 1.5: Scheme of the *Diffuse shock acceleration* from [17]. *Upper left*. Observer frame: A diffusive shock is propagating at velocity  $U$ . *Upper right*. Frame where the shock front is at rest. The velocities of the gas in both sides of the front, assuming is fully ionized, have a ratio of 4. *Lower left*. Frame of reference where the upstream gas is at rest, the distribution of velocities of the high energy particles is isotropic. *Lower right* Same case as previous, but in the reference frame of the downstream gas.

the so called *non-thermal universe*, where radiation is produced by interactions of relativistic particles moving in electromagnetic fields. In general,  $\gamma$ -rays are produced in two kinds of scenarios: leptonic emission (produced mainly by electrons) and hadronic emission (produced mainly by protons). Which one of those is dominant in astrophysical particle accelerators is still a subject of debate and will be commented in section 1.6 about  $\gamma$ -ray sources. In this section a brief summary on the different  $\gamma$ -ray production mechanisms (see figure 1.6) is given.

### 1.3.1 Bremsstrahlung

From the German "braking radiation", the bremsstrahlung process occurs when a charged particle is decelerated by the electric field produced by an atomic nucleus. While their trajectory is deflected, the particle emits electromagnetic radiation with amplitude proportional to the magnitude of the deceleration suffered. The differential cross section for a particle of charge  $e$ , mass  $m$ , carrying an energy  $E_e$  to radiate a photon between energies  $E_\gamma$  and  $E_\gamma + dE$  when interacting with the Coulomb field is:

$$\sigma(E_e, E_\gamma) dE_\gamma = 4\alpha Z^2 r_e^2 \frac{dE_\gamma}{E_\gamma} F(E_e, \nu) \quad (1.4)$$

Where:

$$F(E_e, \nu) = [1 + (1 - \nu)^2 - \frac{2}{3}(1 - \nu)] \left[ \ln \left( \frac{2E_e}{m_e c^2} \frac{1 - \nu}{\nu} \right) - \frac{1}{2} \right] \quad (1.5)$$

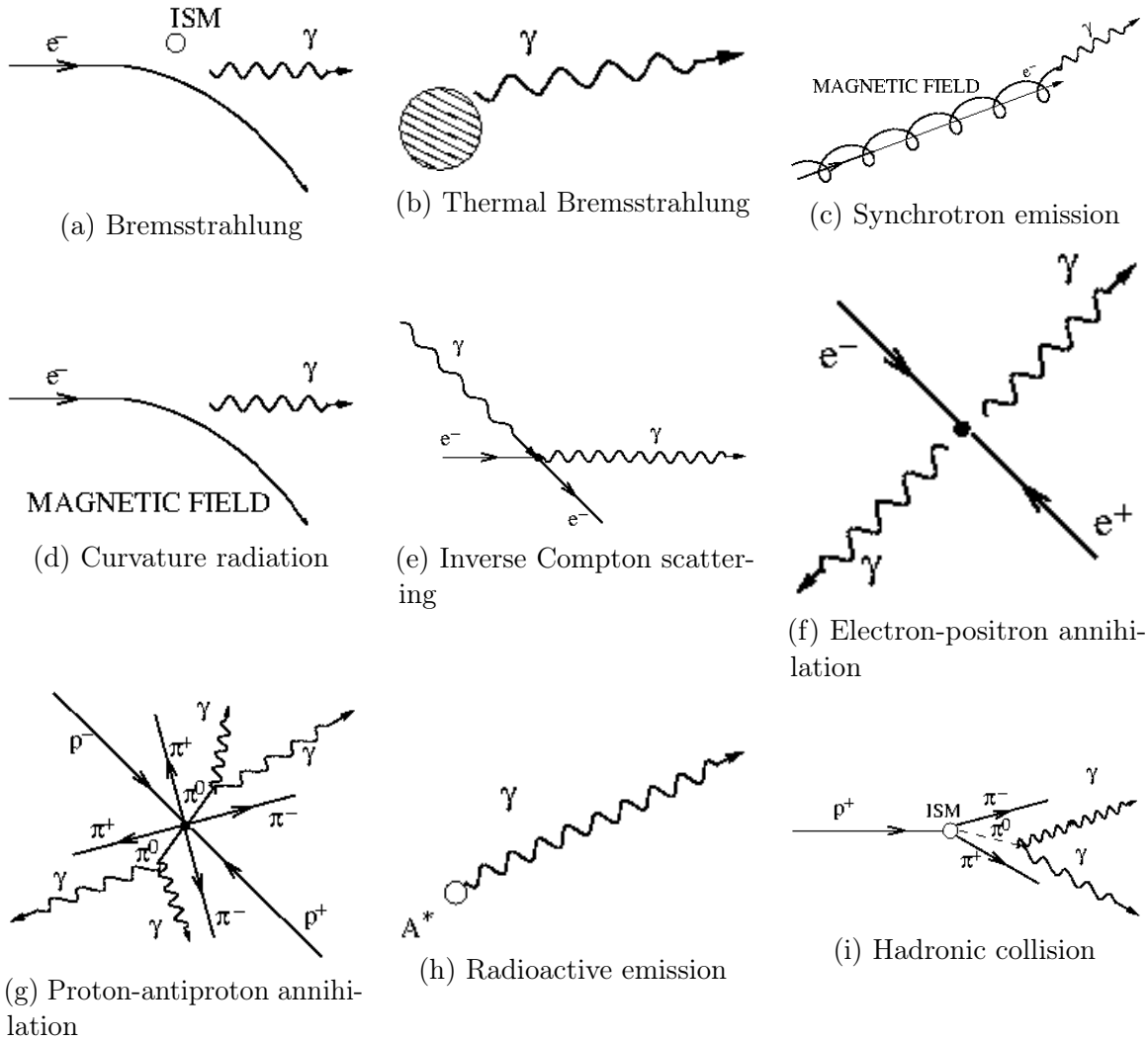


Figure 1.6: Diagrams of the different  $\gamma$ -ray production processes. Figures extracted from [22].

Being  $\alpha$  the fine structure constant and  $\nu = E_\gamma/E_e$  the fractional energy carried by the photon [19]. From equations 1.4 and 1.5 it can be seen that the acceleration suffered by the particle is  $\propto Ze^2/m$ , then while any charged particle can suffer bremsstrahlung, it is going to be much more efficient for electrons than for protons which have a higher mass. The photons emitted will have a continuum spectrum with energies of the same order of the particle, which for cosmic electrons in a gas is going to be a power law [20]. Bremsstrahlung is mainly efficient under high-density conditions. It takes place in gaseous nebulae that contain ionized gas, such as SNR, and in the intracluster medium of galaxy clusters [21].

### 1.3.2 Inverse Compton scattering

IC scattering is the inelastic interaction where a relativistic charged particle transfer a considerable amount of energy to a photon. In the frame of reference of the electron the photon will suffer an "energy boosting" [20]. The energy of the scattered particle is  $E = \Gamma mc^2$ , where  $\Gamma$  is the Lorentz factor, and we can define the parameter  $\alpha = h\nu/mc^2$ , where  $\epsilon = h\nu$  is the initial energy of the photon. We can differentiate between two regimes depending on the initial energy of the photon:

- *Thomson regime*: For low values of  $\alpha$ , particle recoil can be neglected and the energy of the photon after the scattering will be:

$$E_\gamma \simeq \frac{4}{3}\epsilon\gamma^2 \quad (1.6)$$

- *Klein-Nishina regime*: For large values of  $\alpha$ , particle recoil is significant and in this case the energy of the photon after the interaction is:

$$E_\gamma \simeq \frac{1}{2}E \quad (1.7)$$

Photons from the Cosmic Microwave Background (CMB) are typical targets for IC scattering, together with synchrotron photons or photons thermally emitted by astrophysical sources. This mechanism is predominant in Very High Energy (VHE)  $\gamma$ -ray emitters, like in the jets of AGN and TeV blazars. The spectrum of the photons boosted by this process will follow a power law related to that of the population of relativistic electrons in the medium ( $\propto E_e^{-\Gamma_e}$ ):

$$\frac{dN_\gamma}{dE} \propto E^{-\frac{(\Gamma_e+1)}{2}} \quad (1.8)$$

### 1.3.3 Synchrotron emission

Synchrotron emission is produced when a charged particle is moving in a magnetic field. The particle will follow an spiral path, with constant velocity along the field lines, while being accelerated towards the center of its orbit. The particle will suffer energy losses that for relativistic particles follow a continuum spectrum [20] with a critical frequency  $w_c$  at which the maximum power is emitted:

$$w_c = \frac{3eB}{2mc}\Gamma^2 \sin\phi \quad (1.9)$$

Where  $e$  and  $m$  are the charge and mass of the particle,  $B$  is the magnetic field,  $\Gamma$  is the Lorentz factor and  $\phi$  is the pitch angle bewteen the directions of the magnetic field and the particle. The total energy loss is given by

$$-\frac{1}{c} \left( \frac{dE}{dt} \right) = \frac{2e^4}{3m^2c^4}\Gamma^2 B^2 erg cm^{-1} \quad (1.10)$$

Following 1.10, the power emitted is inversely proportional to the mass of the particle so it will be comparatively much more efficient for electrons than for protons.

Synchrotron radiation of ultra-relativistic particles is the most important contribution to the non-thermal universe (radio, X-rays...). According to 1.9 the production of High Energy (HE)  $\gamma$ -rays will require too high values of B and  $E_e$ , but regions emitting synchrotron radiation contain relativistic electrons capable of IC scattering [23], which will acquire much higher energies.

#### **1.3.4 Curvature radiation**

In presence of very strong magnetic fields, of the order of  $10^{11}$ - $10^{13}$  G, electrons and positrons will be forced to follow a trajectory parallel to the magnetic field lines. Since the lines are curved, with a curvature radius  $\rho_c$ , the particle will emit *curvature radiation* in the direction of movement, with a characteristic photon energy [24]:

$$E_c = \frac{3}{2} \Gamma^3 \frac{\hbar c}{\rho_c} \quad (1.11)$$

Typical environment where curvature radiation takes place are the surroundings of pulsars, due to the extremely high magnetic fields close to their surfaces. An electron with an energy of 10 TeV moving along a field line with a curvature of  $10^8$  cm, which is typical for pulsars, emits photons of energy  $\approx 2.5$  GeV [19].

#### **1.3.5 Matter-Antimatter annihilation**

Matter-antimatter pair annihilation processes can produce  $\gamma$ -rays. The most common case is electron-positron annihilation ( $e^-e^+ \rightarrow 2\gamma$ ). If the two particles are at rest, they produce  $\gamma$ -rays with energy equal to their masses (0.511 MeV). If the particles are thermalized but with low energies, such as the electrons of the ambient gas/plasma, they form the unstable state called positronium which can annihilate into 3 photons forming a continuum [25]. For relativistic particles interacting in-flight, the annihilation cross section is:

$$\sigma_A = \frac{\pi r_e^2}{\Gamma} [\ln(2\Gamma) - 1] \quad (1.12)$$

Where  $\Gamma = E_e/m_e c^2$  is the Lorentz factor of the positrons and  $r_e = e^2/m_e c^2 = 2.82 \times 10^{-13}$  cm is the classical radius of the electron. The result of the interaction is the emission of two photons with a continuum of energies. At very high energies, the cross section of equation 1.12 is quite low, leading to very high mean free paths and long lifetimes for the positrons, which typically will be affected by other processes before annihilating. Positrons can lose energy gradually without escaping the galaxy until the cross section is high enough and they annihilate [19].

Proton-antiproton annihilation can also produce  $\gamma$ -rays indirectly by the production of neutral pions  $\pi^0$  which decay into  $\gamma$ -rays later on [26]. In theory, antiprotons can

be produced by interactions of protons with matter, but this process is much less efficient than the direct production of  $\pi_0$  mesons [20] so the production of  $\gamma$ -rays this way is considered marginal.

### 1.3.6 Hadronic collisions

While most of the processes described above were dominated by electron interactions (leptonic scenario), we now focus on the processes that constitute the hadronic contribution to the production of  $\gamma$ -rays, which are believed to be the dominant  $\gamma$ -ray production processes in SNRs and AGN.

Protons accelerated to relativistic energies in extreme environments, such as strong magnetic fields or jets, can collide with other hadrons producing mesons, kaons and hyperions. The most common interaction is the proton-proton collision to produce pions ( $\pi$  mesons):

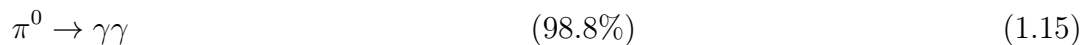


With a threshold energy of the proton, which is the minimum kinetic energy the pair of protons must have in the collision to produce the meson:

$$E_p = 2m_{\pi^0}c^2 \left( 1 + \frac{m_{\pi^0}}{4m_p} \right) \simeq 280 \text{ MeV} \quad (1.14)$$

Where  $m_{\pi^0} = 134.97$  MeV is the mass of the  $\pi_0$ -meson and  $m_p = 938.27$  MeV is the mass of the proton [25].

Neutral pions  $\pi^0$  decay into  $\gamma$ -rays within a short lifetime  $\tau = 8.6 \cdot 10^{-17}$ s through the channels:



Then the energy of the photons emitted by the  $\pi^0$  peaks at  $E_\gamma = m_{\pi^0}c^2/2 \simeq 67.5$  MeV, but in the laboratory frame of reference this energy depends on the energy of the  $\pi^0$  and the angle of the proton trajectory with respect to the  $\pi^0$  allowing the emitted  $\gamma$ -rays to reach very high energies.

The collision of protons can also produce charged mesons, which can decay into neutrinos  $\nu_{e,\mu}$  with a spectrum similar to that of the photons [25]. Finding a correlation between  $\gamma$ -ray emission and astrophysical neutrinos from a certain source would be an unequivocal way to differentiate between leptonic and hadronic emission. Their spectrum shape and the lack of correlation with X-rays could be other ways to distinguish hadronic and leptonic emission.

## 1.4 $\gamma$ -ray Absorption mechanisms

Because  $\gamma$ -rays are very energetic, they can travel long distances without being altered. However there are mechanisms that can produce losses of energy of astrophysical  $\gamma$ -rays or their total absorption, altering the spectrum that is measured from Earth. These mechanisms can be divided in  $\gamma$ -matter interactions and  $\gamma - \gamma$  processes.

### 1.4.1 Interaction with electrons: Compton effect

Compton effect is produced when a photon is scattered by an electron, shifting the wavelength of the photon to lower energies. The shift in the wavelength goes like:

$$\lambda' - \lambda = \frac{h}{m_e c} (1 - \cos\theta) \quad (1.17)$$

Where  $\lambda'$  is the wavelength of the scattered photon,  $\lambda$  the wavelength of the incident photon and  $\theta$  is the scattering angle. In the standard ISM density of 1 atom per  $\text{cm}^{-3}$ , for distances of  $\sim 10$  kpc, the mean free path for photons of 1 MeV would be of 2 Mpc, thus the Compton effect is negligible. In hot dense plasmas however, where densities are much higher, the effect can be quite important [19].

This effect is used in Compton  $\gamma$ -ray telescopes such as described in section 2.1.1.

### 1.4.2 Pair production processes

Pair production is the opposite process to pair annihilation, where two photons interact to produce a pair  $e^-e^+$ . This is the most common absorption mechanism for HE and VHE photons. A  $\gamma$ -ray with energy  $\epsilon_1$  which collides with a target photon with energy  $\epsilon_2$  will produce a pair of particles of mass  $m$  if  $\epsilon_1$  is greater than a threshold energy:

$$\epsilon_t = \frac{2m^2c^4}{\epsilon_2(1 - \cos\theta)} \quad (1.18)$$

where  $\theta$  is the angle between the trajectories of the photons. In astrophysics, this process occurs when energetic photons traveling through the Universe encounter a radiation field, such as the CMB ( $\epsilon_t \approx 4 \times 10^{14}\text{eV}$ ) or the light of stars ( $\epsilon_t \approx 4 \times 10^{11}$ ). Even though photon-photon collisions are not generally frequent, because the spatial density of the target photons is not very large ( $\approx 400 \text{ cm}^{-3}$  for the CMB radiation  $n$  and  $\approx 5 \times 10^{-3}\text{cm}^{-3}$  for extragalactic starlight) the attenuation effect can be appreciated, specially for VHE photons coming from high redshifts. This process also occurs when  $\gamma$ -rays penetrate the atmosphere and are absorbed, leading to the production of Extensive Air Showers (EAS), which are the key for ground based  $\gamma$ -ray detectors and will be explained in section 2.2.

### 1.4.3 The Extragalactic Background Light

The Extragalactic Background Light (EBL) is the accumulated radiation in the universe due to star formation processes and the emission from AGNs. It is a

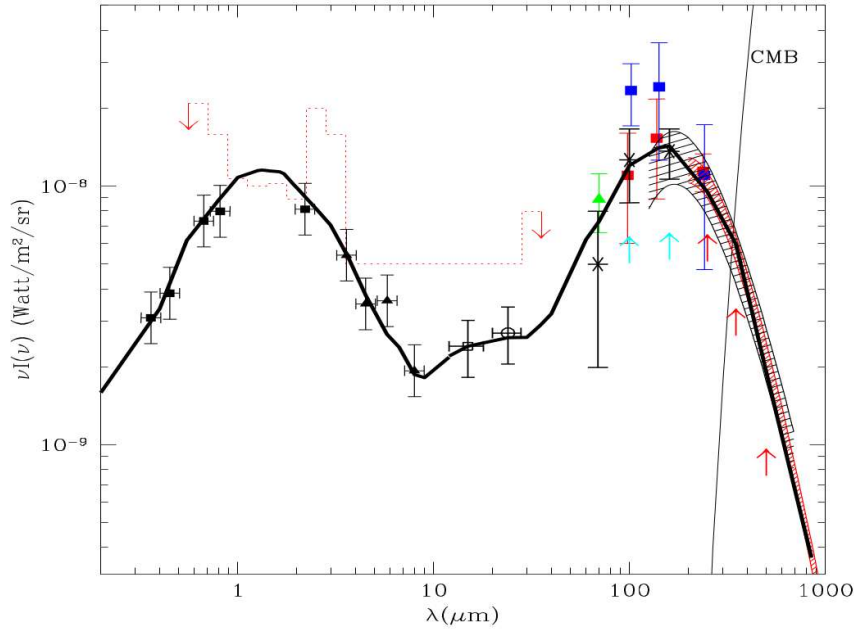


Figure 1.7: Best fit model prediction of the EBL energy density from [28] (thick black line).

fundamental constituent of the universe that permeates it uniformly. The direct measurement of the EBL is a very difficult task, mainly because of the foreground light from the Solar System. Phenomenological approaches try to predict an EBL model based on galaxy formation and evolution during the history of the universe and several direct measurements have been done from the far infrared to the optical, to set constraints on the density and spectrum of the EBL [27]. Besides the different proposed models, it is accepted that the energy density is characterized by two peaks, as seen in figure 1.7. The first peak, found at  $\sim 1\mu\text{m}$  is the stellar component and the second peak at  $\sim 100\mu\text{m}$  is the dust component, the light re-emitted by cosmic dust.

EBL photons are a typical target for  $\gamma$ -rays to produce pair production. The attenuation to the spectrum of a  $\gamma$ -ray source at the energy  $E$  follows the form:

$$F = F_0(E) e^{\tau(E,z)} \quad (1.19)$$

Where  $F$  is the observed flux and  $F_0$  the intrinsic spectrum of the  $\gamma$ -ray source,  $\tau$  is the optical depth which depends on the energy and the redshift  $z$  (as shown in figure 1.8). As a consequence of this dependence, for each energy there is a distance (redshift) at which the universe is optically thick to  $\gamma$ -rays, when the optical depth is equal to 1. The spectrum of the  $\gamma$ -ray source will suffer a cutoff at the energy that reaches the threshold optical depth, which decreases rapidly with redshift. Observations of this effect in distant sources in the VHE range is very useful to characterize the EBL in

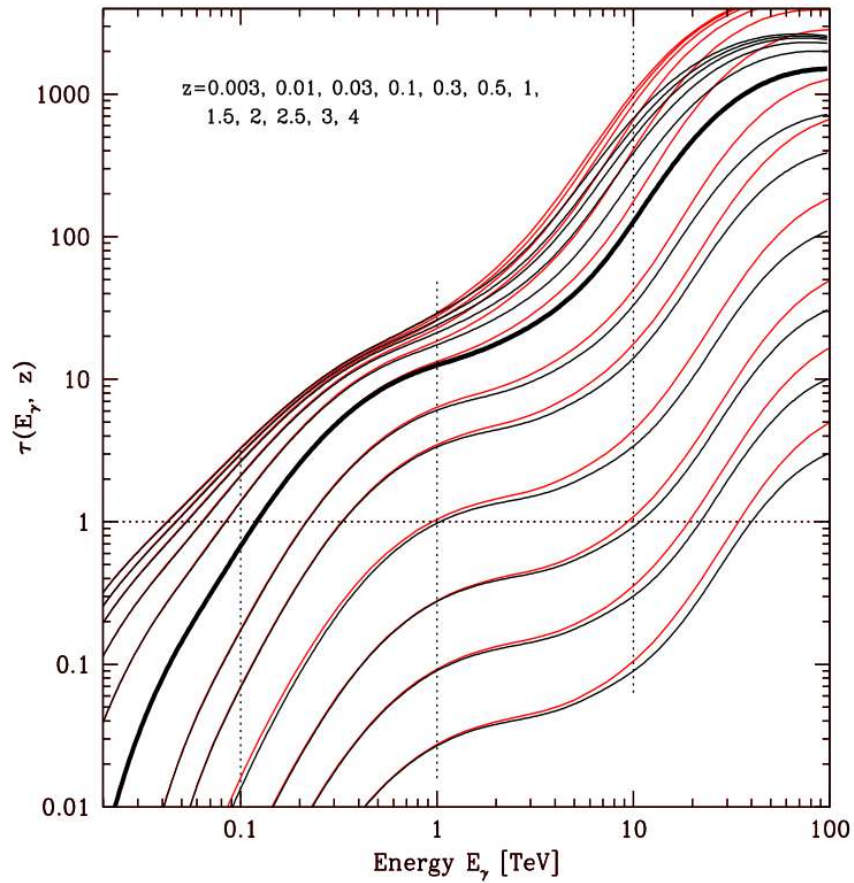


Figure 1.8: Optical depth due to photon-photon collision as a function of energy for different redshift values, from [28].

an indirect way, comparing the expected spectrum to the measured one [29].

## 1.5 Dark Matter and $\gamma$ -rays: WIMP annihilation

The nature of Dark Matter (DM) is one of the most important open questions in modern physics. There are many probes that suggest that the universe is composed of something more than the visible matter: From the Fritz Zwicky measurements on the velocity dispersion in the Coma galaxy cluster [30] and the rotation curves of high-luminosity spiral galaxies obtained by Vera Rubin [31], to the much more modern measurements of the CMB by Planck [32], all of them point towards the existence of a non-baryonic type of matter which only interacts gravitationally with Standard Model (SM) particles. Cosmological simulations and cosmological probes such as Wilkinson Microwave Anisotropy Probe (WMAP) point to a hierarchical structure formation of the universe, where small structures were formed first and then merged to the larger. To accomplish for that model, if DM is formed by particles, they should

be non-relativistic (Cold dark matter) which decoupled from the thermal equilibrium in the early universe. Hot dark matter models, where DM particles would be still largely relativistic (like neutrinos), would lead to large structures forming first and fragment out later [33].

With these assumptions, we can derive the number density evolution of DM particles today. In the early universe, DM and SM particles were in thermal equilibrium with the photon bath emitted in the Big Bang, and reactions of annihilation and formation of particles were taking place at the same rate. While the universe expanded, these reactions started to be slower than the rate of expansion, so these particles *decoupled* from the thermal bath. This is the moment of *freeze-out*. Before that, particles had an equilibrium number density  $Y_{eq}$ , which evolves with time while the universe keep expanding. For DM and using the Boltzmann equation, the number density evolution  $dY/dx$  follow the equation:

$$\frac{dY}{dx} = -\frac{xs\langle\sigma v\rangle}{H(m)}(Y^2 - Y_{eq}^2) \quad (1.20)$$

Where  $m$  is the mass of the DM particle,  $x$  is the scaled time variable  $x = m/T$  being  $T$  the temperature of the photon bath at the moment of freeze out,  $s$  is the total entropy density of the universe,  $Y$  is actually defined as the number density of DM rescaled to  $s$  ( $Y = n/s$ ) to account for the expansion of the universe,  $\langle\sigma v\rangle$  is the velocity averaged cross section for the reaction of DM particles annihilating into SM particles and  $H(m)$  is the Hubble rate (which defines the rate of expansion of the Universe) defined as  $H(x) = H(m)/x^2$ .

While the annihilation rate of the particles is higher than the expansion rate of the universe ( $\Gamma \gg H$ ), the number density  $Y$  remains close to  $Y_{eq}$ . After the moment of freeze-out  $x_f$  ( $\Gamma \ll H$ ), the number density will remain almost constant as shown in figure 1.9.

Following the approach of [34], after freeze-out, the evolution of DM abundance can be written as:

$$\frac{dY}{dx} \approx -\frac{\lambda}{x^{n+2}}, \text{ where } \lambda = \frac{\langle\sigma v\rangle_0 s_0}{H(m)} \quad (1.21)$$

To define  $\lambda$  the dependency of the cross section and entropy with  $x$  was pulled out through the change of variables:  $\langle\sigma v\rangle = \langle\sigma v\rangle_0 x^{-n}$  and  $s = s_0 x^{-3}$ , where  $n$  is an exponent which depends on details of the particle physics model. Taking  $n=0$ , the DM abundance today would be  $\simeq x_f/\lambda$ . There is no SM particle which can explain the cosmic density of DM measured today  $\Omega_\chi$ , but if we consider a weak interacting particle in the weak mass regime ( $m_\chi \sim 100$  GeV), the correct DM density measured by Planck and WMAP arises naturally:

$$\Omega_\chi = \frac{m_\chi s_{today} Y_{today}}{\rho_{cr}} \rightarrow \Omega_\chi h^2 \sim \frac{10^{-26} cm^3/s}{\langle\sigma v\rangle} \simeq 0.1 \left(\frac{0.01}{\alpha}\right)^2 \left(\frac{m_\chi}{100 GeV}\right) \quad (1.22)$$

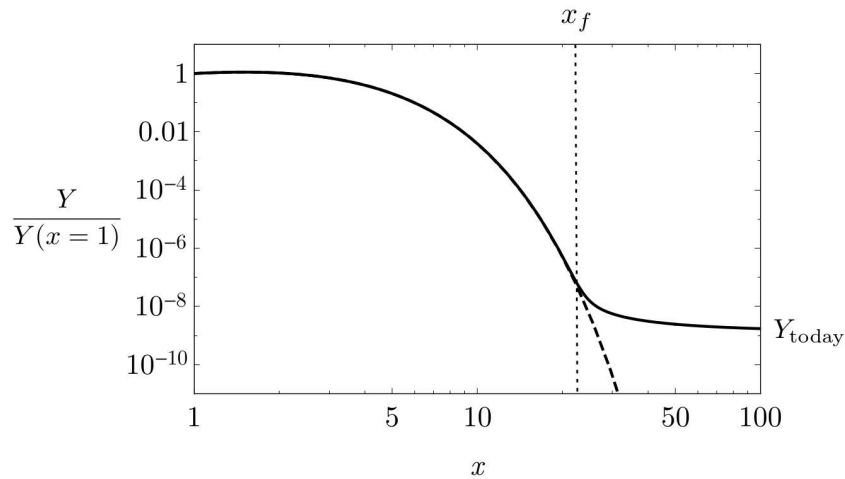


Figure 1.9: Evolution of Cold Dark Matter number density with time variable  $x$ ,  $x_f$  is the time of *freeze-out*, from [34].

where  $\rho_{cr}$  is the critical density in the universe required for it to be at balance. This is called the "WIMP miracle" for the theoretical Weak Interacting Massive Particles (WIMPs) which have some candidates within the Super Symmetry (SUSY) theory. Although the annihilation of these particles would be strongly suppressed after freeze-out, it can still occur in regions with high DM density. The products of this annihilation are pairs of SM particles that can be detected as an excess signal in particle detectors, giving an indirect evidence of the presence of DM.

This way,  $\gamma$ -ray astrophysics can contribute to the indirect detection of DM signatures: Two DM particles can annihilate directly into a pair of  $\gamma$ -rays with a characteristic line spectrum with  $E_\gamma = m_\chi$  or they can annihilate into pairs of other SM particles which afterwards decay giving out a continuum spectrum of  $\gamma$ -rays.

The differential flux of photons produced by DM annihilation is described as:

$$\frac{d\Phi}{dE} = \frac{1}{8\pi} \frac{\langle \sigma v \rangle}{m_\chi^2} \frac{dN_\gamma}{dE} \int_{\Delta\Omega} \int_{l.o.s} dl \rho^2(\vec{l}) \quad (1.23)$$

Where  $dN/dE$  is the spectrum of  $\gamma$ -rays from annihilation of a pair of dark matter particles,  $\langle \sigma v \rangle$  is the thermal velocity averaged annihilation cross section,  $m_\chi$  is the DM particle mass and  $\rho$  is the dark matter density profile. If DM particle is not its own antiparticle, equation 1.23 should be multiplied by a factor 1/2.

The first term of the equation comes from the already discussed particle physics, depends on the annihilation channel and the mass of the particle. The integral second term is known as the J-factor and is the integral over the line of sight and solid angle  $\Delta\Omega$  of the squared DM density profile ( $\rho$ ) and it dependent on the source. The most simple density profile for a dark matter halo that we can think of is a self-gravitating

isothermal gas sphere, where:

$$\rho(r) \propto 1/r^2 \quad (1.24)$$

However, to address the actual physics of galaxies evolution, we need to rely on structure formation simulations which follow the initial DM density perturbations until the formation of current halos. From these simulations and from actual observations [35] we know that the DM density profile can be well reproduced as a six-parameters function of distance  $r$  from the center of the profile [36][37][35]:

$$\rho(r) = \frac{\rho_0}{\left(\frac{r}{r_s}\right)^\gamma \left[1 + \left(\frac{r}{r_s}\right)^\alpha\right]^{\frac{\beta-\gamma}{\alpha}}} \Theta(r_{max} - r) \quad (1.25)$$

Where  $\Theta$  is the Heaviside step function,  $r_s$  is the scale radius and  $\rho_0$  is the characteristic density. These two last parameters depend on the specific DM halo. Setting  $(\alpha, \beta, \gamma) = (1, 3, 1)$  we retrieve the Navarro-Frenk-White profile [38]. Combinations of these parameters can be used to fit a possible DM signal to a specific profile. Other types of profiles have also been treated in the literature, such as the Einasto profile [39].

From 1.23, we can see that the best objects to search for a  $\gamma$ -ray signal will be those that are nearby and DM dense, so the J-factor would be sufficiently large relative to the background of  $\gamma$ -rays produced by ordinary matter interactions.

## 1.6 $\gamma$ -ray sources

In the previous section, the processes that produce  $\gamma$ -ray emission were introduced. In this section, the astrophysical objects where they take place are described. Two major classes of  $\gamma$ -ray emitters can be distinguished: galactic sources and extragalactic sources. At the end of the section, potential sources for DM annihilation signals will be also covered. Figure 1.10 show the current known population of VHE  $\gamma$ -ray sources based on the observations of the current generation of  $\gamma$ -ray detectors, either in space (*Fermi-LAT*) or ground based (the Major Atmospheric Gamma Imaging Cherenkov Telescopes (MAGIC), the High Energy Stereoscopic System (H.E.S.S.), the Very Energetic Radiation Imaging Telescope Array System (VERITAS) and the High-Altitude Water Cherenkov Observatory (HAWC)).

### 1.6.1 Galactic sources

As shown in figure 1.10, the richest region in  $\gamma$ -ray sources is the galactic plane, meaning that the majority of detected emitters belong to our galaxy. In this section, the different characteristics of these sources will be described.

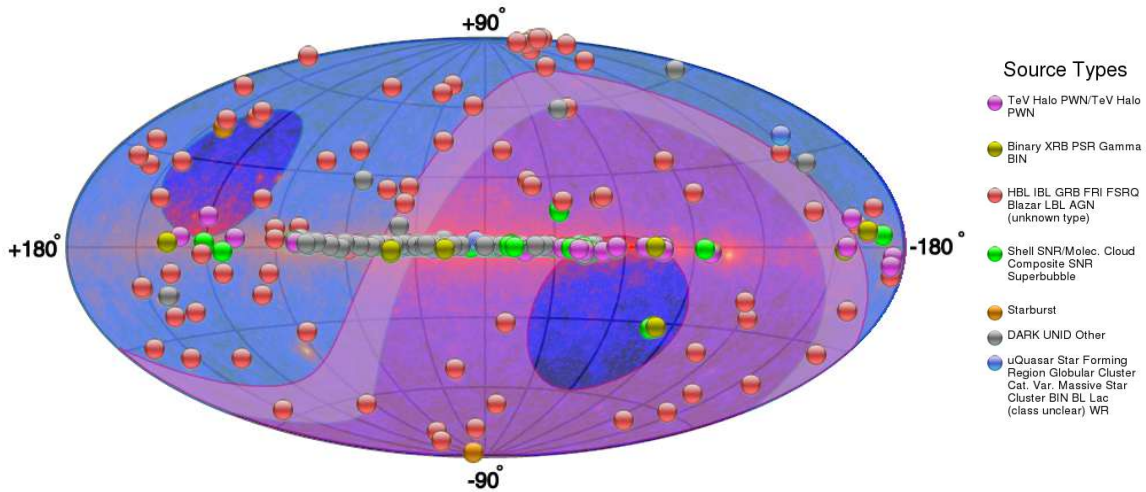


Figure 1.10: Full skymap from TeVCat[40] catalog as of July 2019, with all the detected TeV sources. In the background, the *Fermi*-LAT skymap is shown and the shadowed regions correspond to the MAGIC field of view (blue) and H.E.S.S. (pink).

### Pulsars

Pulsars are the most common type of  $\gamma$ -ray emitters known. When a massive star ( $< 8M_{\odot}$ ) suffers gravitational core collapse at the end of its life, the resulting object is a compact neutron star sustained by degeneracy pressure, where neutronization (the combination of protons and electrons) has taken place due to the extremely high pressures which lead to high densities ( $> 10^9 g/cm^3$ ). The neutron star comprises  $1 - 2 M_{\odot}$  in a radius of  $10 - 14$  km and as the angular momentum of the parent rotating star is conserved, the much more compact neutron star will spin at extremely high velocities with periods that can go from milliseconds to a few seconds. This fast spin produces strong magnetic fields in their surroundings where electrons and positrons are accelerated by the electric field aligned with the magnetic field. When the magnetic fields are aligned with the line of sight from the Earth, we can detect a pulsed emission (mainly synchrotron and curvature radiation) with the period of the rotation of the neutron star, and the object is called a pulsar. Pulsed emission from this kind of object has been detected a broad band in the electromagnetic spectrum, from radio to  $\gamma$ -rays.

It is generally accepted that the origin of the  $\gamma$ -ray emission from pulsars is due to curvature radiation, produced when relativistic electrons accelerated in gaps of the electromagnetic fields powered by the pulsar rotation, are trapped and propagate along the lines of the magnetic field [41]. However, the location of the gaps and the dominating acceleration mechanism are not well known and there are different models proposed (see figure 1.11).

Combined observations of the Crab pulsar from the Imaging Compton Telescope (COMPTEL), the Energetic Gamma Ray Experiment Telescope (EGRET)

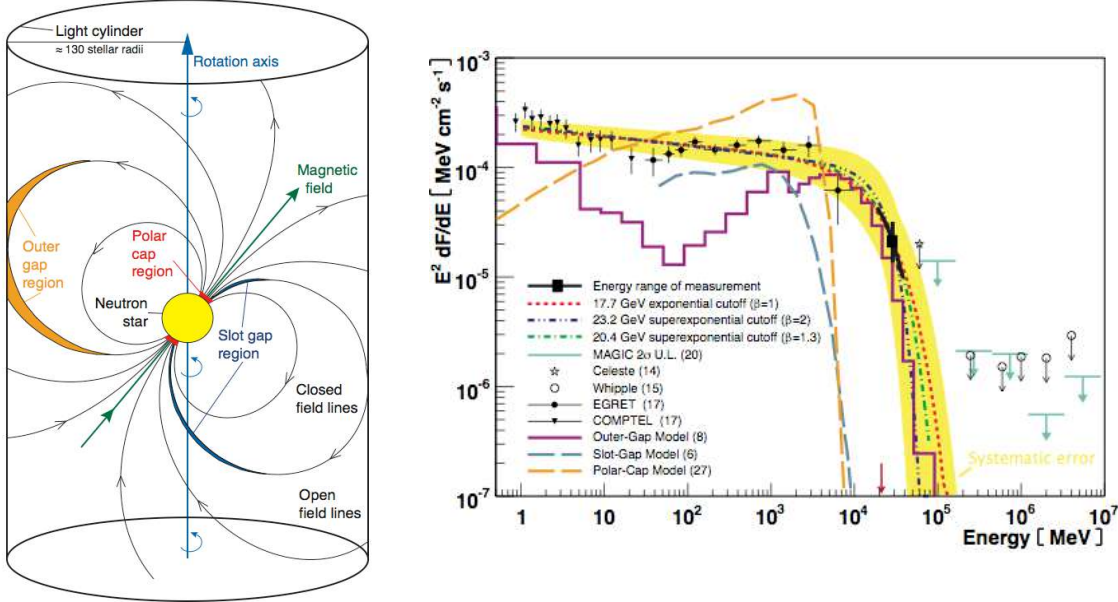


Figure 1.11: *Left:* Crab pulsar's magnetosphere where the location of the three models (Polar-Cap in red, Slot-Gap in blue and Outer-Gap in yellow) is shown. *Right:* Crab pulsar spectral cutoff. Figures from [41]

[42], MAGIC [41], VERITAS [43] and *Fermi*-LAT [44] have shown that their spectrum follows a power law with a cutoff at energies over a few GeV (see figure 1.11). The detection of the pulsar emission at energies over 25 GeV by MAGIC ruled out the possibility of acceleration happening too close to the pulsar (as the Polar-Cap model assets) because the magnetic pair-production attenuation would provide a super-exponential cutoff at much lower energies to those observed. Currently, the Outer-Gap model offers the best explanation of the observed Crab spectrum [45]. While pulsars are the most common  $\gamma$ -ray emitters, only two have been detected in the VHE range, up to TeV energies: the Crab and Vela pulsars [46].

### Supernova Remnants

Supernovae are the result of the evolution of a star, which suddenly becomes much brighter while shells of gas are expelled to the interstellar medium in an explosive event. They can be classified in different types by features in their spectrum which also imply a different origin of the explosion. Type II supernovae show hydrogen emission lines, meaning they come from very massive stars ( $M > 8M_\odot$ ) with hydrogen in their outer layers. After burning lighter elements (H, He, etc.) into heavy nuclei, fusion reactions become inefficient and the imbalance between gravitational forces and pressure radiation lead to the collapse of the central core into a neutron star or a black hole in a violent reaction, expelling shells of material at high velocities. Type I supernovae do not present hydrogen lines, meaning they come from a hydrogen-poor star. They usually are produced by white dwarfs in binary systems which accrete material until

reaching the Chandrasekhar limit [47] and suffer a thermonuclear explosion. Type I supernovae are classified in subtypes: Type Ia show Si lines in their spectra, whereas those without these lines are classified as Ib if they have He lines and Ic if not [48]. The structure of ejected material which is left in the surroundings of the parent star is the SNR. These structures can be classified in different types depending on their spectrum, but the most important feature to differentiate them is the presence (or not) of a shell. There are shell-type SNR, in which the material in the surroundings is heated by the power of the shockwave during the SN explosion. The so called *plerion* SNR or Pulsar Wind Nebula (PWN) do not present a shell. The result of the SN explosion is always a central pulsar and their emission is produced by the interaction between electrons ejected to the medium by the pulsar and its huge magnetic field. There is also a composite type of SNR where a plerion is surrounded by a shell and depending on the wavelength observed, they emit more like one type or the other [49]. Depending on the SNR type, the particle acceleration and  $\gamma$ -ray emission would have a different origin and features.

- **Shell-type remnants:** Shell-type remnants, the commonly referred simply as SNRs, are the most popular candidates for CR acceleration. CRs are deflected by magnetic fields in the ISM which makes it impossible to trace back the emission direction, but neutral particles, like neutrinos and  $\gamma$ -rays coming from SNRs can be used as tracers of CR acceleration. We know CRs can produce  $\gamma$ -rays via hadronic interactions with the gas and dust in the medium. For example, the production of pions and posterior pion decay would give rise to a spectrum with a characteristic peak at 67.5 MeV, if pions are at rest.

A simple energetic argument is used to pose shell type remnants as the main source of galactic CRs: As a rough estimation, if we assume that the typical total kinetic energy produced by a SN explosion is around  $E_{SN} \sim 10^{51}$  erg, with a SN rate in the galaxy of about one in 50-100 years, and a constant fraction  $\eta$  of the kinetic energy is transferred to hadrons, it can be shown that this fraction has to be of the order of the 10% to retrieve the approximated CR luminosity in the galaxy  $L_{CR} \sim 2 \times 10^{41}$  erg/s.

$$L_{CR} = \eta \cdot E_{SN} \cdot SN_{rate} = 0.1 \cdot 10^{51} \text{erg} \cdot 50 \text{yr}^{-1} \propto 10^{41} \text{erg/s} \quad (1.26)$$

A more detailed analysis using real data of galactic SNR was done by [50] arriving at the conclusion that future  $\gamma$ -ray data can be used to constrain the amount of CR energy coming from SNR. However, there are still problems on proving this hypothesis because many of the  $\gamma$ -ray signatures coming from SNR have a leptonic origin rather than hadronic. Also, for SNR to reproduce the full spectrum of CR, SNRs should be pevatrons (meaning they can accelerate CR to PeV energies) at some fraction of their lifetimes, to reach the region after the *knee*. Still, no SNR pevatron has been observed yet but high hopes are deposited in the next generation of  $\gamma$ -ray experiments [51].

- **Plerions or Pulsar Wind Nebulae.** As mentioned, PWN are powered by a central rotating pulsar which dissipates kinetic energy over time in the form of *spin down luminosity*. This energy is injected steadily into the surrounding nebula of ejected material that was formed during stellar evolution. To understand the features of the emission of Pulsar Wind Nebulae (PWNe), it is important to follow their evolution with time and how the period, spin down luminosity and magnetic field changes [52]. A pulsar is formed in a SN explosion and the final state of the pulsar and its PWN will depend on how it interacts with the SNR. If the SNR expands outward freely, the pulsar will remain in the center, but if a reverse shock happens, reverberations between the PWN and the shock can produce instabilities which in the end will displace the pulsar from its original position, even being able to cross away the SNR shell.

Strong magnetic fields in pulsars create currents of particles of the surrounding nebula, producing pulsar winds. Electrons accelerated this way produce synchrotron radiation from radio to X-ray wavelengths. The wind starts decelerating when reaching the nebula radius, due to the more slowly expanding material and thus a wind termination shock is formed. The TeV  $\gamma$ -ray emission from PWNe is explained as IC emission produced by the relativistic particles in the shocked wind interacting with the synchrotron photons. The Crab PWNe was the first source detected of this type, associated with a SN explosion observed in 1054 CE, and has become a sort of standard candle for  $\gamma$ -ray astrophysics.

- **Composite remnants.** A rare type of SNR is a combination of the previous two, where a PWN is surrounded by a shell-type SNR. Usually, PWN are considered young SNRs while shell-types are older systems. Composite SNRs could be an intermediate phase of evolution where the shell and the PWN evolve and interact together [53]. In these systems, the PWN formed in the interior of the SNR expands outwards and it can encounter the inward reverse shock of the SNR [54]. Some examples of this kind are SNRs W28, W44 and SNR G21.5-0.9, which is shown in figure 1.12.

### $\gamma$ -ray binaries

$\gamma$ -ray binaries are systems composed by two objects orbiting each other: One is a compact object, such as a pulsar and the other can be an ordinary massive star big enough to reach the Roche lobe of the pulsar and so stellar winds connect the two objects. Just a few objects (< 10) of this kind have been detected in HE and VHE  $\gamma$ -rays very recently [55], and yet the exact mechanisms of the origin of their emission are unknown. There are two main explanations to the HE and VHE emission in  $\gamma$ -ray binaries. It can be produced by accretion energy released in the form of relativistic jets, or on the other hand, by the energy emitted by the pulsar in the form of pulsar winds in a similar way as in PWNe. The first case is denominated the *microquasar* scenario due to its similarities with AGN (also known as quasars) but emitting jets in

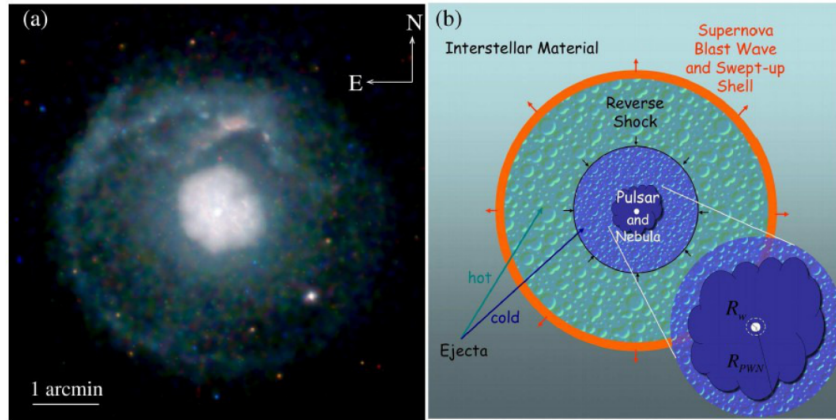


Figure 1.12: a): Chandra X-ray image of the composite SNR G21.5-0.9. b): Diagram of a PWN inside a SNR. Pictures from [54].

a smaller scale. However, a variety of indirect evidences seem to favour the pulsar wind interpretation mainly based in the spectral similarities of the known binaries with the power of a pulsar spindown. Also the presence of strong magnetic fields and morphological characteristics of radio emission are similar features to those found in PWNe [56].

### **Novae**

Binary star systems are rather common objects in the universe. One of the stars can be more massive than the other, evolving faster and becoming a white dwarf while the second star can still be in its main sequence phase. If this happens, the white dwarf can start accreting material from the companion, building an accretion disk. The hydrogen rich gas in the surface of the white dwarf starts heating the bottom layers which becomes electron-degenerated, leading to a chain of thermonuclear explosions [57]. This event is known as "classical nova". When the companion star is a red giant, which has highly increased its volume, the system is called a *symbiotic binary system*. In this case, the interaction between the stellar wind of the red giant and the white dwarf surface expansion give place to a favorable scenario for particle acceleration. Both classical novae and symbiotic systems have been detected in HE  $\gamma$ -rays by *Fermi*-LAT [58], [59] although these results do not allow to differentiate between the different emission scenarios.

### **The Galactic Center and the Fermi Bubbles**

The center of the Milky Way, known as the Galactic Center (GC), is a region of the sky situated at  $4^\circ$  longitude,  $2^\circ$  latitude, with a size of  $600 \times 300$  pc and at a distance of about 8 kpc. It is obscured by dust in the optical and ultraviolet range, but emission in infrared, radio, X-rays and  $\gamma$ -rays reveals a prolific region full of energetic sources.

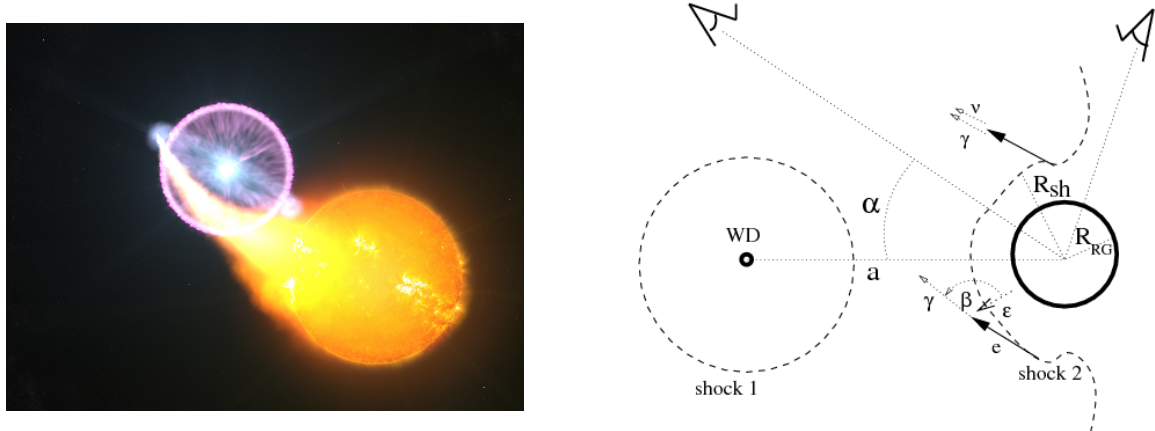


Figure 1.13: *Left:* Artist concept of a classical nova. Credits: NASA’s Goddard Space Flight Center/S. Wiessinger. *Right:* Diagram of the geometry of the symbiotic binary system V407 Cyg from [60]. The expanding shock (1) from the white dwarf partially overtakes the Red Giant (shock 2), producing particle acceleration through IC (leptonic scenario, with angle of interaction  $\beta$ ) and proton collisions with the red giant wind (hadronic scenario).

Among many SNRs, PWNe and stellar clusters in HII regions, there is also a Super Massive Black Hole (SMBH), Sagittarius A\*, whose detection has been one of the major motivations for GC surveys. Many  $\gamma$ -ray experiments have surveyed the GC region (*Fermi*-LAT , MAGIC [61], H.E.S.S. [62], VERITAS [63]) and emission from HE to VHE bands has been detected. The main problem with this highly populated region is the difficulty of tell apart individual sources, making it a big challenge to identify the actual emission from Sgr A\* [64]. The high energy emission from Sgr A\* has its origin in the strong winds produced by the presence of an accretion disk surrounding the black hole, where material is accelerated at very high energies [65].

Closely related to Sgr A\* might be the *Fermi bubbles*, two large  $\gamma$ -ray lobes that appear to be ejected from the center of the galaxy. They were discovered while searching for a  $\gamma$ -ray counterpart to the WMAP haze [66], which is a residual microwave emission that arises after subtracting all the other known emission components. They extend to  $55^\circ$  up and above the GC and are not symmetric, with an enhanced emission towards the south-east side of the bubbles. With well defined edges, an uniform power-law spectrum of index  $\sim 2$  and a cocoon-like shape, they resemble jet-like structures [67]. Their origin is still under debate: They could be jets, outflows or the result of accretion events from the black hole, winds from SN explosions or the remnant of AGN activity in the Milky Way in the past.

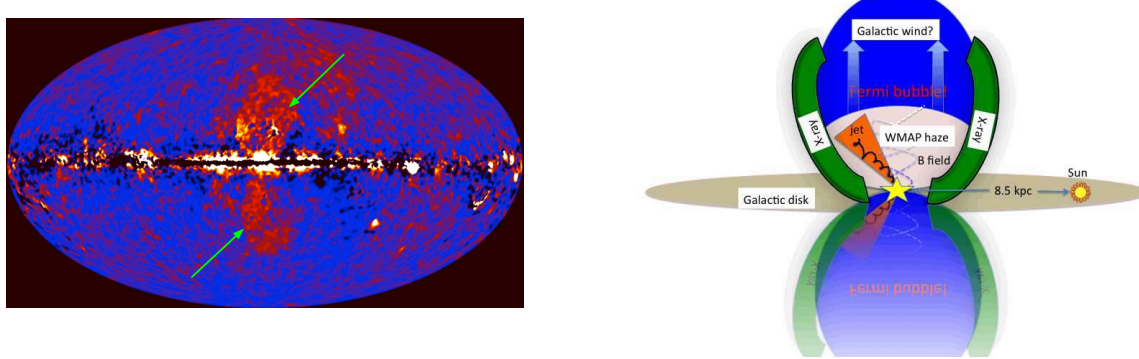


Figure 1.14: *Left:* The Fermi Bubbles as seen by *Fermi*-LAT after subtracting all the other known  $\gamma$ -ray components. Credits: NASA/DOE/Fermi LAR/D. Finkbeiner et al. *Right:* Schematic picture of Fermi Bubbles structure from [66].

### Globular Clusters

Globular clusters are compact gravitationally bounded stellar associations with spherical geometry which are distributed outside the galactic plane, conforming a spherical halo around the galaxy. They are old highly evolved systems with many compact objects like neutron stars, white dwarfs and pulsars even forming binary systems. Furthermore, the majority ( $\sim 80\%$ ) of Millisecond Pulsars (MSPs) (pulsars with a period of the order of milliseconds) detected up to date have been found in globular clusters.

Since all the mentioned objects are well known  $\gamma$ -ray emitters, globular clusters have been observed and detected in  $\gamma$ -rays by *Fermi*-LAT [68] and H.E.S.S. [69]. Even pulsed  $\gamma$ -ray emission have been observed from individual MSPs [70], [71]. Two types of models of  $\gamma$ -ray emission have been discussed to happen in globular clusters, both related to MSPs. One takes place in MSPs magnetospheres, where  $\gamma$ -ray emission would be produced by curvature radiation. The second type of models involve IC scattering of electrons accelerated close to the MSP with optical, infrared or CMB photons [72].

### 1.6.2 Extragalactic sources

While most of the  $\gamma$ -ray emission detected on Earth comes from the galactic plane, there is a big amount of individual sources outside our galaxy which produce HE radiation and allow the study of a new range of extragalactic phenomena. A big caveat for extragalactic sources is that the VHE range is suppressed by the EBL absorption, as described in section 1.4.

### Active Galactic Nuclei

AGN are the brightest steady sources of  $\gamma$ -ray in the universe and the most luminous known electromagnetic emitters. Known as *black-hole galaxies*, their strong emission is powered by infalling gas into a massive Black Hole (BH) located in the center. The

BH attracts gas and material from the galaxy forming an accretion disk, where matter loses angular momentum through viscous and turbulent processes, and emits a huge amount of energy from ultraviolet to soft X-ray bands [73]. AGN can be classified in two broad types, according to their radio emission: *Radio-quiet* and *radio-loud*. Further observational classification depends strongly on the orientation angle, which can make AGNs appear as spectroscopically completely different sources, depending on the region of the object that is showing. All AGN have a dusty tori, broad-line regions, narrow-line regions and strong blue/UV bump emissions from the accretion disk [74]. Depending on the angle, one or several of these regions will be observable and will show their particular features in the spectrum. Figure 1.15 show a scheme of AGNs taxonomy.

Radio-loud AGN, also known as *blazars*, are about three orders of magnitude brighter in radio band than their quiet counterparts. This radio emission is directly related with the presence of relativistic jets of plasma which carries a big part of the energy released during accretion and that afterwards is emitted as radiation from radio to  $\gamma$ -rays [75]. They are associated with elliptical galaxies that have undergone recent mergers. On the contrary, radio-quiet galaxies do not show jets and so do not account for high energy non-thermal emission. Also, they are typically spiral galaxies in lower density regions [76]. Blazars are rare among AGN, accounting only for 10% of the total, but a large number of them has been detected in  $\gamma$ -rays, with more than 1500 sources detected at GeV energies, and more than 60 at TeV energies [74].

### Gamma Ray Bursts

GRBs are short and intense flashes of  $\gamma$ -ray emission coming isotropically from random directions in the sky. With a range of luminosities from  $10^{51}$  ergs/cm<sup>2</sup> to  $10^{52}$  ergs/cm<sup>2</sup> they are the brightest transient objects in the sky [78]. They can be classified by their duration, having two distinct populations: short GRBs, which last just a few seconds; and long GRBs which can last for few minutes [79]. Long bursts are usually followed by afterglows in X-rays, optical and radio which can last for several years after the event. The so called *fireball* model is the generally accepted mechanism which drives GRB [80]. Since the observed emission of the bursts is not thermal, its origin must be the result of the conversion of an ultra-relativistic energy flow into radiation in an optically thin region. The energy flow could come from the kinetic energy of accelerated particles or electromagnetic Poynting flux. In this model, the process is ignited by an "inner engine" which is not possible to observe directly, but which activity can be characterized by the observed temporal structure of the bursts. The engine produces an explosive fireball of the size of the engine itself. There is an alternative model based in internal shocks, where the engine would produce a wind and a long energy flow. About the nature of the phenomena producing GRBs, there exist an apparent difference between the origin of short GRB and long GRB according on their hardness ratio (defined as the ratio of the flux in two separated bands) versus duration plot (see figure 1.16) [79].

These two populations in the hardness ratio vs. duration plot, together with rather

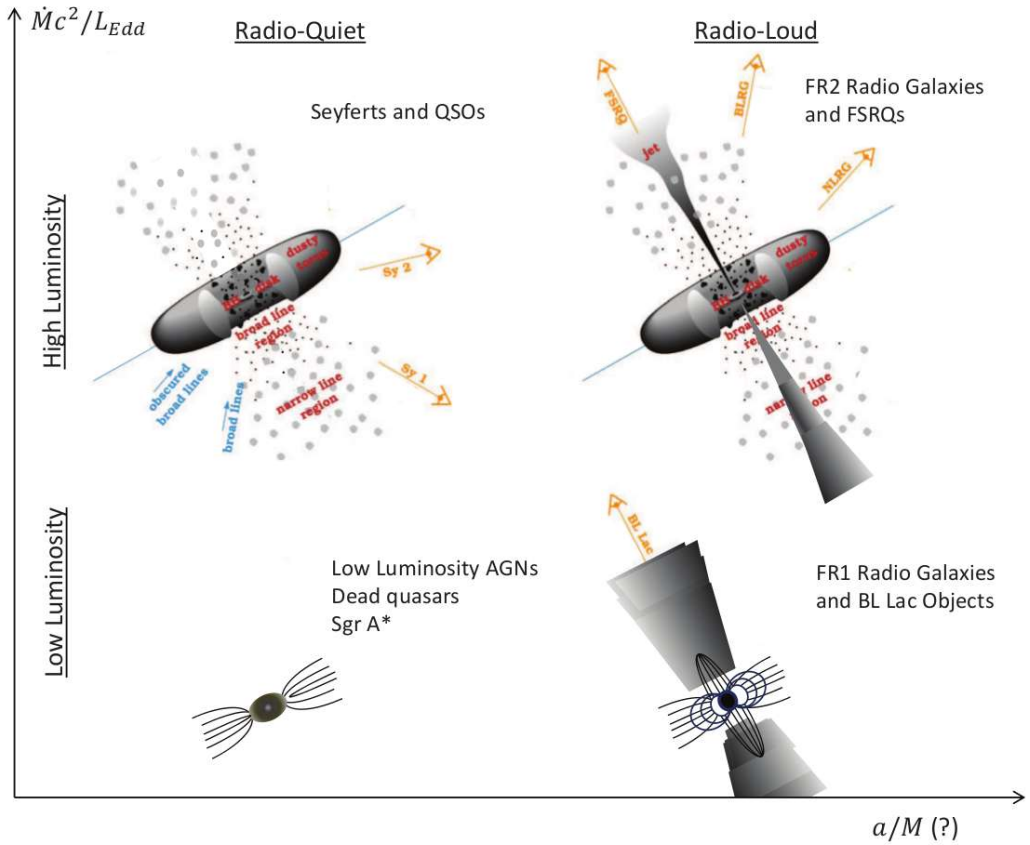


Figure 1.15: Top: AGN taxonomy as from [74]. In this scheme, the vertical axis represents the luminosity power in terms of the mass-accretion rate and horizontal axis represents the BH rotation. Bottom: Observational classification of active galaxies. QSO= quasi-stellar objects; Sy1(Sy2) = Seyfert 1(2); FR1(FR2)=Fanaroff-Riley 1(2). Pictures based on [77] from [74].

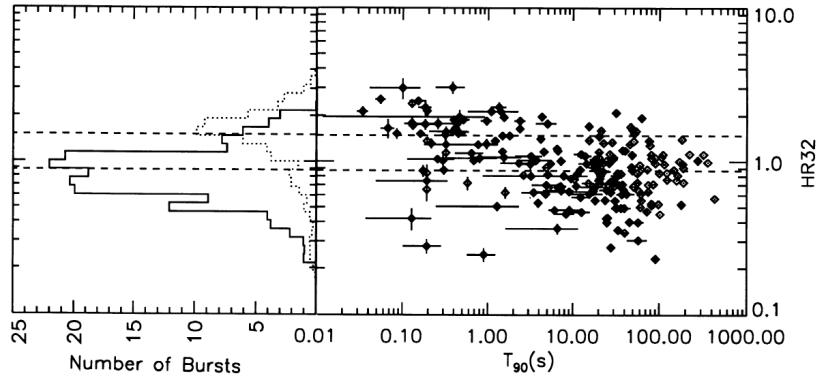


Figure 1.16: *Left:* Hardness ratios for the two duration classes of GRB. Solid lines corresponds to short GRBs, dashed line to long GRBs. *Right:* Hardness vs. duration plot, where duration  $T_{90}$  is defined as the time during which the cumulative counts > 25 keV increase from 5% to 95% above background. Dashed lines correspond to the mean hardness ratio of the two classes. Figure from [79].

significant spectral differences [81] and afterglow observations, suggest that long GRBs are closely related to star forming regions, compatible with SN explosions of massive stars. Short GRBs on the other hand, could be related to more evolved regions and be the result of neutron star mergers, such as the recently detected gravitational wave event GW170817 by LIGO/VIRGO [82] which was also detected as a GRB by the Fermi Gamma-Ray Burst Monitor and later observed by *Fermi*-LAT [83]. Also recently MAGIC, which were specifically designed to observe such objects, detected the first event in the VHE range [84].

### Starburst galaxies

Starburst galaxies are those with a greatly enhanced star formation, whose Star Formation Rate (SFR) is considered to be out of equilibrium, consuming gas for star formation at very short timescales ( $< 1$  Gyr). Since the SFR is highly correlated with the SN explosion rate, it is expected that  $\gamma$ -ray emission detected from starburst galaxies has its origin in SNRs.

The production and transport of CRs in the ISM significantly affects the star formation, because CRs penetrate deep into molecular cloud cores (molecular clouds are dense gas regions where star formation takes place) catalyzing complex chemical reactions which can affect the initial conditions of star formation and evolution [85]. The conditions of the ISM in starburst galaxies are very different from Milky Way [86]. The gas density is much higher and the high population of massive stars produce a huge amount of radiation, which is absorbed by dust and re-emitted in infrared. Magnetic fields are also affected by the presence of such population. Thereby particles accelerated in the region will suffer strong losses of energy and faster cooling. Detection of  $\gamma$ -rays from starburst galaxies is a key probe to understand the efficiency of CR acceleration in SNRs and CR transport in different ISMs.

The current generation of  $\gamma$ -ray telescopes have detected NGC253 and M82 starburst galaxies ([86], [87], [88]), which has been long predicted to emit  $\gamma$ -rays up to VHE range.

### **Galaxy clusters**

Galaxy clusters are the largest gravitationally bounded structures in the universe. They are mainly composed of DM (70-80% of the total mass) and their ordinary matter is composed by the galaxies and the filaments connecting them, plus a big amount of hot gas in the surroundings called the Intracluster Medium (ICM)[89]. In the standard paradigm of structure formation, clusters are formed by hierarchical mergers and accretion of smaller structures. Mergers are the most energetic phenomena to occur in the universe (they release  $10^{63}$ - $10^{64}$  ergs/Gyr) and they dissipate energy in the form of shocks which heat the gas, or through large-scale ICM motions [90]. Part of the energy dissipated during this process is fused into particle acceleration to ultra-relativistic energies, thus they are a source of CR production. Radio observations of galaxy clusters proves the existence of non thermal emission from synchrotron radiation processes in the ICM. Galaxy clusters can therefore be a source of HE photons which can be produced via leptonic scenario through IC scattering of CMB photons with ultra-relativistic electrons, or hadronic scenario by neutral pion decay.

Until recently,  $\gamma$ -ray experiments that tried to detect  $\gamma$ -ray signal from the closest galaxy clusters were only able to set upper limits [91], [92]. *Fermi*-LAT was able to report a detection of an extended  $\gamma$ -ray signal from the Coma cluster roughly correlated with the radio halo [93].

### **Neighbour galaxies**

The Local Group is the cluster of galaxies gravitationally bounded to the Milky Way. They are the closest galaxies to be observed and their characteristics are expected to be similar to those of our own galaxy. The second and third closest and spatially resolved galaxies (the first being the Canis Major dwarf galaxy) are the Large Magellanic Cloud (LMC) and the Small Magellanic Cloud (SMC). They are two irregular dwarf galaxies seen in the southern hemisphere, at a distance of 50 kpc [94]. They present a remarkable high star formation rate ( $\sim 0.2\text{yr}^{-1}$  for the LMC,  $0.3\text{yr}^{-1}$  for the SMC [95], compared to the  $0.68\text{yr}^{-1}$  to  $1.45\text{yr}^{-1}$  of the Milky Way [96] in a much smaller volume.). They can produce  $\gamma$ -ray emission due to the interaction of CR with ISM. The first detection of a  $\gamma$ -ray diffuse signal from the LMC was made by EGRET [97], being the first normal galaxy outside the Milky Way detected in  $\gamma$ -rays. The SMC was first detected in  $\gamma$ -rays by *Fermi*-LAT [98]. Further observations of the LMC from *Fermi*-LAT at HE [99], [100], [101] and H.E.S.S. [102], [103] at VHE revealed a complex structure of the diffuse emission and a population of very interesting individual sources comprising pulsars, SNRs, PWNe and  $\gamma$ -ray binaries. Since the LMC emission in  $\gamma$ -rays is one of the main topics of this thesis, it will be extensively

treated in chapter ??.

Apart from the before mentioned starburst galaxies M82 and NGC253, other close galaxies such as M31 and M33 have also been observed and detected in HE  $\gamma$ -rays by *Fermi*-LAT [104].

### 1.6.3 Potential Dark Matter annihilation emission sources

In section 1.5 the production of  $\gamma$ -rays through WIMP annihilation or decay was described. In the search for this kind of signal, one can analyze which would be the best sources in the universe for an indirect search of DM. First of all, they must have a high amount of DM, given by the astrophysical parameter J-factor (integral term in eq. 1.23). Also, a low background of other  $\gamma$ -ray sources would allow to unequivocally identify the DM signal. Following these premises, indirect DM searches have been performed by  $\gamma$ -ray experiments in the most promising sources, described in this section.

#### Milky Way Galactic Center

In the present evolutionary stage of the universe, galaxies are believed to be embedded in DM halos which extend much more than the visible matter, the center of the galaxies being the location of higher DM density [105]. The center of the Milky Way is therefore a promising target for DM searches. However, as explained in section 1.6.1, it is also a very populated region with many  $\gamma$ -ray sources which are even not fully resolved. This fact makes the GC a true challenge for disentangle a possible DM emission, needing a very good background modelling and control of the instrumental systematics [106]. Usually, DM searches in the GC tend to avoid the galactic plane region, observing a region with lower background at expenses of having a weaker DM signal due to the lower density.

The most constraining upper limits in the VHE energy range for the velocity averaged cross section  $< \sigma v >$  in the GC have been established by H.E.S.S. [107]. Both *Fermi*-LAT and H.E.S.S. have accounted for a  $\gamma$ -ray excess coming from the GC of unknown origin which has been tried to be fitted with the most conventional DM models, but the results were not sufficiently compatible [108], [109].

#### Dwarf Spheroidal Galaxies and Dark Clumps

Following the standard model of cosmology, N-body simulations of the evolution of CDM since the Big Bang predicts a hierarchical structure formation where DM clusters into subhalos which merge into higher structures. The final picture at galactic scales, are galaxies embedded in a big DM halo, surrounded by a population of subhalos with mass inversely proportional to their number [110]. Simulations like Via Lactea II predict that the Milky Way is surrounded by a large number of DM subhalos ( $\sim 50,000$ ). The heavier of these substructures are the so called Dwarf Spheroidal Galaxies (DSphe). They are very faint galaxies (in optical) orbiting the Milky Way.

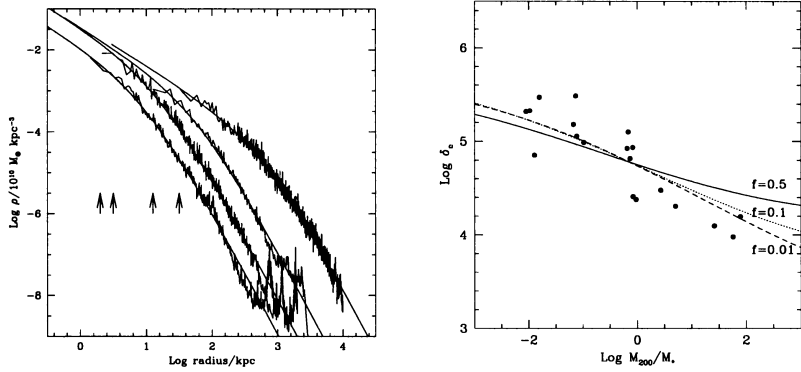


Figure 1.17: *Left:* Typical density profiles from Cold Dark Matter (CDM) halos obtained from N-body simulations. *Right:* Characteristic overdensity of halos as a function of mass. Masses are expressed in units of the current non linear mass corresponding to the standard biased CDM spectrum  $M_* = 3.3M_\odot$ . Figures from [105].

Many of the observed DSphe are strongly DM dominated, but have absent or very little star formation and no signal of ionized or neutral gas [111]. Smaller structures with no emission at all are known as Dark Clumps.

These kind of objects are a perfect target for DM searches because no  $\gamma$ -ray signal is expected from them due to ordinary astrophysical processes. Any  $\gamma$ -ray detection would be an unequivocal signal of DM annihilation.

The present generation of  $\gamma$ -ray experiments have widely studied these objects in the search for DM, not yet being successful at detection but setting very stringent upper limits on DM models using data from many DSphe ([112], [113], [114], [115], [116]).

### Galaxy Clusters

As has been mentioned before in section 1.6.2, galaxy clusters are mostly dominated by DM with a very high mass-to-light ratio. For this reason, they are good targets for indirect DM searches both for annihilation and decay. They are specially suitable for decaying DM, since at large volumes the signal of decaying DM which is proportional to the first power of the density overshines the signal of annihilation [117].

Strong constraints for a wide number of models for DM annihilation and decay have been set by *Fermi*-LAT [118], [119] and H.E.S.S. [120], and also constraints on the decaying lifetime of DM were set by MAGIC [121].

### The Large Magellanic Cloud

The LMC has been considered a well promising target for DM searches due to its proximity and rather high J-factor ( $10^{20}J/\text{GeV}^2\text{cm}^{-5}$ ). Kinematic studies of the LMC show that more than half of the LMC mass is forming a dark halo with a compact central bulge [122], [123].

*Fermi*-LAT has used five years of data to set constraints on the DM annihilation

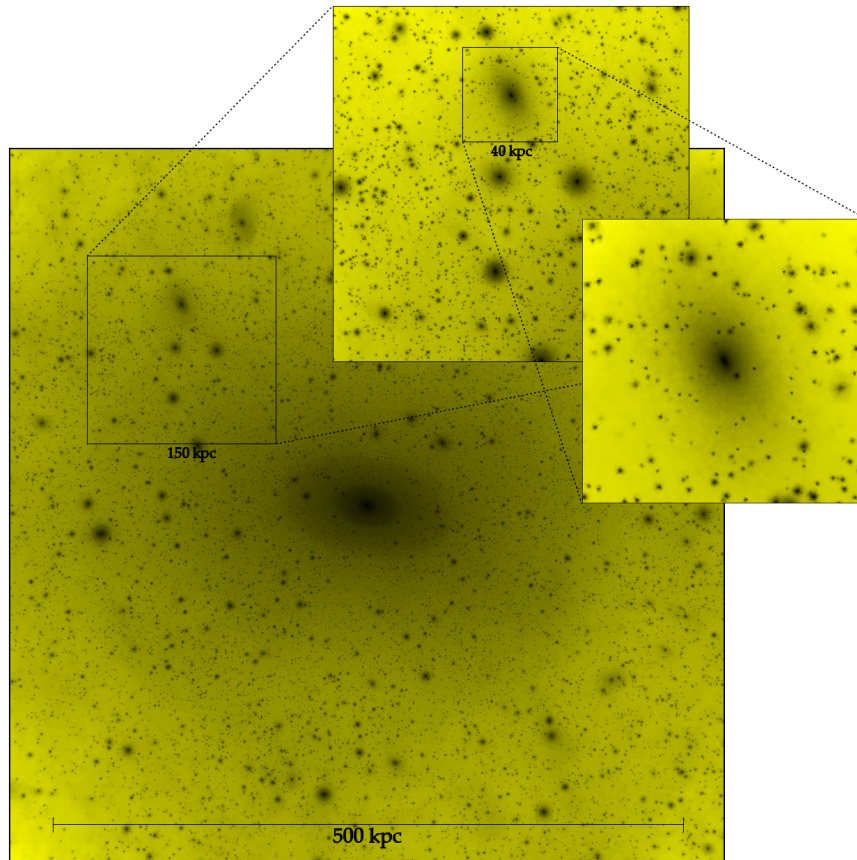


Figure 1.18: Results from *Via Lactea* N-body simulations of DM substructures. The picture show a projection of density squared in a  $566 \text{ kpc} \times 566 \text{ kpc} \times 566 \text{ kpc}$  region centered on the host halo at  $z = 0$ , from [110].

signal from the LMC in the HE regime [124]. No limits has yet been set in the VHE range though. As one of the main topics of this thesis, more on this subject will be extensively discussed in chapter ??.



Discoveries in astronomy have always been directly related to technological advances of new instruments and observation techniques. The first astronomical telescope was developed by Galileo in the *XVII* century and it allowed him to observe for the first time the four brightest moons of Jupiter. Since then, and specially during the *XX* century, a broad new range of experiments, detectors and telescopes have been built either on the ground or in space. Thanks to them, astronomers have observed the universe in every wavelength from radio to  $\gamma$ -rays. Furthermore, the recent field of multimessenger astronomy has started a new era, combining electromagnetic radiation with other cosmic messengers such as neutrinos and gravitational waves.

This chapter is dedicated to the technologies used to detect  $\gamma$ -rays, from the history of first detectors, to the present generation and future of  $\gamma$ -ray observatories.

Contrary to the visible light that Galileo received with his first telescope,  $\gamma$ -rays cannot be directly observed from Earth. The atmosphere absorbs most of the radiation coming from space, limiting the range of the spectrum that can be detected with ground based detectors. As shown in figure 2.1, only visible and radio wavelengths reach the ground through the so called *atmospheric windows*, hence  $\gamma$ -rays can be observed only from outside the atmosphere, with detectors in balloons or satellites. A description of different types of such detectors and their used techniques is given in section 2.1.

Other possibility is to take advantage of the interactions of  $\gamma$ -rays with particles in the atmosphere when they are absorbed. When a  $\gamma$ -ray or any cosmic particle hits an atmospheric atom, a large number of secondary particles is produced which themselves suffer further interactions in a cascade reaction known as Extensive Air Showers (EAS). More on EAS and ground-based detectors can be found in sections

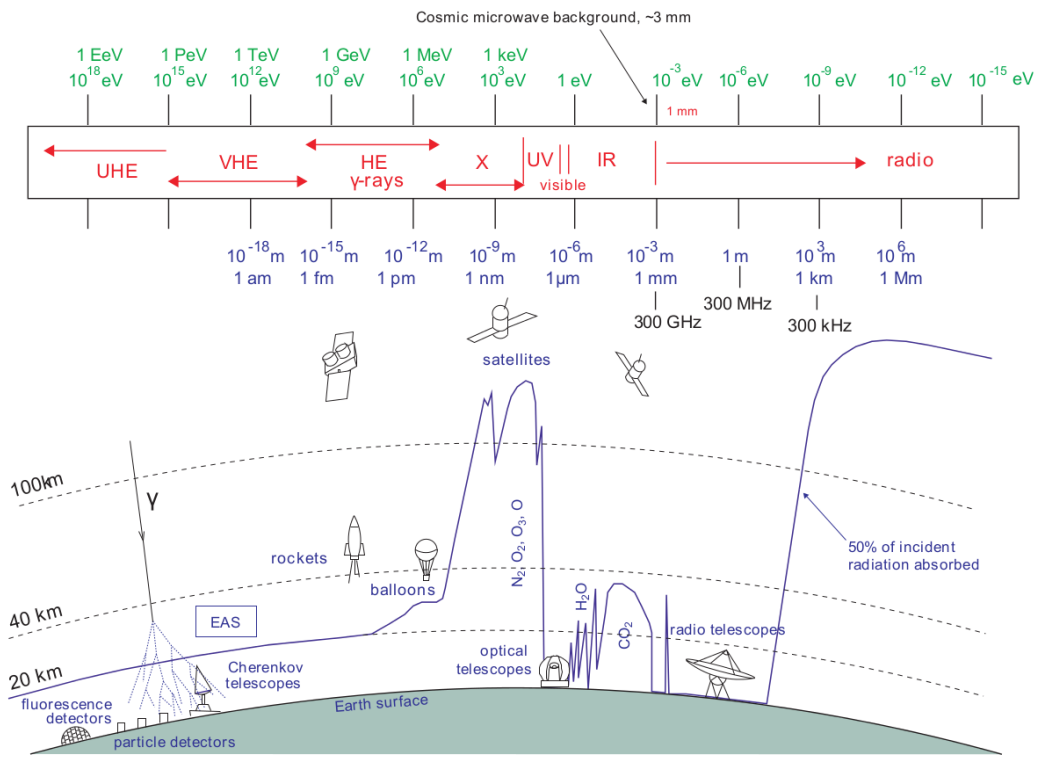


Figure 2.1: Atmospheric transparency for the whole electromagnetic spectrum, from [17]. The continuous line represents the height in the atmosphere where 50% of the light is absorbed.

2.2 and 2.4 respectively.

Space detectors and ground based detectors complement perfectly well, supplying the limitations of one another to cover the full  $\gamma$ -ray spectrum. Lower energy  $\gamma$ -rays are abundant, but so are hadronic backgrounds (Cosmic Rays (CRs)). Space detectors are perfectly suited to study these part of the spectrum, because beside their rather small collection areas ( $\sim 1\text{m}^2$ ), they have very good background rejection. At higher energies, the  $\gamma$ -ray flux decay strongly and much higher collection areas are needed. Ground based instruments detect the extended secondary products of  $\gamma$ -rays interacting in the atmosphere, they are designed to cover big areas, capturing even events from the highest energy  $\gamma$ -rays.

## 2.1 Space detectors

Direct detection of  $\gamma$ -rays can only be done outside the atmosphere, with particle detectors mounted in high altitude balloons or satellites. The main advantage of

these kind of detectors is the extremely efficient background rejection, being relatively easy to veto charged cosmic particles and distinguish them from neutral  $\gamma$  photons. However, they are limited in the energy of the  $\gamma$ -rays they can observe, not being able to go much further 100 GeV (High Energy (HE) regime) because of the technical difficulties to have a large collection area. The collection area corresponds to the size of the detector, which for space instruments is about  $1\ m^2$ , hindering the capture of Very High Energy (VHE) photons which flux decreases rapidly with energy.

In this section, different types of space detectors are described.

### 2.1.1 Compton detectors

Compton scattering occurs when a photon transfers part of its energy to an electron. At the low end of the  $\gamma$ -ray energy range (from 20 keV to 30 GeV) this is the process that dominates interactions between light and matter. Compton detectors are based on this interaction. Usually, they count on two parts: In the first level, the interaction between the  $\gamma$  photon and an electron occurs inside a scintillator. The trajectory deviation of the photon is measured, and then is possible to reconstruct its original direction. Afterwards, the photon travels to a second level where it is absorbed by a calorimeter and its energy is measured. The Imaging Compton Telescope (COMPTEL) instrument from the Compton Gamma Ray Observatory (CGRO) was operative between 1991 and 2000 and was able to do a survey of the galactic plane using this technique, detecting more than 60 sources (figure 2.2). Currently, the Imager on-Board the INTEGRAL Satellite (IBIS) [125] telescope [126] is the present representative of this kind of detectors.

### 2.1.2 Pair production detectors

A photon travelling with an energy over twice the rest mass of the electron (511 keV, usually photons over 20 GeV) passing close to a nucleus have a high probability to undergo through pair production process, giving rise to an electron-positron pair. Pair production detectors account for different layers of a heavy material where the interaction takes place, interleaved with a tracker material which measures the position of the resulting particles, being able to reconstruct the original direction of the  $\gamma$ -ray. A calorimeter measures the energy of the particles and an anti-coincidence detector acts as veto for the background of charged particles (CRs) which can enter the detector. A very prolific instrument of this kind, still on going, is the Large Area Telescope (LAT) instrument, on the Fermi Gamma-Ray Telescope which is formerly described in the next section.

#### The Fermi Gamma-ray Space Telescope

The Fermi Gamma-ray Space Telescope was launched in 2008 with the goal of performing a sky survey in the HE range. It follows a low Earth orbit, being able to observe the whole sky in 3 hours. It counts with two instruments: The LAT, which is the principal instrument for  $\gamma$ -ray detection, and the Gamma-Ray Burst Monitor

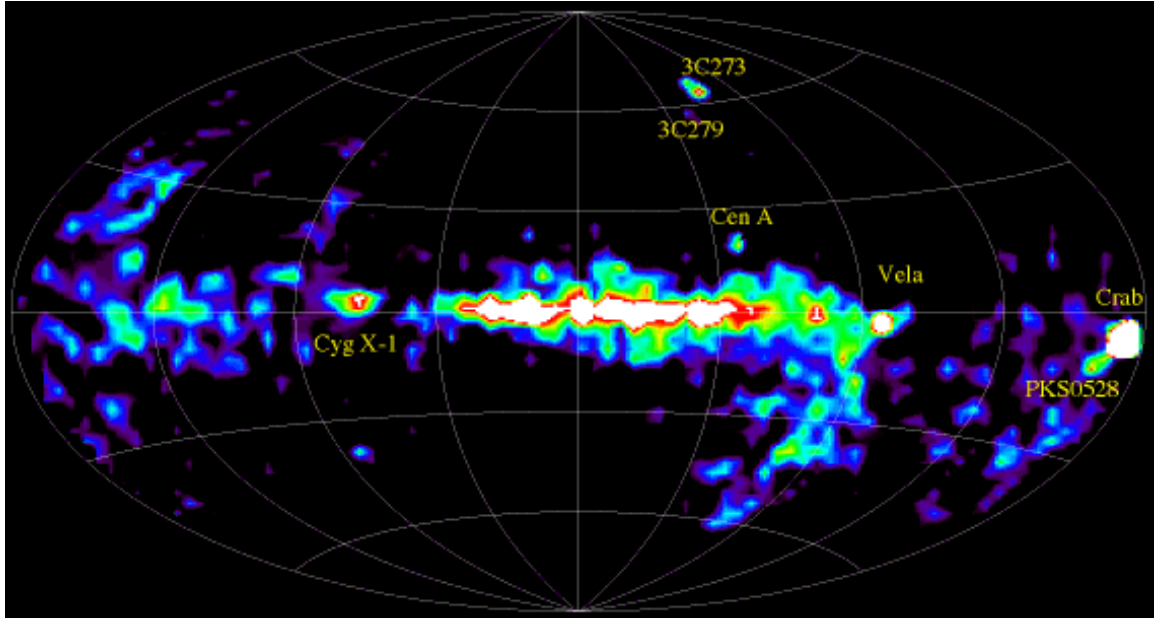


Figure 2.2: Skymap from COMPTEL source catalog. Credits to NASA.

(GBM), which is designed to detect Gamma Ray Bursts (GRBs).

- **The LAT:** This is the principal instrument of the Fermi telescope, a pair production  $\gamma$ -ray detector able to observe photons with energies from 20 MeV to more than 300 GeV [127]. It consists of 16 modular towers with 18 tungsten converter layers, where the pair production takes place, and 16 dual silicon tracker planes which measure the trajectory of the  $e^\pm$  pair. The 16 calorimeter modules have 96 long, narrow CsI scintillators which measure the deposited energy. When any particle enters the detector, it first passes through an anticoincidence plastic scintillator where, if it is a charged particle, it will produce a flash of light, making it possible to distinguish it from true  $\gamma$ -ray events.
- **The GBM:** Complementary to the LAT, the GBM is destined to detect GRBs and quickly alert the main instrument to reposition towards its direction. It is sensible to X-rays and  $\gamma$ -rays in the range between 8 keV to 40 MeV. The detector includes 12 Sodium Iodine (NaI) scintillation detectors which cover the lower part of the spectrum (up to 1 MeV) and provide the burst trigger, and 2 Bismuth Germanate (BGO) scintillation detectors with an energy range from  $\sim 150$  keV to  $\sim 30$  MeV, aimed to overlap the LAT energy range.

The principal scientific goals of Fermi are the study of unidentified sources detected by previous instruments like Energetic Gamma Ray Experiment Telescope (EGRET); understanding the mechanisms of particle acceleration in Supernova Remnants (SNRs) and GRBs; studying the behaviour of GRBs; performing indirect searches of Dark Matter and using  $\gamma$ -rays to probe the early universe and cosmic evolution of HE

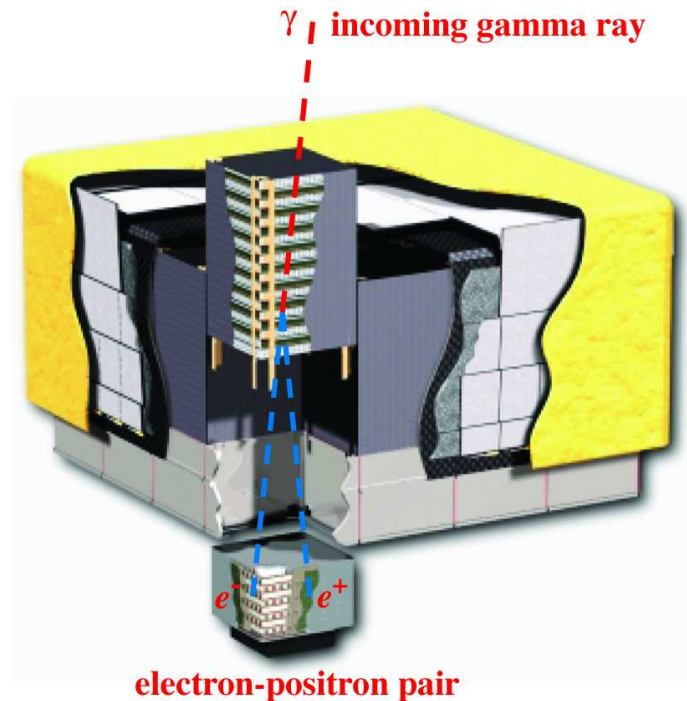


Figure 2.3: Schematic picture of the LAT from [127]. Dimensions are  $1.8 \text{ m} \times 1.8 \text{ m} \times 0.72 \text{ m}$ .

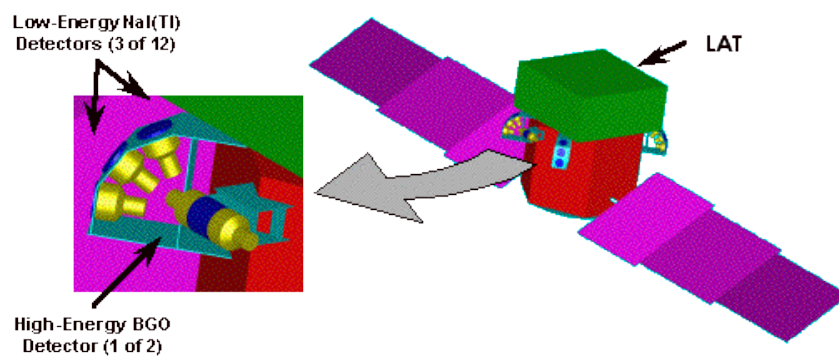


Figure 2.4: Schematic picture of the GBM integrated between the LAT and the shroud envelope of the Fermi's spacecraft.

sources.

During the more than 10 years of data taking up to date, the *Fermi*-LAT has been extremely prolific, launching several catalogs with thousands of sources. The 4FGL catalog is the last one released, based on the first 8 years of science data. It counts with 5065 detected sources above  $4\sigma$ , 1337 of which do not have a counterpart in other wavelengths.

Some of the scientific highlights during its lifetime are the discovery of the Fermi Bubbles (see section 1.6.1); the detection of hadronic signals in SNRs [128]; the detection of the most luminous GRB ever observed GRB130427A [129] and the detection with the GBM of the GRB after the LIGO event GW170817 [130], among many more.

## 2.2 Extensive Air Showers

As explained in the beginning of this chapter, the atmosphere absorbs the totality of the  $\gamma$  radiation coming from space. Any  $\gamma$ -ray entering the atmosphere will interact with an atomic nucleus triggering the production of a cascade of particles known as EAS. Furthermore, not only  $\gamma$ -rays can produce EAS, but CRs too, being in fact the responsible for the majority of EAS happening in the atmosphere ( $> 99\%$ ). The products of these cascades, whether being secondary particles or Cherenkov radiation (see section 2.3), are the targets for ground based  $\gamma$ -ray detectors. Depending on the type of detector, different techniques are required to reconstruct the energy and direction of the primary particle, in addition to distinguish between electromagnetic (produced by  $\gamma$ -rays) and hadronic (produced by CRs) showers. In this section, the characteristics and physical processes produced in the different types of EAS are described.

### 2.2.1 Electromagnetic Showers

When a primary  $\gamma$ -ray enters the atmosphere, it will produce a pair of  $e^\pm$  in the electric field of an atomic nucleus, typically after traversing one radiation length ( $\xi_0$  defined as the mean distance for a charged particle to reduce its energy by a factor  $e$  due to interactions with the medium), at about 20 km of altitude. This pair of particles, emitted in the forward direction will again interact with other atmospheric nuclei through bremsstrahlung, producing high energy photons. The result is a chain of pair production-bremsstrahlung processes, where a certain amount of energy is lost in each interaction, until the high energy photons reach a critical energy  $E_c \sim 83$  MeV. When this happens, ionization and Compton scattering of electrons and positrons become dominant over bremsstrahlung so the production of high energy photons is reduced until the shower slowly dies. Since the angle of emission in all the processes is proportional to  $\propto m_e c/E$  rad, the shower will not spread too much laterally, from an axis pointing towards the primary direction [20].

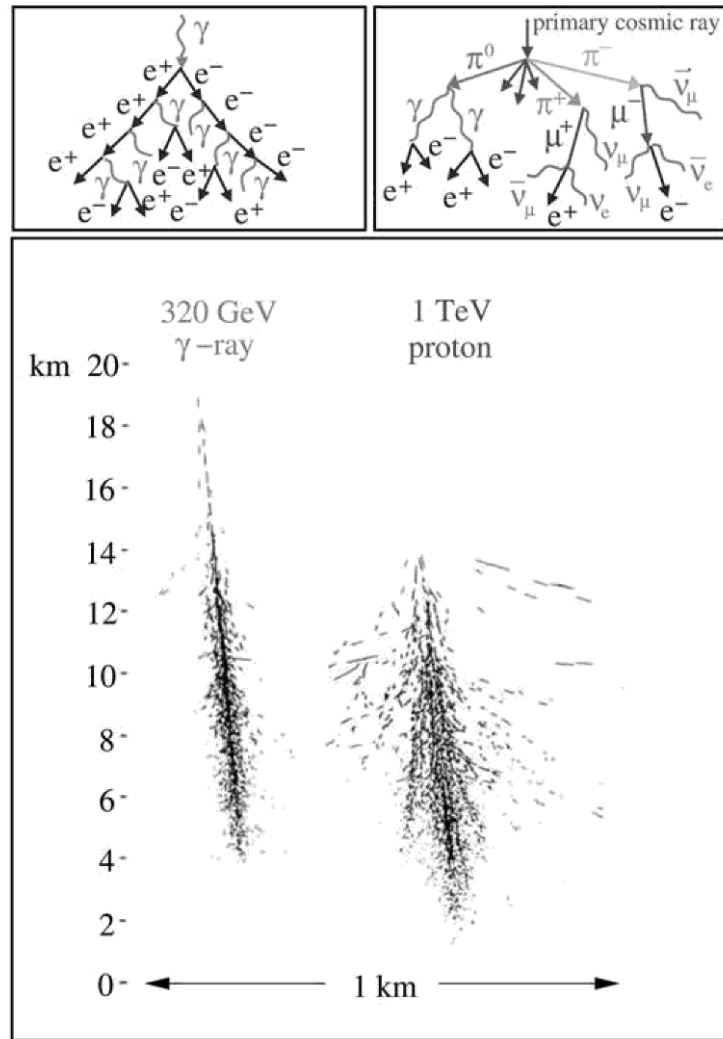


Figure 2.5: Montecarlo simulations of a 320 GeV  $\gamma$ -ray shower and a 1 TeV proton shower from [20]. The top panel show a schematic diagram of shower development with their secondary particles.

To understand in a simple way the evolution of the shower, It can be considered that it develops in discrete steps of one radiation length, just as in the model from [131]. The radiation length for the  $e^\pm$  pair is going to be close to the mean free path of photons of similar energy ( $\simeq 9/7\xi_0$ ) which for the air is  $36.7 \text{ g cm}^{-2}$ . Defining the atmospheric thickness as  $R=\xi_0 \ln 2$ , the probability of a photon, electron or positron of the shower to interact while traversing a longitude  $R$  will be  $\exp(-R/\xi_0) = 1/2$ . Since the distribution of energy in each step between the charged particles and the emitted high energy photon is considered symmetric, after traversing a thickness  $nR$ , the number of surviving  $e^\pm$  and photons will be  $2^n$ , and their mean energy  $E_\gamma/2^n$ , where  $E_\gamma$  is the energy of the primary  $\gamma$ -ray. When the energy reaches the critical energy  $E_c$ , the shower has reached the shower maximum, where the total number of particles is  $E_\gamma/E_c$ . The position of such maximum is:

$$X_{max} = \frac{R}{\ln 2} \ln \frac{E_\gamma}{E_c} = \xi_0 \ln \frac{E_\gamma}{E_c} \quad (2.1)$$

The shower maximum depends on the energy of the primary: higher energy photon showers penetrate more deeply in the atmosphere than lower energy showers, hence in order to lower the energy threshold of a ground based detector it must be located at high altitudes.

An analytical approach to shower development was carried out in [132]. The Greisen equation defines the number of electrons, positrons and photons in the shower before reaching the critical energy:

$$N_e(t) = 0.31 \left[ \log \frac{E_\gamma}{E_c} \right]^{-1/2} e^{T[1-(3/2)\log s]} \quad (2.2)$$

Where  $T$  is defined as the atmospheric depth expressed in radiation lengths, and  $s$  is the shower age parameter:

$$s = \frac{3T}{T + 2 \ln \left[ \frac{E_\gamma}{E_c} \right]} \quad (2.3)$$

The age parameter  $s$  indicates the degree of development of the shower, being equal to 0 at first interaction, 1 in the shower maximum and 2 in the dying point.

While  $N_e$  describes the longitudinal distribution of the shower, the lateral distribution is given by the Nishimura-Kamata-Greisen function:

$$f(r) = \frac{\Gamma(4.5-s)}{\Gamma(s)\Gamma(4.5-s)} \frac{N_e}{2\pi r^2} \left[ \frac{r}{r_m} \right] \left( 1 + \frac{r}{r_m} \right)^{s-4.5} \quad (2.4)$$

Where  $r$  is the distance from the shower longitudinal axis and  $r_m$  is the Molière radius, characteristic from multiple scattering theory, and  $\Gamma$  is the gamma function.

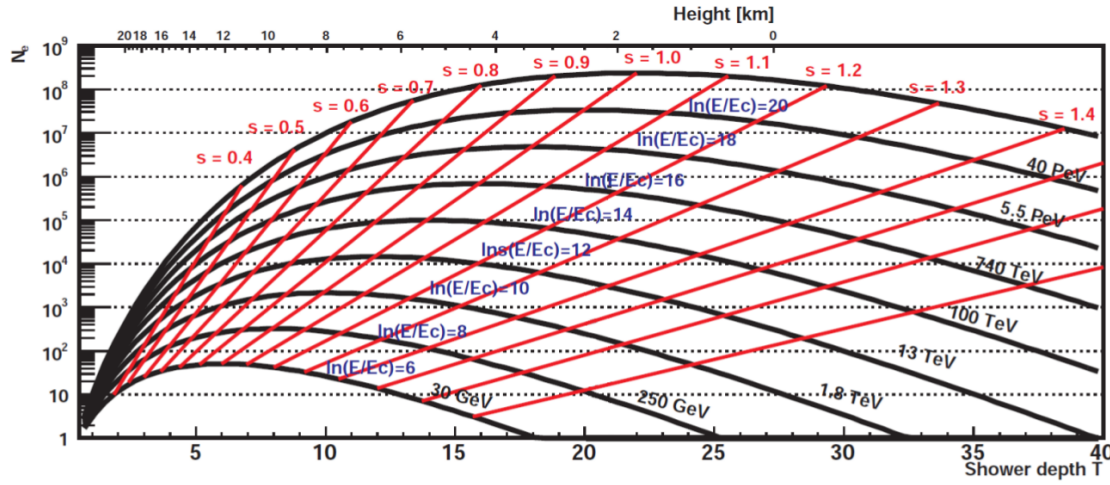


Figure 2.6: Longitudinal development of an electromagnetic shower in the Greisen approximation, from [133] and [134].

### 2.2.2 Hadronic showers

Hadronic showers are produced by CRs, mostly protons, colliding with atmospheric particles. Their development is substantially different from electromagnetic showers, since they produce a vast number of secondary particles of different nature (see figure 2.5) mainly fragments of atomic nucleus, pions and kaons, which end up decaying into muons and neutrinos. Hadronic showers have three components:

- **Hadronic core:** In the first interaction, a relativistic CR collides with a nucleus (O, N...) fragmenting it into smaller nucleons and transferring energy to them, which on their side keep colliding with other particles. They also produce charged mesons in each interaction ( $\pi$  and K mesons). Hadronic interactions will continue until the energy per nucleon becomes smaller than the pion production threshold around 1 GeV.
- **Electromagnetic component:** Around 90% of the particles generated in hadronic showers are pions, of which 1/3 are  $\pi^0$ . Neutral pions decay into two HE photons which generate pure electromagnetic showers. Charged K mesons can also decay into neutral pions through  $K^\pm \rightarrow \pi^\pm + \pi^0$ .
- **Muon and neutrino component:** Charged mesons can also decay into muons and neutrinos through  $\mu^\pm \rightarrow \nu_\mu(\bar{\nu}_\mu)$ . Muons traversing the atmosphere will only lose energy through ionization due to their long life and their small bremsstrahlung cross-section. They will decay into electrons/positrons and neutrinos through  $\mu^\pm \rightarrow e^\pm + \nu_e(\bar{\nu}_e)$  after a time of  $2.2 \cdot 10^{-8}$  s in their own reference frame, but due to their high Lorentz factor, time dilation can make

them reach ground level without decaying at all.

Despite their complexity, a model can be assumed to describe the evolution of hadronic showers, similar to the one for electromagnetic EAS. In the superposition model from [135] it is assumed that the shower induced by a nucleus of mass A and energy  $E_0$  is equivalent to A independent nuclei of energy  $E_0/A$ . The shower maximum in this case would be:

$$X_{max} \propto \xi_N \ln \left( \frac{E_0}{AE_c} \right) \quad (2.5)$$

Where  $E_c$  is the critical energy and  $\xi_N$  is defined as the mean path which reduces the number of relativistic charged particles by a factor  $1/e$  as they pass through matter, which for a proton of 1 TeV is  $83 \text{ gcm}^{-2}$ . Because  $\xi_N$  is larger than the radiation length for photons  $\xi_0$ , the altitude of first interaction of hadronic showers is higher than electromagnetic showers and they are able to penetrate deeper into the atmosphere. Furthermore, hadronic interactions are able to transfer considerable transverse momentum to the secondary products of the showers making them to disperse laterally. Also, hadronic showers are more irregular and present large fluctuations. These features are used in detectors to distinguish between electromagnetic and hadronic induced showers.

### 2.2.3 Electronic showers

There exist a third type of EAS produced by cosmic electrons and positrons entering the atmosphere. The type of cascade produced is very similar to electromagnetic showers, since the same processes take place: The electron/positron produces HE photons via bremsstrahlung while interacting in the electromagnetic field of atmospheric nuclei and those resulting photons produce  $e^\pm$  pairs. The main differences with electromagnetic showers have to do with the nature of the primary: Since it is a charged particle, interactions start just when it enters the atmosphere so the shower maximum is reached at higher altitudes. Also, it will be more affected by the deviations produced by the geomagnetic field of the Earth.

## 2.3 Cherenkov radiation

The Cherenkov radiation is a kind of electromagnetic radiation which is emitted when a charged particle travels through a dielectric medium at a velocity higher than the local speed of light. Many scientists during the XX observed that when a transparent material was placed in the neighbourhood of strong radioactive sources, they emitted a faint bluish light. From 1934 to 1938 Pavel Alekseyevich Cherenkov carried out a series of exhaustive experiments to try to explain the causes of this effect, named after him, and was awarded with the Nobel Prize in 1958 for his results.

Cherenkov radiation is a very important effect for ground-based  $\gamma$ -ray detectors

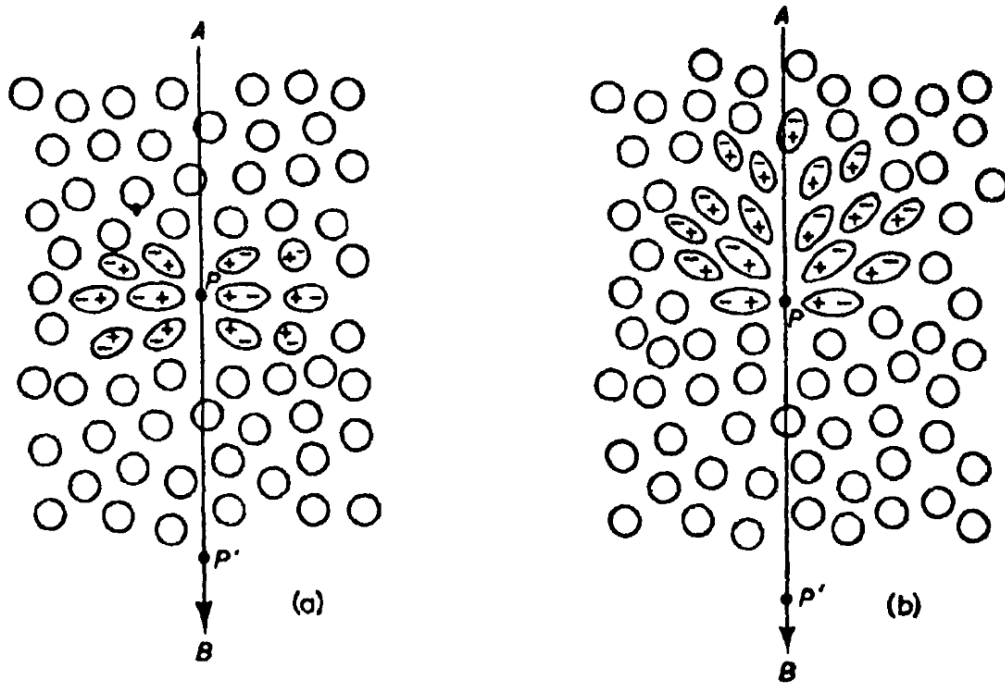


Figure 2.7: Polarization of a dielectric material at the passing of a charged particle by the point  $P$  at a) low velocity b) high velocity. Image from [136].

because EAS, which contain a large number of relativistic charged particles, are able to produce this kind of radiation in the atmosphere. Characterization of the Cherenkov signal from EAS allow to trace back the nature of the primaries.

This effect can be explained through the reaction of the atoms of a material when a charged particle is traveling through it. For example, in the case of an electron travelling through a glass, if the electron is travelling at a slow velocity, along its trajectory the electric field of the particle will distort the atoms, attracting the positively charged nucleus and repelling the negative electrons (see figure 2.7 a). The medium becomes polarized around the position of the particle, each atom behaving like a dipole and the region of the glass receiving a small electromagnetic pulse. Since the distribution of dipoles is symmetric, there will not be a resulting field thus no radiation will be emitted.

In the case the electron travels almost at the velocity of light in the medium the resulting field is not symmetric anymore along the direction axis of the particle (see 2.7 b). The dipole field will be noticeable even at long distances and the electron will produce the emission of wavelets of radiation at each point of its trajectory. In general, those wavelets will interfere destructively so that the resulting intensity of the field will be zero. If the velocity of the electron is higher than the speed of light in the medium, the wavelets can be in phase and produce a global field visible in the distance and thus, emit radiation. Figure 2.8 shows a diagram of a Huygens

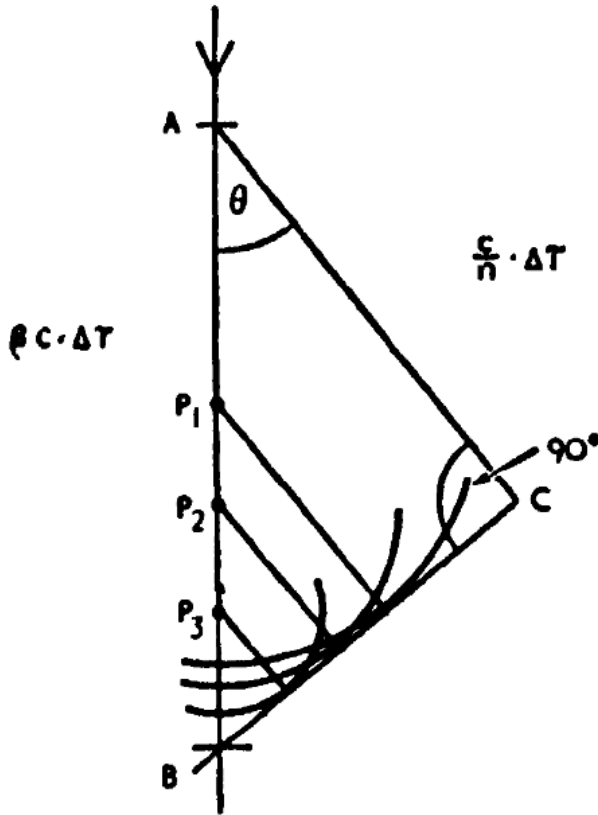


Figure 2.8: Diagram of Huygens construction showing coherence of waves emitted by a charged particle travelling faster than the speed of light in the medium, from [136].

construction of this effect. If a particle travels from A to B faster than the speed of light in the medium, it can travel that distance in the same amount of time that light will go from A to C, therefore when seen under an angle  $\theta$  all the waves emitted along the trajectory will be in phase and form a plane wave from B to C.

The angle  $\theta$  is named Cherenkov angle and can be expressed as:

$$\cos \theta = \frac{1}{n\beta} + \frac{\hbar k}{2p} \left( 1 - \frac{1}{n^2} \right) \quad (2.6)$$

Where  $\beta = v/c$ ,  $k$  is the emitted photon momentum,  $p$  is the charged particle momentum and  $n$  is the refractive index of the medium. Since  $p \gg k$ , the expression can be simplified to:

$$\cos \theta = \frac{1}{n\beta} \quad (2.7)$$

The Cherenkov light produced by EAS in the atmosphere will be emitted in the shape of a cone around the axis of the shower, leaving a ringlike signal when reaching

the ground. Because the refractive index of the atmosphere changes with altitude, the maximum angle will also vary and so the extension of the ring and the minimum energy required by a particle to produce Cherenkov radiation (when  $v = c/n$ ). The variation of the refractive index with altitude can be approximated by:

$$n(h) = 1 + n_0 e^{-\frac{h}{h_0}} \quad (2.8)$$

Where  $n_0$  is  $2.9 \times 10^{-4}$  and  $h_0 = 7.1$  km for an isothermal atmosphere, and the minimum energy:

$$E_{min} = \frac{m_e c^2}{\sqrt{1 - \beta_{min}^2}} = \frac{m_e c^2}{\sqrt{1 - (1/n)^2}} \quad (2.9)$$

Hence the minimum energy as a function of altitude:

$$E_{min} \approx \frac{m_0 c^2}{\sqrt{2n_0}} e^{\frac{h}{2h_0}} \quad (2.10)$$

and the maximum angle  $\theta$ :

$$\theta_{max} = \sqrt{(2n_0)} e^{-\frac{h}{h_0}} \quad (2.11)$$

This dependency means that at higher altitudes, the maximum angle is lower, so the Cherenkov signal in the ground will be less spreaded. Also, the minimum energy lowers with altitude, meaning that more developed EAS will more likely produce Cherenkov light.

About the spectrum of Cherenkov light in the atmosphere, while it could go from infrared to ultraviolet, photons below 290 nm are absorbed by ozone ( $O_3$ ), and over 800 nm by  $H_2O$  and  $CO_2$ . Also it suffers Rayleigh dispersion and aerosol dispersion. As a result, the peak of the spectrum at a detection altitude of about 2km is around 300 nm (blue light). The Cherenkov spectrum produced by a particle with charge  $z$  and velocity  $\beta$  is:

$$\frac{d^2N}{dxd\lambda} = \frac{2\pi\alpha z^2}{\lambda^2} \left( 1 - \frac{1}{\beta^2 n^2(\lambda)} \right) \quad (2.12)$$

## 2.4 Ground-based detectors

Ground-based detectors work capturing the products of EAS generated by primary  $\gamma$ -rays in the atmosphere. As explained in previous sections, EAS produce a cascade of particles which at the same time, emit Cherenkov light. There are two main types

of ground based detectors: Particle detectors, which capture the particles produced in the shower, and Cherenkov detectors, which measure the Cherenkov light. Because both  $\gamma$ -rays and CRs produce showers, the biggest challenge for ground based detectors is to differentiate the two kinds of events, being the background rejection less efficient than for space detectors. A proper knowledge of the differences in the development of electromagnetic and hadronic showers is crucial for this task. In general, ground based instruments take advantage of very precise Montecarlo simulations of EAS to find features in the signals which can help to do the  $\gamma$ /hadron separation.

#### 2.4.1 Particle detectors

Particle detectors measure the particles and secondary photons produced by EAS. Because the shower maximum depends on the energy of the primary, as seen in equation 2.1, only  $\gamma$  rays with extremely high energies can produce showers that reach the ground. In order to lower the energy threshold of detectors is necessary to place them at high altitudes (over 2000 m).

- **Particle counter matrices detectors** are classic particle detectors which record the arrival time of particles and direction to reconstruct the shower and eventually the primary characteristics. Examples of this kind of experiments are CASA-MIA [137], LHAASO-KM2 [138], Tibet-AS [139] and HEGRA [140].
- **Water Cherenkov detectors** are other kind of particle detector. They consist on a large number of big water tanks where particles from the shower produce Cherenkov light. ARGO-YBJ [141] and HAWC [142] are examples of this kind of detector.

The advantage of particle detectors is that they can be extended over hundreds of square meters, covering a very wide field of view. Also, they can work anytime, even under daylight. In general, they cover the higher energy range, being able to reach hundreds of TeV.

#### 2.4.2 Atmospheric Cherenkov Telescopes

Cherenkov photons produced by EAS in the atmosphere account for  $10^{-4}\%$  of the Night Sky Background (NSB) and they can be observed from the ground as flashes of around 10 ns. For that reason, unlike particle detectors, they require very clear and dark moonless nights, to differentiate Cherenkov photons from any background light. There are two types of atmospheric Cherenkov telescopes:

##### **Sampling detectors**

They consist on a grid of counters which measure the Cherenkov light from EAS at ground level with low-gain Photomultiplier Tubes (PMTs). The direction of the primary can be determined measuring the timing signals from the photons detected,

and the energy is reconstructed from the lateral distribution of the Cherenkov light. The energy threshold for these kind of detectors is high, being suitable for the study of VHE and Ultra High Energy (UHE)  $\gamma$ -rays. For example, the minimum energy threshold of the Air shower Observation By angle Integrating Cherenkov Counters (AIROBICC) was 20 TeV [143]. For sampling detectors, differentiating  $\gamma$ -ray showers from hadronic is truly problematic, and currently they have been outperformed by Imaging Atmospheric Cherenkov Telescopes (IACTs).

### **Imaging Atmospheric Cherenkov Telescopes (IACTs)**

IACTs are the most prolific type of ground based  $\gamma$ -ray detectors and their evolution is the key for the next generation of VHE  $\gamma$ -ray astrophysics.

They work similar to optical telescopes, with a large mirror which collects Cherenkov light into a camera, that records images of the showers. Because Cherenkov light flashes are very short, cameras need to be very fast to take snapshots of just a few nanoseconds. Also, as the number of photons of the NSB is very high compared to the small number of Cherenkov photons, is essential to have a very precise time correlation between camera pixels, given by state-of-the art electronics, to reject random signals from NSB and get the time evolution of the showers.

The reconstruction of the energy and incident direction of the primary photon as well as the separation of  $\gamma$  and hadron events can be achieved through a parametrization of the shower images, based on the work done by Michael Hillas [144]. With this method, the moments of the observed light distribution in the camera, which for  $\gamma$ -rays looks like an ellipse (named Hillas ellipse), are used as parameters to characterize the shower, which subsequently allow to distinguish between  $\gamma$  and hadronic showers. The intensity of Cherenkov light in the image is directly proportional to the energy of the primary and the orientation of the ellipse can be used to reconstruct their direction of arrival. Several techniques are used to reconstruct the primary information from Hillas parametrization, most of them based on modern Machine Learning algorithms.

Other techniques make use of the entire information of the camera image, comparing pixel by pixel with a template generated by a semi analytical model of shower development. A detailed summary on reconstruction methods for Cherenkov Telescopes can be found in [145] and [146].

Either of the techniques improve substantially when using stereoscopy, taking shower images with several telescopes at the same time. This not only improves the reconstruction power, but also helps rejecting the hadronic background very efficiently. When pointing the telescopes to a  $\gamma$ -ray sources, in general, shower images from  $\gamma$  primaries will be oriented towards the position of the source in the cameras of all telescopes. Hadronic showers, which come from random directions in the sky, will point towards random directions in the camera, so they can be easily discarded.

The first telescope of this kind was the Whipple Observatory 10m reflector [147], with a camera of 37 pixels. It started operations in 1968 but it wasn't until 1988 that they detected the first  $\gamma$ -ray source, the Crab Nebula. The first stereoscopic

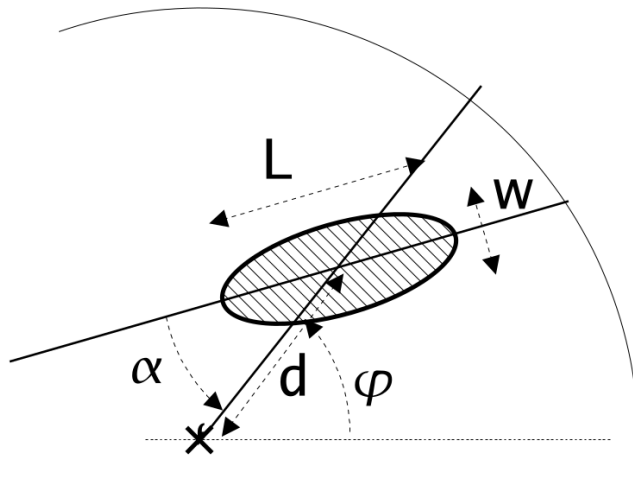


Figure 2.9: Geometrical definition of the Hillas parameters. L for Length (W for Width) is the RMS spread of light along the major(minor) axis of the image, it carries information of the longitudinal(lateral) development of the shower. Nominal distance d is the angular distance between the centre of the camera and the image centre of gravity. Angle  $\phi$  is the azimuthal angle of the image major axis and orientation angle  $\alpha$  is the angle between the major axis and the center of the camera. Figure from [145].

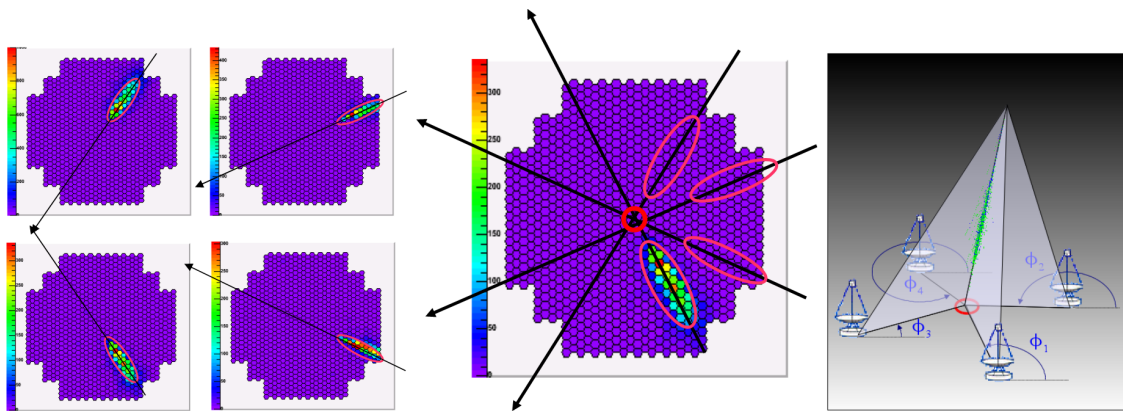


Figure 2.10: Geometric reconstruction of shower direction in stereo mode, from [146]. *Left and middle:* The shower image from 4 telescopes is combined to get the source position in the intersection of the main axis. *Right:* Intersection of the planes which contain the shower tracks and the telescopes give the shower Impact Parameter on the ground.

system was the High Energy Gamma Ray Astronomy (HEGRA) complex, with a total of six IACTs which worked together with other types of  $\gamma$ -ray detectors (like the AIROBICC).

The current generation of IACTs is formed by Major Atmospheric Gamma Imaging Cherenkov Telescopes (MAGIC) [148], High Energy Stereoscopic System (H.E.S.S.) [149] and Very Energetic Radiation Imaging Telescope Array System (VERITAS) [150] telescopes:

- **MAGIC:** The MAGIC telescopes are a set of two IACTs of 17 m diameter, located in the Roque de Los Muchachos Observatory at the Canary Island of La Palma, Spain. They are at an altitude of 2200 m, separated by 85 m. The first telescope, MAGIC-I, started operations in mono mode in 2004, and in 2009 the second telescope, MAGIC-II was included, becoming an stereoscopic system. An upgrade was made during the years 2011-2012, to reduce differences between both telescopes and improving the stereo performance.

The energy threshold of MAGIC can reach 25 GeV when using the *sum trigger* setup, becoming the most sensitive IACT system below 300 GeV in the northern hemisphere.

Due to their big size, the MAGIC telescopes are especially well suited to observe low energy events, which produce less Cherenkov photons and require bigger mirrors. This characteristic makes them especially ideal for observing high redshift Active Galaxy Nuclei (AGNs) and pulsars. Also, they were designed to be very light in order to be able to do a fast repositioning to follow up GRBs alerts. The MAGIC collaboration announced the first detection of a GRB in January 2019 [84].

During their fifteen years of operations the MAGIC telescopes have given prolific scientific results such as the detection in VHE of the Pulsar Wind Nebula (PWN) 3C 58, the one with the lowest luminosity and lowest flux ever detected in VHE  $\gamma$ -rays; the observation of  $\gamma$ -ray emission from a jet originated inside the event horizon of the central Black Hole (BH) of the galaxy IC 310; the detection of the galaxy PKS 1441+25, one of the two most distant galaxies detected at high energies; the detection of the Crab pulsar, located inside the well known Crab PWN; the detection of  $\gamma$ -rays from a gigantic explosion occurred in the galaxy QSO B0218+357 thanks to gravitational lensing; and the tracing of the source (the active blazar XS 0506+056) of a very rare cosmic neutrino event detected by IceCube experiment on September 2017 [151].

- **H.E.S.S.:** An array of 5 telescopes located in Namibia, close to the Gamsberg mountain, being the only IACT observatory in the southern hemisphere. The first four telescopes, operational since 2004, have 12 m diameter and are arranged in a square shape. The second phase of the experiment consisted in a fifth telescope of 28m of diameter, sitting in the center of the square. It was inaugurated in 2012 and contributed to lower the energy threshold. An update

in the cameras of the small telescopes was performed during the years 2015-2016 improving the performance of the whole array.

The energy range of H.E.S.S. goes from 30 GeV to 100 TeV, being the widest of IACT observatories.

Because it is located in the South, H.E.S.S. has been able to perform a galactic plane survey in VHE range, complementary to the HE survey done by *Fermi*-LAT (see picture 2.11). Some important scientific highlights of H.E.S.S. are the detection of the Vela pulsar and the colliding wind binary system Eta Carinae; the discovery of new SNRs in the galactic plane; the detection of VHE emission from the LMC P3 binary system discovered by *Fermi*-LAT, with a binary phase of  $\sim 0.3$ , being the most luminous binary system detected up to date; direct measures of the Extragalactic Background Light (EBL) spectral density thanks to the observations of a large number of AGN spectra; and observation of flares and variability in the AGNs Mrk 501 and 3C 279. A detailed summary on these topics among many more scientific highlights of H.E.S.S. can be found in [149].

- **VERITAS:** Is an array of four IACTs located in the Fred Lawrence Whipple Observatory in southern Arizona. They are 12 m diameter telescopes arranged in a diamond shape and their design is based on the original Whipple 10 m Telescope. The first light of the VERITAS prototype was in 2004 and the full array started operations in 2007. In 2012 the cameras PMTs were upgraded to high-quantum-efficiency PMTs. The total energy range goes from 85 GeV to 30 TeV. Among the most important scientific results from VERITAS are the detection of pulsed emission from the Crab pulsar; Regarding the observations of blazars (AGN), the detection of rapid variability in the blazar BL Lacertae, the detection of the high redshift blazar ( $z \sim 0.6$ ) PKS 1424+240 above 0.1 TeV, the discovery of the source VER J0521+211 and deep observations of the distant 1ES 0229+200 ( $z = 0.14$ ); and the survey of the Cygnus region which allowed to resolve new sources and contributed with new candidates of counterparts at TeV energies to *Fermi*-LAT sources in the region. A summary on the most recent VERITAS highlights can be found in [150].

The future of ground based  $\gamma$ -ray astronomy is in hands of the Cherenkov Telescope Array (CTA) currently in construction. CTA will be a  $\gamma$ -ray observatory without precedents, as the result of combined efforts of scientists from all over the astroparticle physics community. It will have two locations, one observatory in the northern hemisphere in the island of La Palma, Spain, and the other in the south, in the Atacama desert, Chile. This will allow to do full sky observations, with a sensitivity one order of magnitude better than the current generation of IACT observatories (see figure 2.12). An extended summary on CTA can be found in chapter 3.

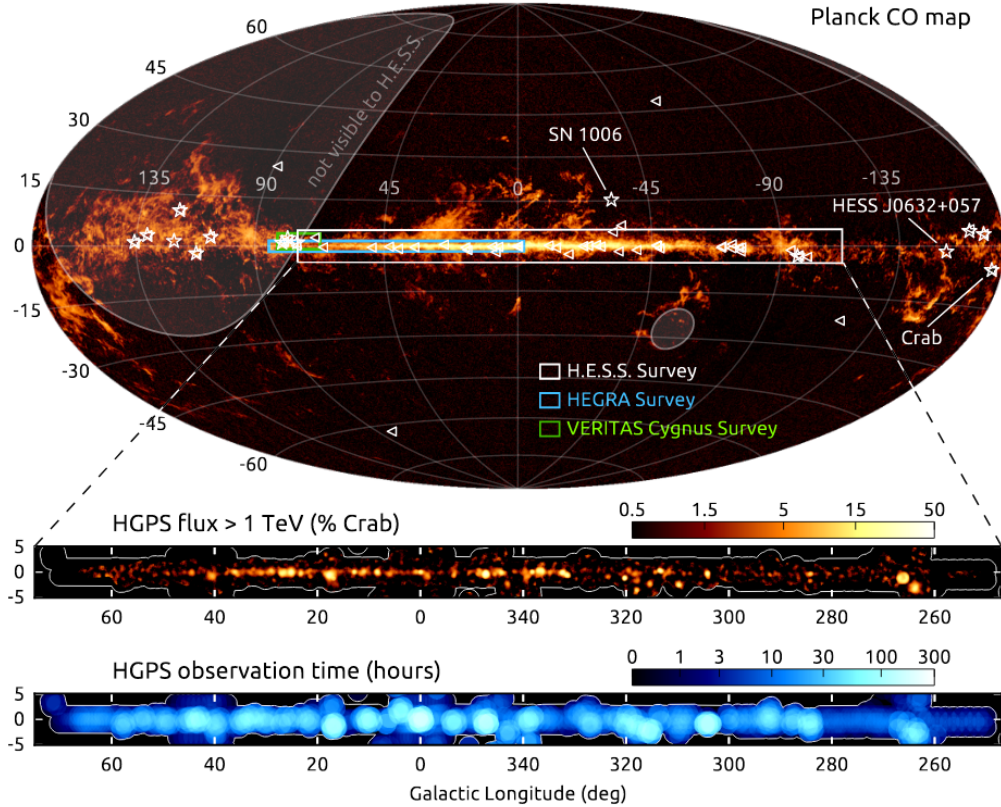


Figure 2.11: Illustration of the H.E.S.S. I galactic plane survey. The region surveyed is shown in the top panel as a white rectangle on top of the carbon monoxide gas sky map measured with the Planck satellite. Previous surveys from HEGRA and VERITAS are also represented. Triangles are sources detected at lower energies by *Fermi*-LAT and stars are galactic sources detected outside the survey region. Middle and lower panels show the observed flux and observation time. Picture from [149].

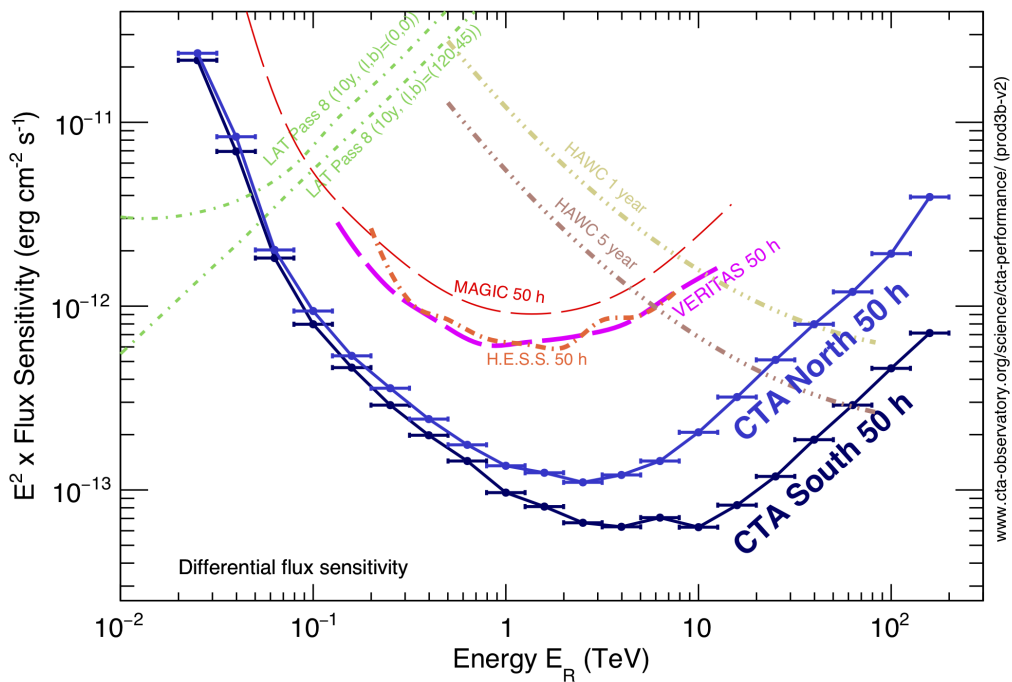


Figure 2.12: Differential sensitivity of CTA for 50 h observation compared to other  $\gamma$ -ray experiments, from [152].



### 3.1 Introduction

The Cherenkov Telescope Array(CTA)[153] is the next-generation ground-based observatory for  $\gamma$ -ray astronomy. It is the result of the combination of efforts from all the  $\gamma$ -ray community, to push the field of Very High Energy (VHE) astrophysics to new limits. It will consist on two observatories of Imaging Atmospheric Cherenkov Telescopes (IACTs) located in the Northern hemisphere, in the Roque de los Muchachos Observatory in the island of La Palma (Canary Islands, Spain) and in the Southern hemisphere in the Paranal desert (Chile). With this configuration, Cherenkov Telescope Array (CTA) will be the first ground-based observatory to be able to survey the full sky. CTA will have five to ten times more sensitivity than current instruments in the wider energy range ever reached, from 20 GeV to 300 TeV. Its fine angular resolution up to 2 arcseconds, with a field of view of  $\sim 10^\circ$  will allow the observation of fine structures in extended  $\gamma$ -ray sources. Its energy resolution with an uncertainty less than 10% will make CTA capable of study features in the sources spectra, such as lines and cutoffs.

To reach such improvements with respect to the current generation of IACTs observatories, CTA will count with more than 100 telescopes in three sizes, each designed to improve the performance in a specific spectral range. Large Size Telescopes (LSTs) have the bigger size, with a 32 m diameter mirror. They focus on the lowest part of the VHE spectrum ( $\sim 20$  GeV to 3 TeV) where  $\gamma$ -ray showers are common, so a small number of telescopes is enough, but the amount of Cherenkov light is low so large mirrors are required to collect the maximum number of photons. Medium Size Telescopes (MSTs) have an intermediate size, with a diameter of  $\sim 10$ m. They have the best performance at the range between  $\sim 100$  GeV and 50 TeV. Small Size Telescopes (SSTs) have much smaller mirrors ( $\sim 4$  m), and a large number of them

will be installed to get big collection areas and be able to capture the highest energy photons (up to 300 TeV), which are very rare but produce huge amounts of Cherenkov light.

Thanks to the large number of telescopes, CTA will have great flexibility of operations, with different observation modes: with full array for best sensitivity; using subarrays to observe several sources at the same time; and divergent pointing mode where the field of view can be extended up to 20 deg.

In this chapter the main features of CTA are covered. A description of performance is given in section 3.2. In section 3.3 the three types of telescopes are described in detail. Section 3.4 is dedicated to CTA data analysis techniques and tools at different levels.

## **3.2 CTA Requirements and Performance**

The current generation of Cherenkov telescope observatories consist on arrays of 2 to 5 telescopes which reach sensitivities of about 1% of the Crab flux at the range of 0.1-1 TeV. The typical angular resolution is about  $0.1^\circ$ , but it can improve largely for intense point sources (20-30 arc seconds). The goal of CTA design is to advance the state of the art in  $\gamma$ -ray astronomy, improving sensitivity, energy range, angular and timing resolution and offering full sky coverage. The performance goals of CTA are shown in table 3.1. As a result of these goals, CTA will account for two unique features: the ability to produce a deep survey of the VHE sky, discovering hundreds of new sources; and the possibility to observe the shortest time-scale phenomena, such as flares and jets from black holes in the center of active galaxies or periodic emission like such of pulsars. To achieve these improvements, different types of telescopes are required and they should be spreaded over large areas to reach a collection area of several  $\text{km}^2$  [154].

The final performance of CTA will depend on the design of the telescopes, which will be discussed more deeply in next sections, and also on the arrangement of them in the two sites. To have an estimate of the performance of the observatory and to decide which will be the best configuration detailed Monte Carlo simulations were made [155], comprising simulations of shower development in the atmosphere, detector response and event reconstruction. A deep study of these simulations [156] for different configurations of telescopes and sites was made to came up with the final array layout illustrated in picture 3.1.

The baseline design for Southern observatory foresees 4 LSTs, 25 MSTs and 70 SSTs. It will be dedicated to the study of galactic sources which emit the most energetic  $\gamma$ -rays that can reach the Earth. Because of the extremely low fluxes, it will cover very a large area ( $\sim 4 \text{ km}^2$ ), achieved thanks to the large number of SSTs, to capture as many events as possible.

The Northern observatory will mainly observe extragalactic sources and transient events from which only the less energetic photons reach the Earth due to absorption (see section 1.4). The final configuration will consist on 4 LSTs and 15 MSTs.

The performance of CTA has been evaluated in terms of the best results for

Diff. sensitivity (erg cm <sup>2</sup> s <sup>-1</sup> )	at 50 GeV at 1 TeV at 50 TeV	$8 \times 10^{-12}$ $2 \times 10^{-13}$ $3 \times 10^{-13}$ (S) / $3 \times 10^{-12}$ (N)
Collection area (m <sup>2</sup> )	at 1 TeV at 10 TeV	$> 10^4$ $> 10^6$ (S) / $> 5 \times 10^5$ (N)
Angular resolution	at 0.1 TeV $> 1$ TeV	0.1° 0.05°
Energy resolution	at 50 GeV $> 1$ TeV	$\leq 25\%$ $\leq 10\%$
Field of view	at 0.1 TeV at 1 TeV $> 10$ TeV	5° 8° 10°
Sensitivity in FoV	at 1 TeV flat out to at 1 TeV	$> 2.5$ ° 5" per axis
Repointing time	<0.1 TeV 0.1-10 TeV	20s (goal), 50s(max) 60s (goal), 90s (max)

Table 3.1: Performance goals for CTA observatories, adapted from [154]. Sensitivity given in 5 bins per energy. (N)= Northern site, (S) = Southern site.

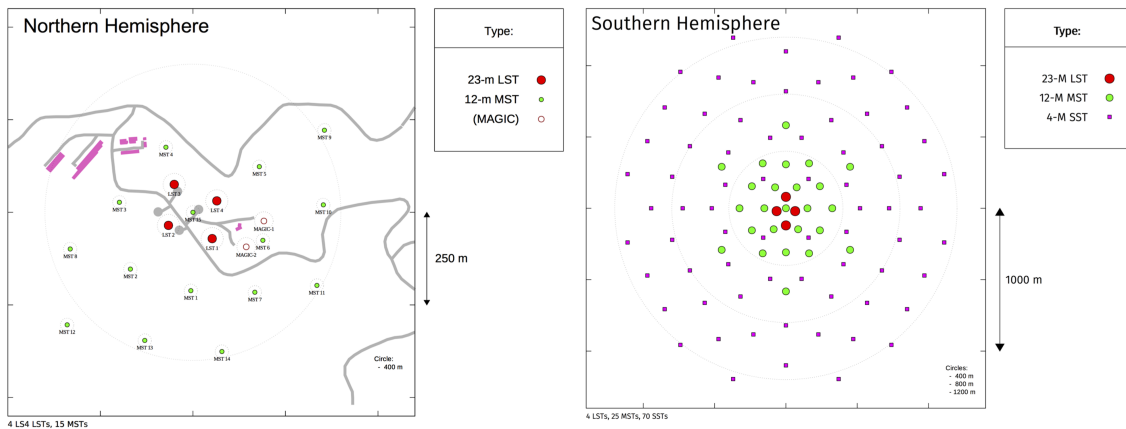


Figure 3.1: Array layout selected for CTA from [152]. Left is Northern site where also Major Atmospheric Gamma Imaging Cherenkov Telescopes (MAGIC) telescopes are located. Right is Southern location.

the observation of a point source located at the centre of the field of view of telescopes cameras. A set of metrics are taken into account: Effective collection area, residual cosmic-ray background rate, angular resolution and differential sensitivity. Usually they are calculated after applying cuts in *gammaness* and  $\theta^2$  optimized to maximize sensitivity for a set of typical observation times. Gammaness is referred to the gamma-hadron separation of shower events, events with higher gammaness are more likely to be produced by a  $\gamma$ -ray instead of a hadron. The angle  $\theta^2$  is the square of the angle between the reconstructed source position and the true source position. An overview of the mentioned metrics for performance evaluation is the following:

- **Effective collection area:** The effective collection area describes the area in which CTA is able to detect a shower from the point source. The effective collection areas for the assumed point sources are shown in figure 4.4.

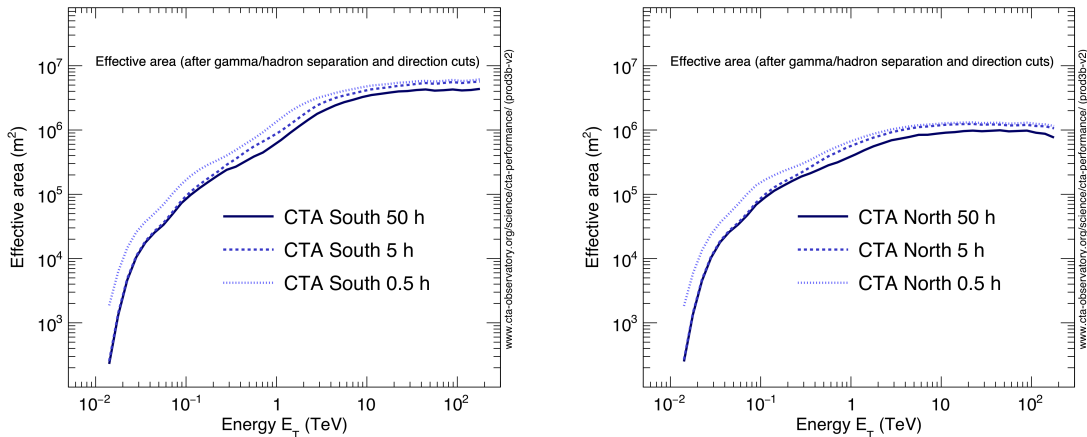


Figure 3.2: Effective collection area for point-like sources for CTA South(left) and CTA North (right) [152].

- **Residual cosmic-ray background rate:** The ability of CTA to reject background events, meaning showers produced by Cosmic Rays (CRs) instead of  $\gamma$ -rays is measured through the residual CR background rate. The 99.9% of the showers reaching the telescopes are produced by CRs, so a good background rejection is a key requirement for IACTs. In figure 3.3 the (post-analysis) residual cosmic-ray background rate per square degree vs reconstructed  $\gamma$ -ray energy is shown. The rate is integrated in each bin, where five bins per decade has been taken. CTA have such strong background rejection capabilities that the majority of the background in the range 0.2-1.5 TeV is due cosmic-ray electrons and positrons [157] which produce showers very similar to those produced by  $\gamma$ -rays (see section 2.2.3).

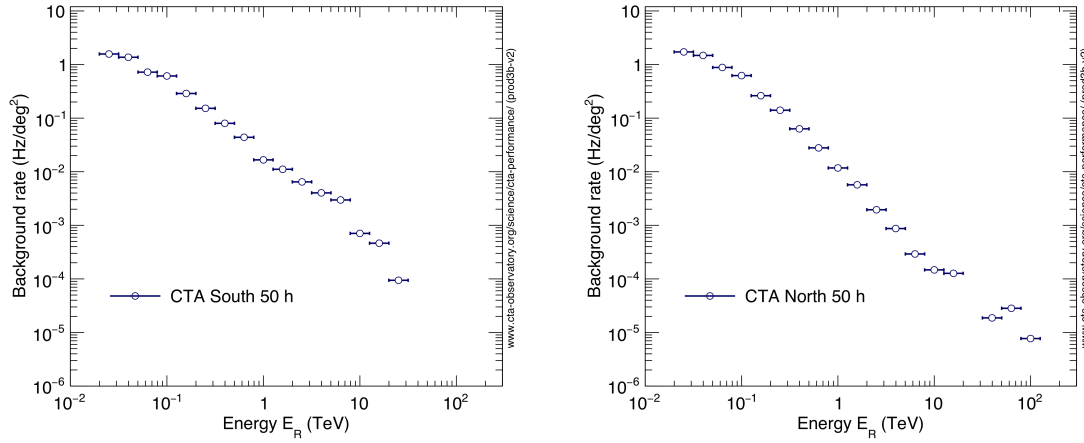


Figure 3.3: Residual cosmic-ray background rate vs reconstructed energy for CTA South(left) and CTA North (right) [152].

- **Angular resolution:** The angular resolution is defined as the angle within which 68% of reconstructed  $\gamma$ -rays fall, relative to their true direction. Figure 4.2 show the angular resolution vs. reconstructed energy optimized for best point-source sensitivity. It is possible to improve angular resolution at expenses of collection area for a better study of morphological features of bright sources.

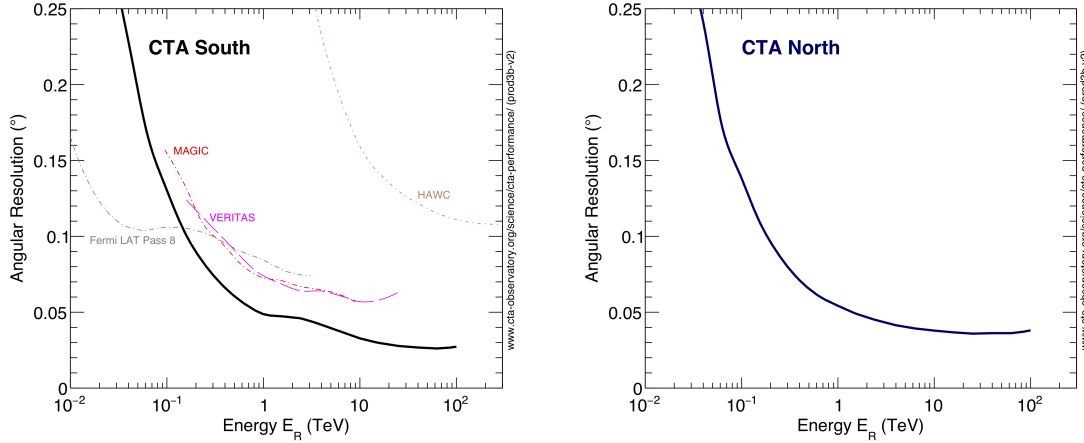


Figure 3.4: Angular resolution for CTA South compared to other experiments (left), and for CTA North (right) [152].

- **Energy resolution:** The energy resolution  $\Delta E/E$  is obtained from the distribution  $E_{rec} - E_{true}/E_{true}$ , where  $E_{true}$  and  $E_{rec}$  are the true and reconstructed energies of  $\gamma$ -ray events. It is defined as the half-width of the interval around 0 which contains the 68% of the distribution. The energy resolution of CTA as a

function of reconstructed energy is shown in figure 3.5. Note that for the range of 1-10 TeV the energy resolution is well below the required 10%.

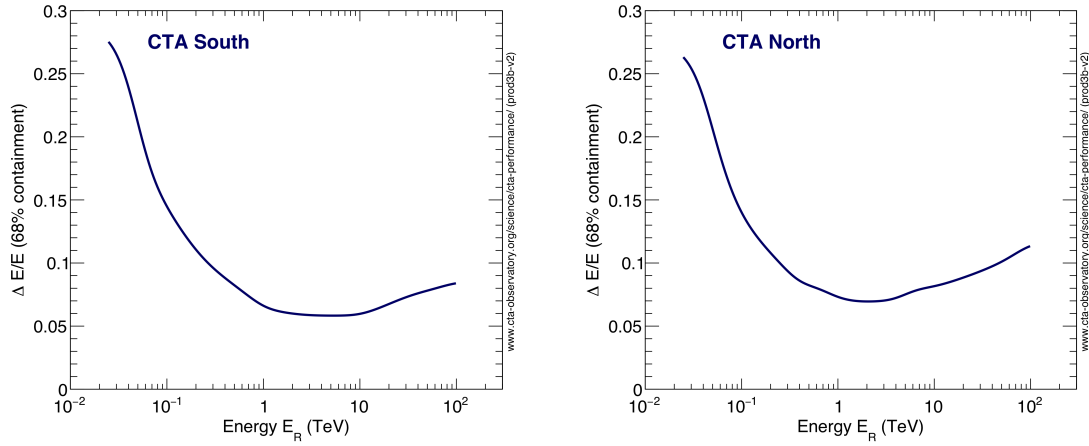


Figure 3.5: Energy resolution vs reconstructed energy for CTA South (left) and CTA North (right) [152].

- **Differential sensitivity:** The most important feature at evaluating the performance is the differential sensitivity, which indicates the minimum flux needed by CTA to detect a point-like source at  $5\sigma$ . The sensitivity is calculated in five energy bins per decade, where it is required that at least 10  $\gamma$ -rays are detected and the signal to background ratio is at least 1/20. The cuts in gammaness and source direction ( $\theta^2$ ) are optimized to improve this quantity. The differential sensitivity of CTA compared to that of other instruments for 50h observation time was shown in figure 2.12.

### 3.3 CTA Telescopes

While all telescopes share a basic design concept, each of them have particular features to accomplish the performance requirements for CTA. In general, subsystems of IACTs are divided in **structure**, **optics** and **camera**. In this section an overview of these subsystems and the particularities of each of the three types of CTA telescopes is given.

#### 3.3.1 Large Size Telescope (LST)

The purpose of the LST is to enhance the sensitivity of CTA at low energies, reaching an effective threshold down to 20-30 GeV. This energy range has a particular interest because it covers the barely explored gap between the highest energies detected by satellite experiments, and the lowest by IACTs. The main science goals for LSTs

are to observe high redshift Active Galaxy Nuclei (AGNs), Gamma Ray Bursts (GRBs), pulsars and galactic transients. The first prototype for the LSTs (LST1) has been installed in the CTA North site, in La Palma island, and is currently being commissioned.

A detailed description of LST subsystems can be found in [158], next sections offer a summary of the most remarkable features of the telescope.

### LST Structure

The structure of the telescope is divided in several parts: The azimuth system and substructure, the mirror support dish, the elevation system, the camera support structure and the drive system. All parts of the structure are specially designed to make the telescope lightweight, to ensure fast repositioning in the case of a transient alert (mainly GRBs).

The azimuth system allow the telescope to turn around its vertical axis. It consists in a circular rail of 24 m diameter where six wheeled bogies support the structure. The azimuth structure is a space framed structure made of carbon fiber reinforced plastic (CFRP) tubes. Its design is very similar to that of MAGIC telescopes, but much lighter. The mirror support dish is a double layer space frame made of CFRP tubes arranged in a tetrahedral structure. The diameter of the dish is 23 m and the focal length is 28 m. The elevation system consists on a structure made of heavier steel tubes, located in the backside of the dish, to help compensate the weight of the telescope structure. The camera support structure consists on an arch with three curved sections on each arm, made of CFRP. A total of 26 ropes stiffen the structure. The arch holds the camera frame, where the camera and the square lids are fixed. The drive system, designed to ensure a fast and precise repositioning, consists on 4 synchronous motors capable to supply a total mechanical power of 190 Kw to move the structure in azimuthal axis and elevation. The different parts of the structure are shown in figure 3.6.

### LST Optics

The mirror of the telescope has a parabolic shape, with 28 m diameter, and is segmented in 198 hexagonal mirrors of spherical shape. The structure is made in a way that it guarantees the isochronousity of the optics. The mirrors are manufactured using the cold slumped technique which, like a sandwich structure, is composed of a soda-lime glass sheet, an aluminum honeycomb box and another glass sheet[159]. Mirrors are fixed to the telescope structure by three knots, two of them mounted on actuators which allow to adjust each mirror panel in two directions. The *active mirror control* system controls these actuators in order to vary focal distance and focusing, to account for the possible deformations and bending of the telescope structure. Each mirror segment has an infrared laser, and two more lasers are mounted in the center of the disk, which constantly point to the left and right of the camera. The directional offset of the mirror facets can be estimated by taking pictures of the reflected spots



Figure 3.6: Left: Simplified diagram of the structures of LST without bogies, mirrors and camera. Azimuth substructure is blue color, the elevation system and the camera support structure are shown in green color and the mirror dish is red color, from [158]. Right: Photo of the first LST installed in CTA North site (Roque de los Muchachos Observatory, La Palma, Spain).

on a target in front of the camera with a high resolution IR CCD camera located in the center of the dish. The achievable positioning resolution can reach  $< 5\mu m$  [158].

### LST Camera

The camera focal plane instrumentation consist on 256 modules with seven Photomultiplier Tubes (PMTs) each, making a total of 1855 pixels. The PMTs are mounted with a 50mm spacing, surrounded by hexagonal light guides made of a very reflective material (3M ESR), to collect all the light arriving to the camera. The PMT model is Hamamatsu R11920-100-20, specially developed to reach high quantum efficiency (42%) and low after pulse rates, which go below 0.02 % above 4 photoelectrons. Each module with seven photodetectors has one readout system based on the Domino Ring Sampler version 4 (DSR4). The signal sampled at a rate  $\mathcal{O}(\text{GHz})$  is divided in three channels: high gain and low gain channels which are connected to the DSR4 chips and the trigger channel [159]. The two level trigger electronics (L0 and L1) are mounted on a mezzanine. A slow control board monitors the PMTs and analogue backplanes are dedicated to trigger and clock propagation. The mechanical structure of the camera consist on several parts, shown in figure 3.7. The modules are coupled in ensembles named clusters, which are inserted in the load bearing structure. Slits in the back allow to connect the cluster readout electronics to the backplanes. The design of such modular structure guarantee an easy access to individual modules in case any repair is necessary, allowing to disconnect and extract one module while the rest of the camera is still functioning. The load bearing structure is mounted inside a tubular structure which holds the camera external walls, doors and interfaces with the camera frame. In the front part of the camera there is the front window which can be totally covered by a shutter to avoid the entrance of sunlight during the

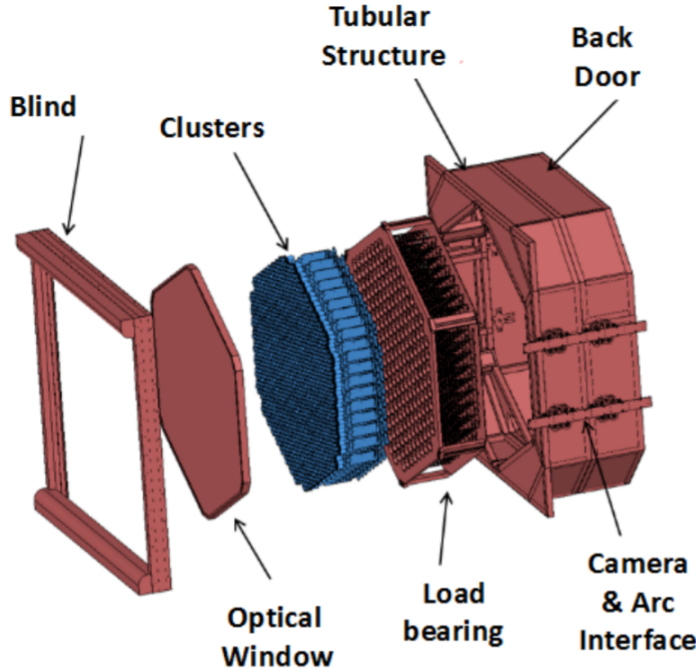


Figure 3.7: Different LST camera mechanical elements from [160].

day which could damage PMTs. In the back part of the camera lies all the cabling and auxiliary electronics. The total dimensions of the camera is  $2.9 \times 2.9 \times 1 \text{ m}^3$  and the weight is less than 2000 kg. Since all the electronics are stored inside the camera, the structure was required to accomplish a series of requirements related to the exposure to environmental conditions such as the protection to the entrance of dust, water and sunlight and guarantee a stable temperature between  $20^\circ\text{C}$  to  $40^\circ\text{C}$  [160]. Temperature regulation is possible thanks to the cooling system, consisting on a water cooling system based on cold plates and a temperature controlled air flow cooling system.

An access tower allow to manipulate the camera during day-time operations when the telescope rests in park position, and also acts as an anchor in case of strong winds.

### 3.3.2 Medium Size Telescope (MST)

MSTs will cover the core energy range of CTA, from 100 GeV to  $\sim 10\text{TeV}$ . This is the range reached by current IACTs so the improvements in sensitivity will come from the large area covered and the better image reconstruction due to the larger number of telescopes (15 in the north, 25 in the south). Currently two approaches to the MST design are being developed. The first is a 12 m diameter modified Davies-Cotton (DC) optical layout very similar to that of Very Energetic Radiation Imaging Telescope Array System (VERITAS) and High Energy Stereoscopic System (H.E.S.S.). The first prototype of this type, the Davies-Cotton MST (DC-MST) [161],

has been built in Adlershof, Germany, and is currently in commissioning phase. There are also two different camera designs for DC-MST: *FlashCam* and *NectarCAM*, which characteristics will be discussed in this section. The telescope second design uses a novel technique never built before CTA, with a 10 m diameter Schwarzschild-Couder (SC) [161] optics counting of two mirrors, and a novel Silicon Photomultiplier (SiPM) camera. The prototype for this telescope has been built in the Fred Lawrence Whipple Observatory, in Arizona. A detailed report of the status of the MSTs as of July 2019 can be found in [162]. A summary on the different parts of the telescopes is given in this section.

### **MST Structure**

The structure of both telescope designs is similar, with specific modifications for the optical system of the Schwarzschild-Couder MST (SC-MST) [161] as can be seen in figure 3.8. The main mechanical structure of the telescope is a cylindrical tower of 1.8 m diameter and 20 mm wall thickness. The tower is connected on top to the head of the telescope, that contains the azimuth bearing which allows the telescope to rotate in the horizontal axis, and the drive assemblies. It is possible to access to the tower through a door at the base. In the inside, all electrical cabinets are stored distributed over three floors. A combination of ventilation and air conditioning system is used to keep the temperature within operation range. The drive assemblies are designed to reach any object above 30° in elevation in less than 90s. It is divided in the azimuth drive subassembly and two elevation drive subassemblies, mounted in the left and right of the telescope. To account for the possible sources of excitation, like wind gusts or structure flexibility, which can lead to oscillations of the structure, an active vibration damping control is used to reduce their effect on the pointing accuracy of the telescope. The dish structure is designed to host the mirrors and attached to it is the camera support structure [163]. For the SC-MST, the positioner is the same, but the optical support is very different to sustain the segmented aspheric primary and secondary mirrors, and the camera support structure, located in the focus of the secondary [164].

### **MST Optics**

The optical system of the DC-MST consist on a mirror segmented in 86 hexagonal mirrors of 1.2m length, providing an effective mirror area  $> 88 \text{ m}^2$  and a 12 m diameter reflector. The focal length of the telescope is 16 m. Different mirror technologies are being tested, all based in cold slumping technique, with different layers of materials, coatings and structures. A system of actuators form the Active Mirror Control (AMC) system of the MST allowing to adjust the mirror position for focusing. The structure is stiff enough that is not necessary to readjust during observations to maintain the Point Spread Function (PSF). The AMC is used only for the initial mirror adjustment and for maintenance activities, or adjust the focal distance for specific observations.

The SC-MST uses a novel aplanatic optical system composed of two aspheric mirrors. This configuration is derived from the exact Schwarzschild solution with



Figure 3.8: *Left:* DC-MST prototype with FlashCam in Adlershof. *Right:* SC-MST prototype in the Fred Lawrence Whipple Observatory, from [164].

aplanatic constants  $q = 2/3$  and  $\alpha = 2/3$ . The effective focal length of this system is 5.586 m, with a collection area of 50 m<sup>2</sup>. Both mirrors are segmented, as shown in picture 3.9, and the surface is parabolic to minimize astigmatic aberrations at the edge of the field of view (FoV).

### MST Cameras

For the SC-MST two camera prototypes have been designed and tested in the structure installed in Adlershof and showers have been detected, as shown in picture 3.10. The first design named FlashCam have 1764 PMT-based pixels divided in 147 modules of 12 pixels each. It implements a fully-digital trigger and readout system which allows to define flexible trigger patterns relying on the digitized PMT signals. The readout system is designed for a dead-time-free operation with trigger rates up to 30 kHz. FlashCam uses only one gain channel, reducing the required bandwidth for data transfer. The second camera design named NectarCAM accounts for 1855 pixels, divided in 256 groups of 7 modules. The camera mechanics and many auxiliary systems have been designed to be equivalent to the LST camera. The signal digitizing of NecatrCAM relies on a dedicated Nectar ASIC which digitizes the PMT signals at sampling speeds of around 1 GHz. It implements a digital trigger based on the binary outputs of individual pixels after comparing their analog signals with a threshold (Level 0 trigger).

The camera of the SC-MST is based on SiPM pixels which allow a very fine pixelization, with 11328 pixels of angular size 0.07°, grouped in 177 modules of 8 × 8 pixels. They are arranged in a slightly parabolic shape and are operated at a temperature that must be controlled to better than 0.1° C. The focal plane of the camera has a diameter of 0.8° m and a FoV of 8°. The trigger system is based on a two level trigger, where the first level sums the analog signal from 4 adjacent pixels and apply a discriminator

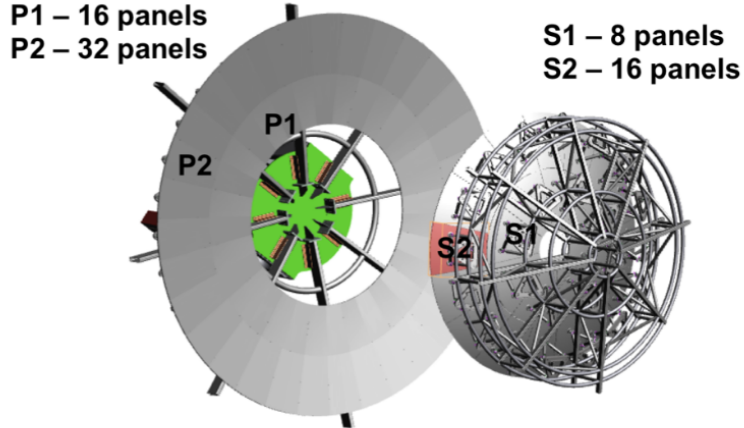


Figure 3.9: Diagram of the optical system of the SC-MST, from [161].

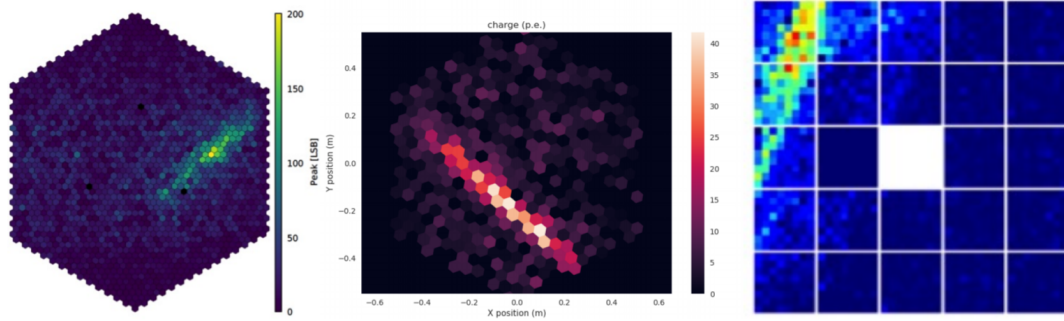


Figure 3.10: Left: DC-MST Showers obtained with FlashCam(*left*), Nectar-CAM(*middle*) and SC-MST camera (*right*) prototypes, from [162].

threshold. The camera is divided in 9 sectors of up to 25 modules and a single backplane board, which receives the trigger signal from 16 modules. A prototype of the SC-MST camera with 24 modules and 2 types of SiPM has been tested in the SC-MST prototype. The fine pixelization and the module structure of the camera can be appreciated in figure 3.10.

### 3.3.3 Small Size Telescope (SST)

The smaller telescopes, SSTs, will be the more numerous in the CTA layout, with more than 70 telescopes in the southern site. These telescopes are dedicated to detect the unfrequent highest energy  $\gamma$ -rays which in the majority of cases will come from the galactic plane. They need to be spread over a very large area, to catch as many  $\gamma$ -ray showers as possible, but they do not need large mirrors, because VHE radiation

produces a huge amount of Cherenkov light. The best sensitivity will be achieved at energies greater than 10 TeV. Three SST designs have been produced for CTA, the ASTRI telescope [165], the GCT telescope [166] and the SST-1M telescope [167]. In the end, the design of ASTRI telescopes was selected as the one that will be installed in the CTA layout, but using the GTC CHEC cameras [168]. In this section, summary descriptions of the ASTRI structure and optics design and CHEC cameras are given.

### SST-ASTRI Structure

The optical design of ASTRI telescope is based on a SC double mirror configuration, similar to the one described in section 3.3.2 for the SC-MST. A column raises from the base of the telescope and interfaces at the top with the azimuth fork. The fork sustains the elevation assembly, which is composed by the mirror dish, the counterweight and the structure that sustains the two mirrors. The dish is designed to hold the segments of the primary mirrors, which can be individually controlled by actuators. A quadrupod is attached to the dish, which together with a central pole, are joint to the structure that supports the secondary mirror and also serves to counteract deformations due to gravity and wind. The structure for the monolithic secondary mirror accounts for three actuators and three lateral arms which support the transverse components of the mirror's weight. The drive of the azimuth is located at the base of the column. An scheme of the ASTRI structure can be found in picture 3.11. A detailed description of the ASTRI structure design can be found in [169].

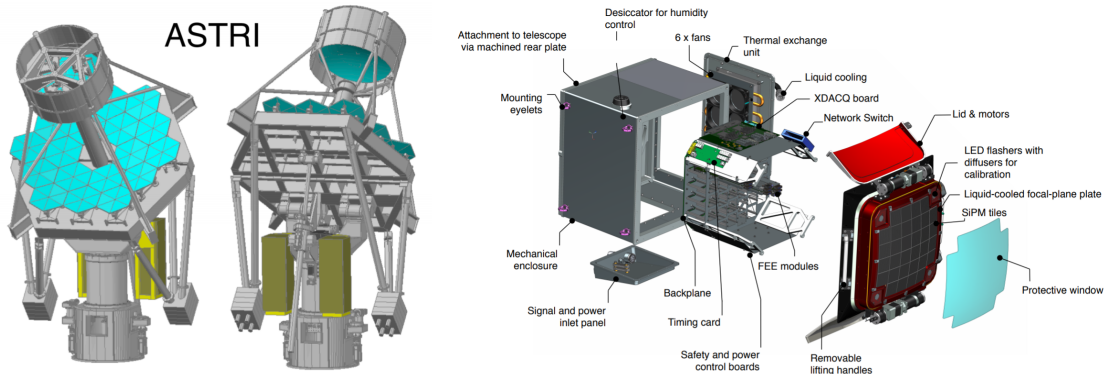


Figure 3.11: *Left:* General view of the ASTRI telescope structure and electromechanical subsystems, adapted from [169]. *Right:* CAD model of the Compact High-Energy Camera (CHEC) camera from [168]

### SST-ASTRI Optics

The SC design of the ASTRI telescopes is composed by two mirrors, one primary of 4.3 m diameter segmented in hexagonal tiles, and a monolithic secondary mirror of 1.8 m. The primary mirror tiles have been manufactured using a cold slumping replication process. The secondary is made of a hemispherical thick glass shell thermally bent to 2.2 m radius of curvature. The focal length of the system is 2.15 m, f/0.5 and the

FoV reaches 10°.

The advantages of a double mirror configuration are a better PSF over a large FoV and better correction of aberrations [165].

### **SST-CHEC Camera**

The CHEC camera was originally designed for the GTC telescope prototype, but finally has been selected to be mounted in the ASTRI structure. The camera is composed by 2048 pixels made of SiPM, instrumented in 32 photosensors which comprise 64 pixels of  $\sim 6 \times 6 \text{ mm}^2$ . The digitalization of the waveform is performed by Front-end electronics (FEE) based on TARGET ASICs [170] which also give the first trigger level, as the sum of four neighbouring pixels. A backplane provides the power, clock, trigger and data interface of the FEE. The trigger decision is formed in the backplane by combining trigger signals from all the FEE modules. In the camera structure, a lid protects the camera from the elements and a cooling system based on the circulation of chilled liquid through the camera focal plane plate and six internal fans, maintains a stable temperature. A diagram of the CHEC camera is shown in figure 3.11. A detailed description of CHEC and results from its commissioning phase can be found in [168].

## **3.4 Reconstruction and Analysis tools**

The best performance results from CTA will come not only from the telescopes designs, but it is also very important to have strong software tools, accessible and user friendly, which will allow to analyze the forthcoming data. Also, specially in the first parts of the experiment, to calculate the predicted sensitivity shown in section 3.2 it is necessary to produce precise and reliable simulations of the instrument response to the arrival of electromagnetic showers. In this section, the principal software tools for the simulation and analysis of the different levels of CTA data are described.

### **3.4.1 Monte Carlo simulations**

Monte Carlo (MC) simulations are of great importance for the IACT technique, where the detection of  $\gamma$ -rays is indirect and it is necessary to reconstruct the primary parameters from the signal received at the telescopes. Detailed simulations of the development of the Extensive Air Showers (EAS) in the atmosphere, combined with simulations of the instrument response to the Cherenkov light produced by those EAS are used for two main purposes: Separation of  $\gamma$  and hadron showers. Since hadrons produce the majority of Cherenkov light which reach IACTs, it is necessary to characterize the particular differences between photon and hadron induced showers thanks to the MC simulations; and reconstruction of the shower direction and energy of the primary. Comparing the shower parameters to those of the simulated showers, and applying different reconstruction methods, like Multi-variate analysis (MVA), Machine Learning (ML) or Deep Learning (DL) among others, the characteristics of the primary particles can be reconstructed.

MC simulations consist in two phases: The first is the simulation of the EAS development in the atmosphere, tracking the particles created, the products of their interaction and the amount of Cherenkov light produced. The second part consist on simulating the instruments, taking into account ray tracing, the optical features of the mirrors, the response of the electronics, etc.

For CTA, MC simulations have been performed using the programs **C**Osmic **R**ay **S**Imulations for **K**Ascade (CORSIKA), for the EAS simulation, and **sim\_telarray**, for the telescopes response. These two softwares allow to configure a specific array of telescopes with their particular features and store only the information of the particles and light from the showers that fall in the surrounding of the telescopes. The current production of MC data, with the layout described in section 3.2, is the named *prod3b-v2* which used CORSIKA version 6.9. In the next subsections, a brief description of CORSIKA and **sim\_telarray** is given.

### **CORSIKA**

CORSIKA is a detailed MC program to study the development of EAS in the atmosphere [171], originally developed for the Kascade experiment [172]. The showers can be initiated by different kinds of primary particles, such as photons, protons or other heavier nuclei. The program tries to treat every possible process taking place in the development of EAS to the present state of our knowledge. It takes into account the transport of particles through the atmosphere and their interactions with air particles. The secondary particles produced are tracked along their trajectories and their parameters are stored when they reach an observation level, i.e. the stage of the shower that can be detected by an instrument. The main problem of the simulation of EAS is the extrapolation of hadronic interactions at the higher energies which cannot be probed in collision experiments. The secondary particles emitted in the extreme forward direction, which are not accessible by colliders, are precisely the more important in EAS development because they are the one bringing the largest energy fraction to the atmosphere. The extrapolations must therefore rely on different theoretical models. To study the systematics of such models, in CORSIKA there are five different hadronic interaction models available. For CTA prod3b-v2 the model used was QGSJET-II [173]. An example of three different showers simulated with CORSIKA is shown in picture 3.12.

### **sim\_telarray**

The second part of MC simulations is carried out by the program **sim\_telarray** [175], dedicated to the simulations of the detectors: Optical ray-tracing of photons, their registration by PMTs, the behaviour of discriminators or comparators for trigger at pixel and telescope levels, and the digitalization of resulting signals. It was originally created for the High Energy Gamma Ray Astronomy (HEGRA) IACT system, and has been improven and made fully configurable to be used with any kind of IACT layouts.

The simulation of ray-tracing follows the trajectory of photons since they reach the

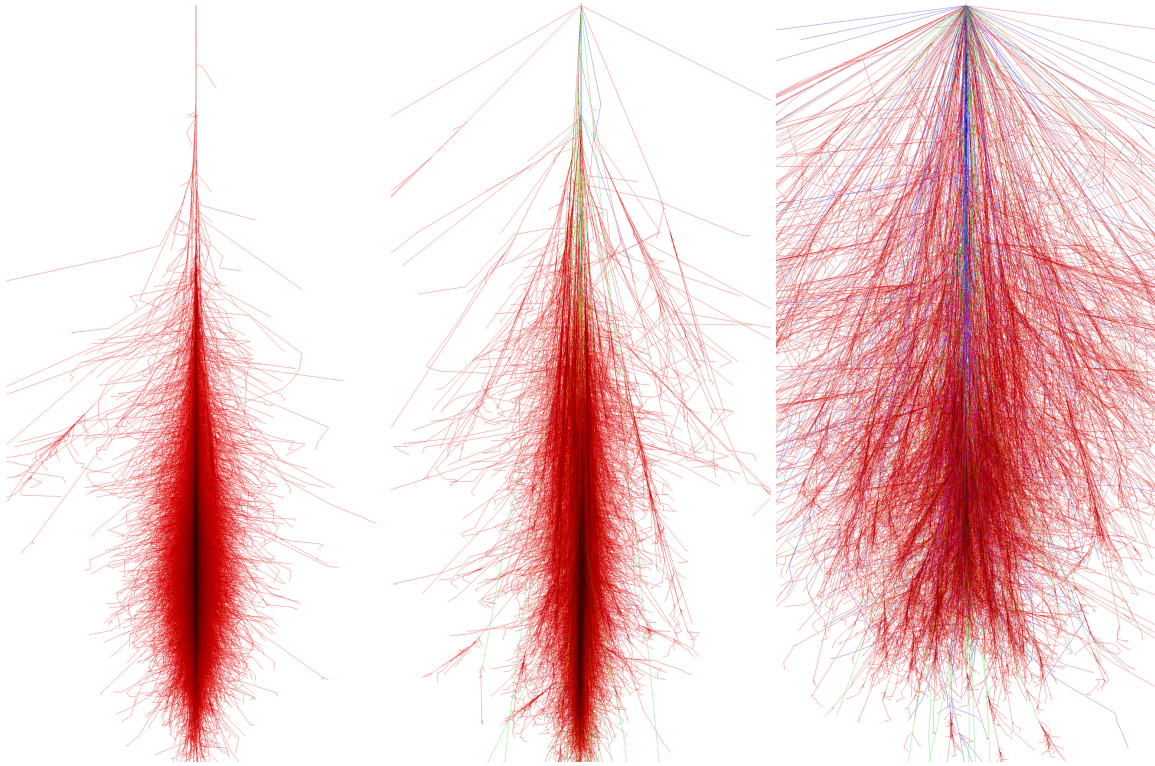


Figure 3.12: Photon (left), proton (center) and iron (right) produced showers for a primary energy of 1 TeV and  $0^\circ$  zenith angle, simulated with CORSIKA from [174].

mirrors of the telescopes and arrive to the camera pixels. The mirror optics are simulated taking into account the configured mirror morphologies, dish shapes and segmentation. The shadowing of the camera structure can be also included in the simulation. The final step of ray-tracing simulation is the angular acceptance of the pixels, which usually are equipped with Winston cones (lightguides) to avoid gaps between neighbouring pixels. From ray-tracing simulations, the PSF of the telescopes can be calculated and hence can be used to optimize their designs. In the simulation of the photon detection by the PMTs, the fluctuations in quantum efficiency in each pixel are taken into account. As pixels are permanently exposed to Night Sky Background (NSB), the number of photons arriving to each pixel is fully configurable assuming a specific NSB spectrum. In the final simulation, the amplitude of the NSB signal is subtracted from the signal baseline. The afterpulsing producing by NSB photons is also taken into account, which is produced by ions hitting the photo-catode, and can produce pulses of large aplitude which enter in the readout window. The trigger system simulation takes into account the switching behaviour of discriminators or comparators, which can be configured to a specific logic (next-neighbour, pixel secotrs...). The result from the pixel trigger system serves as input for the telescope level trigger, which usually requires at least two telescope triggers within a short time window. The final output of the sim\_telarray simulation

Data level	Description
R0	Raw data from camera, or MC data
R1	Calibrated data
DL0	Data Volume Reduced Data
DL1	Calibrated image with Hillas parameters
DL2	Reconstructed shower parameters (Energy, direction and $\gamma$ -hadron separation)
DL3	Reduced data, sets of gamma-like events with associated Instrument Response Function needed for science analysis
DL4	High level binned data products, like spectra, skymaps or light curves.
DL5	Legacy observatory data, like survey sky maps or source catalog.

Table 3.2: The different CTA data levels, based on [176] and [177]

is a data container in a format as closest as possible as the real data format from the actual instruments, based on the *eventio* machine-independent format.

### 3.4.2 Low level analysis: *ctapipe*

The analysis of CTA data, both real and simulated, goes through different steps before turning into a format with which real science can be done. A description of the different CTA data levels is given in table 3.2.

*Ctapipe* [176] is a framework for prototyping the low-level data processing algorithms for CTA. It is written in Python and is currently in development, still suffering large and rapid changes to structure and functionality. While is not yet the final code for CTA analysis, and other alternatives are currently under development, *ctapipe* is the framework chosen for the low level data analysis carried on in this thesis and so it is the one that will be described in this section.

The goal of *ctapipe* is to reduce R0 data, that is to say, raw data directly out of telescope cameras or MC simulated data out from `sim_telarray`, to dl2 reconstructed data.

Raw data can be read with *ctapipe* thanks to specific *EventSource* classes, which depend on the type of the input file (simulated data, real data from each specific telescope, etc.). It is possible to loop over the events of the source container to perform different operations on them. The first part of the data analysis is typically the calibration of the signal, meaning the treatment of the waveform signal in each pixel. *Ctapipe* allows to perform the integration of the waveform using different types of integrators (*LocalPeakWindowSum*, *FullWaveformSum...*) to calculate the total number of counts in the pixel and transform it to number of photoelectrons. The result is a camera image, where pixels contain the light from the shower and from background. Different cleaning methods, like two-level tailcuts cleaning, can be applied to subtract the background light and get the shower image. The computing of the Hillas parameters is done calculating the moments of the photons distribution of the shower image. Other functions allow to calculate the timing parameters, being the parameters from

a linear fit of the arrival times of shower pixels versus the longitudinal axis of the hillas ellipse. All these shower parameters are stored in the DL1 format, with the possibility to lose pixel-wise information and reduce the size of data files. For the reconstruction of the primary parameters, naming the energy, direction and particle type, there are currently two different algorithms implemented: A moment-based stereo reconstruction, which combines the Hillas parameters of different triggered telescopes geometrically, to estimate the shower direction; and a template-based stereo reconstruction, which uses a fit of the full camera image to a expected image model to find the best fit shower axis, energy and depth of maximum. Other methods using machine learning and deep learning techniques are also being explored but not yet implemented in the main source code of *ctapipe*.

### 3.4.3 Science analysis: *ctools*

One of the proposed softwares for the scientific analysis of CTA data is *ctools*, based on *GammaLib* [178], a versatile toolbox for the scientific analysis of astronomical  $\gamma$ -ray data. It comprises a set of tools and python scripts with a command-line interface which allow interactive data analysis. It is possible also to create scripts and pipelines within Python using *ctools* functionalities. The data managed by *ctools* is at the level of DL3 and beyond, treating with observation events, skymaps, spectra and so on. For the analysis of observation events, *ctools* includes the possibility of doing a binned (separating the data in energy bins) or unbinned analysis, and also it can stack the data of several observations to be analyzed together. A likelihood fitting can be performed to fit data to a given emission model, retrieving the best fit parameters of spectral, spatial and time components of the model of each emission source. Besides, *ctools* allow to perform simulations of observations, using a set of precomputed IRFs, to be used as *mock data* for the calculations of prospects of the future performance of CTA. Some of the most important tools of *ctools* that has been used in this thesis are:

- *ctobssim*: This tool produces simulations of event lists using the instrument characteristics specified by a given IRF and an input model. The model is composed of the individual models of each  $\gamma$ -ray source in the target FoV. Each model has a spatial component, given by the geometry of the source (point source, disk, gaussian, spatial map...), a spectral model describing the flux per energy (it can be specific functions like power law or log parabola, or an user made spectrum where the flux per each energy is given in a file), and a time model, describing the variability of the source with time. The model also should include an instrumental background model to simulate background events, which are misclassified proton events. As input, *ctobssim* requires a pointing direction, radius of the simulation region, time interval, energy interval, an IRF and an input model. The result is an event list in fits format, which contains all the information of the observation in the header.
- *ctbin*: This tool creates a counts cube, with a certain number of energy bins,

and fills it with events from an event list. It is possible to stack events from different observations in the same counts cube. The resulting cube can be used in further steps of the analysis, like the likelihood fitting.

- *ctlike*: Performs a maximum likelihood fitting of a model to binned or unbinned data. The model parameters that should be fitted have to be marked with the attribute `free="1"`. As input, it can take event lists or a count cube, and depending on the input it will perform binned or unbinned likelihood. A joint likelihood fitting can be done for multiple observations, and the average response functions (exposure, PSF and background) can be precomputed using the tools *ctexpcube*, *ctpsfcube* and *ctbkgcube*. It is also possible to calculate the Test Statistics (TS) (which is a measure of the source significance) of a source by setting the parameter `tscalc="1"` in the model. More details on the likelihood fitting with *ctools* will be given in chapter [??].
- *ctmodel*: This tool generates 3-D model cube which provides the number of predicted number of counts for an input model as a function of spatial coordinates and energy. As an input, it will require a counts cube, an event list or an observation definition file and it will need the definition parameters of the cube, such as sky coordinates, projection, energy binning, number of pixels and pixel scale.
- *ctulimit*: Computes the upper flux limit for a specific source model. Starting from the maximum likelihood parameters, the tool will look for the flux that produces a decrease in the likelihood which corresponds to a given confidence level. By default, it is set at 95% confidence level, but it can be configured. The result is the differential flux upper limit for a specified reference energy and the integrated flux in a certain energy range.





## 4.1 Introduction

The first Large Size Telescope (LST) was inaugurated in October 2018 and since then has been in commissioning phase. Being the first Cherenkov Telescope Array (CTA) telescope installed on site (in La Palma island), and it is expected to be operating on its own until LST 2-4 are built. This mean that LST1 will need its own analysis chain in *mono* mode, which differs in several aspects from the stereo analysis included in the benchmark analysis tools of CTA (see section 3.4.2). Although single telescope observations present a big challenge, specially regarding source position reconstruction and  $\gamma$ -hadron separation, it is expected that LST1 performance, thanks to its size and camera design, will be competitive enough to offer scientific results in the time it will be operating alone.

This chapter will present a considerable amount of the work done during this thesis, which includes the development of the code for the single telescope analysis for LST1, the calculation of LST1 sensitivity based on Monte Carlo (MC) simulations, the development of a new technique for Hillas Parameters calculation without cleaning using the Expectation-Maximization algorithm and the application of the analysis chain to real LST1 data.

## 4.2 The LST1 analysis chain overview

The analysis software for the single telescope analysis of LST1 named *cta-lstchain* has been developed before the necessity of specific tools for single telescope analysis not included in *ctapipe*, the benchmark analysis tools for low level data of CTA. It is written as a python package which heavily relies on *ctapipe*, and it is structured in several modules containing functions destined to the different parts of the analysis.

The first version of *cta-lstchain* was written by the author of this thesis and many contributors have joined the project over the last two years to improve and optimize the repository to its current version, which is able to perform every analysis step both for simulated MC data and real data. The analysis chain is divided in several steps, each of which can be executed through a python script which requires certain inputs and calls for the appropriate functions. All the configuration parameters of the different elements of the analysis are given through configuration files, which can be edited by the user or else a standard configuration will be used. The input of the analysis chain are the raw data files of LST1 events, which for MC data are *sim\_telarray* files and for real data are *zfits* files with a similar internal format. The files contain the full information available per pixel, known as *waveform* and which is the digitized signal amplitude vs. time sample for every triggered event, together with MC information in the case of a simulated file (such as the true energy, source position, number of simulated events, and so on), or recorded information from the different telescope subsystems in the case of real data (such as time, pointing, trigger type...). Throughout the analysis chain, the data including the images and image parameters, is stored in containers designed in *cta-lstchain* specifically for LST1, which can be dumped into *pandas* dataframes and saved in *hdf5* files.

The main steps of the analysis chain can be summarized as:

- **Calibration:** The waveforms of each pixel in the camera should be integrated after pedestal subtraction, and converted to number of photoelectrons. Also, the timing information of the signal is obtained.
- **Image cleaning and parameterization:** The images in the camera contain pixels with light not related to the cherenkov event, so a cleaning must be applied to remove them. Afterwards, the photon distribution in the image is used to calculate the Hillas parameters.
- **Energy and direction reconstruction:** The energy and direction reconstruction of the triggered events are performed using a multidimensional regression technique based on Random Forests (RFs). A set of simulated diffuse  $\gamma$  events are used to train the RF.
- **$\gamma$ -hadron separation:** For the  $\gamma$ -hadron separation, a multidimensional RF classifier is used. Sets of simulated *gamma* and proton events, which energies and directions have been reconstructed in the previous step, are used to train the classifier.

#### 4.2.1 Calibration

In the calibration phase, the raw signal known as *waveform* is integrated after background subtraction, to obtain a total number of counts per pixel, which afterwards is multiplied by a factor to be converted in number of photoelectrons. Depending on if MC data or real data is being analyzed, the following steps vary and will be explained for each case.

### Signal extraction

For every triggered event, the signal in each pixel is recorded in a 40 samples window from the 4096 samples Domino Ring Sampler version 4 (DSR4). This signal contains information not only from the Cherenkov light, but also from background light from Night Sky Background (NSB) and from the intrinsic noise induced by the readout chain. Before integrating the signal, it is necessary to subtract this *pedestal*. For simulated MC events the pedestal value for each pixel in the camera is already stored, but for real data it is necessary to take special pedestal runs, with randomly activated trigger. Pedestal events are used to calculate the mean pedestal value for each DSR4 sample so typically, around 1000 events are needed to fill the ring. In *cta-lstchain* a specific script is used to extract the pedestal values from pedestal runs and they are stored in a *hdf5* file to be used later in the calibration.

Once the pedestal is subtracted from the signal, the signal peak can be integrated. Typically a smaller window of a few samples around the maximum is used for the integration, which can be performed with one of the several integrators implemented in *ctapipe*. By default, the integrator used in *cta-lstchain* is the *NeighborPeakWindowSum*, which sums the signal in a window around the peak defined by the waveform in neighbouring pixels. This allow to avoid integrating peaks which can arise from fluctuations. The default width of the integration window for this integrator is of 7 samples. When analyzing real data, the first and last two samples of the waveform should be dropped, to avoid integrating the spikes that can arise from ?? *i.e.* These calibration steps are performed for the two gain channels of LST1 camera, if available. By default, the signal used is the high gain, unless it is saturated, meaning the maximum is above 4096 counts. In this case, the channel is switched to low gain for that pixel.

### Conversion to photoelectrons

Once the signal amplitude is extracted, it must be converted from DC counts to photoelectrons through a calibration factor, which is different for each pixel and channel. For simulated MC data, these factors are stored in the simulated file and the conversion can be done simply by multiplying the image in DC counts by the factor of each pixel. For real data, special calibration runs must be taken to calculate these factors. Calibration events are taken using Ultraviolet light pulses fired from the CaliBox [179], [180] located in the mirror dish. The calculation of the calibration coefficients is made using the F-factor method [181], which assumes that the distribution of photoelectrons in a Photomultiplier Tube (PMT) follows a poissonian statistics with a mean  $N$  and a root mean square (RMS) of  $\sqrt{N}$ . The signal distribution, however, will be deviated from a poissonian statistics with a wider RMS due to a excess-noise factor F, which is different for each PMT and whould be measured in the laboratory. The relation between the relative widths of the two

distributions can be written as:

$$F \cdot \frac{1}{\sqrt{N}} = \frac{\sigma_Q}{\langle Q \rangle} \quad (4.1)$$

Where  $\langle Q \rangle$  is the mean value of the pixel signal and  $\sigma_Q$  its RMS. The calibration coefficients will come from the relation between the number of photoelectrons  $N$  and the mean pixel signal  $\langle Q \rangle$ , which from 4.1, and taking into account that the signal must be corrected from pedestal:

$$\frac{N}{\langle Q \rangle} = F^2 \frac{\langle Q \rangle - \langle ped \rangle}{\sigma_Q^2 - \sigma_{ped}^2} \quad (4.2)$$

The values of  $\langle Q \rangle$ ,  $\sigma_Q$ ,  $\langle ped \rangle$  and  $\sigma_{ped}$  are calculated from a sufficiently large number ( $\sim 1000$ ) of calibration and pedestal events, using a specific script from *cta-lstchain*, which stores the resulting calibration coefficients in an HDF5 file to be used later in the calibration of data runs. For the LST1, the value of F factor used is the mean value for all PMT which is 1.2.

#### 4.2.2 Image cleaning and parameterization

In order to extract information from the image of Cherenkov light shower recorded by the camera, it is necessary to get rid of the background light not belonging to the Cherenkov event, which has arrived to all pixels. This background light is usually related to fluctuations in the NSB. A process named cleaning is used to eliminate all pixels which presumably do not contain light from the shower and after the *clean* image is the one used to perform the parameterization. Besides there exist several proposed cleaning algorithms in the literature [182], [183], [184], [185], for the time being in *cta-lstchain*, a classical two-level tailcuts cleaning is being used (e.g. the used in [186]). This method uses only the information of the amount of light in pixels (already converted to number of photoelectrons) and compares it to two levels of thresholds in the following way:

- Pixels with a number of photoelectrons over the highest threshold level are selected.
- If pixels selected in the previous step have at least one neighbor also above the highest level threshold, those pixels are marked as core pixels from the shower.
- Neighbors of the core pixels with number of photoelectrons above the lower level threshold are selected as boundary pixels. For the rest of them not selected, their charge is set to zero.

The standard values for the two levels used in *cta-lstchain* are  $Th_{high} = 10$  phe and  $Th_{low} = 5$  phe, just the same values used by MAGIC telescopes. Note that these values have not been yet optimized for the particular case of the LST1, and they can be changed easily in the configuration files. An optimization of the cleaning

can lead to a better performance, specially for lower energies, because in those cases Cherenkov showers are small and a lot of information can be lost because of cleaning. Using other information apart from the number of photoelectrons, for example the arrival times of the signals to pixels, can help to improve the image parameterization. Low energy showers of  $\gamma$ s and hadrons are much more difficult to differentiate, for that reason, an image parameterization which highly depends on the settings of the cleaning parameters can be problematic when trying to lower the energy threshold of the telescope. In section 4.4 a method for image parameterization not requiring previous cleaning is proposed as an alternative.

The parameterization of the shower image after cleaning, that is to say the calculation of the Hillas parameters (see section 2.4.2 and figure 2.9), is performed by a specific function from *ctapipe*. The resulting parameters: intensity (total number of photoelectrons in the shower) width, length, coordinates of ellipse center of gravity, azimuthal angle  $\phi$ , the orientation angle  $\psi$ , and the third order moments, *skewness*, which is a measure of the asymmetry of the distribution and *kurtosis*, which is a measure of whether the distribution is peaked or flat relative to a normal distribution. The calculation of the Hillas parameters with *ctapipe* only requires the image of the shower (i.e. the number of photoelectrons in each pixel) and the information of the camera geometry.

Besides the Hillas parameters, the time parameters are also calculated with other function in *ctapipe*. This function requires the shower image and a camera geometry, plus the time position of the peak in the waveform of each pixel, which is obtained with the signal integrators mentioned in section 4.2.1. The function performs a linear fit of the time positions versus the distance of the pixel from the vertical camera coordinate along the semimajor axis of the hillas ellipse. The *time gradient* is the slope of this line, and the *intercept* is the free parameter of the linear fit. These two parameters are specially important for single telescope analysis, because they reflect the direction of development of the shower, which give information of the side of the ellipse where the source position is located in the camera frame.

Ultimately, there are two extra parameters calculated: The *leakage2*, which indicates the percentage of the shower that falls in the two outer pixel rings of the camera; and the *number of islands*, which accounts for the number of separated groups of pixels (a typical  $\gamma$ -ray shower will only have one island with elliptical form, but hadronic and heavier nuclei showers tend to produce messy light distributions with several islands of irregular shapes). Both parameters are calculated with respective functions from *ctapipe*.

The calibration and image parameterization is performed *cta-lstchain* using the scripts *lstchain\_data\_r0\_to\_dl1.py*, *lstchain\_mc\_r0\_to\_dl1.py*, depending on if the raw data used is simulated or real data. As is reflected in the script names, this steps reduces the data level from raw R0 data to DL1 (see table 3.2). In general, the image parameters can well describe the shower and therefore pixel wise information is not needed in further steps of the analysis. However, for testing and crosscheck purposes, *cta-lstchain* scripts offer the possibility to store DL1 data with the full

images, or only the parameters to save disk space.

### 4.2.3 Reconstruction of energy and source position

After the calibration and image parameterization, the image parameters should be used to extract information of the primary particle, whereas is a  $\gamma$ -ray or a background event (protons, electrons, heavier nuclei...). In *cta-lstchain* the first step is to reconstruct the energy and arrival direction of the event. It can be easily seen that the energy is going to be directly proportional to the amount of Cherenkov light in the shower, hence the *intensity* parameter will be the key of energy reconstruction.

The direction reconstruction is problematic in mono mode, because even knowing that the Hillas ellipse should point towards the source position in the camera frame, we do not know which side of the ellipse is correct (this is known as head-tail degeneracy). In stereo mode, this is solved because the source position will be in the cross point between the line which follows the semimajor axis of Hillas ellipses of all cameras, but for single telescope we must rely in other methods. In the case of *cta-lstchain* we make use of a vector known as *disp*. This is the vector going from the center of gravity of the ellipse to the source position.

Originally, the disp quantity could be parametrized in terms of the elongation of the image, meaning the ratio between *width* and *length*. The first parameterization was proposed by the Whipple collaboration [187]:

$$Disp = \xi \cdot \left(1 - \frac{width}{length}\right) \quad (4.3)$$

Where  $\xi$  is a factor dependent on the amount of photoelectrons in the shower image (the *intensity* parameter) And a more general parameterization was used for MAGIC-I [188]:

$$Disp = A(intensity) + B(intensity) \cdot \frac{width}{length + \rho(intensity) \cdot leakage} \quad (4.4)$$

Where A and B and  $\rho$  are the second order polynomial function of  $\log(intensity)$ .

Instead of using a parameterization, we reconstruct the disp vector using the image parameters. The time parameters will be very important to reconstruct this quantity, because the Cherenkov light from the upper parts of the shower arrive before the light from later developed lower parts, giving the time gradient. The time gradient will therefore give information on which side of the ellipse is pointing to the source position.

The method used in *cta-lstchain* for the reconstruction of these quantities, energy and disp vector, is based on a multidimensional regression technique relying on RFs. RF is a supervised learning algorithm which uses an ensemble of several decision trees (a *bagging* technique). Decision trees are flow-chart-like structures where each internal

node denotes a test on a selected feature. The result is a split in the dataset depending on the value of that feature. The best splitting criterion for regression is typically calculated using the mean squared error (MSE). For each node, the MSE of the two subsets is calculated for each feature and for each possible cut on that feature, until a minimum is reached. This step is repeated at each node until a condition is reached, typically that the MSE of the remaining data sample is below a threshold, or it has too few events to keep splitting. The termination nodes are also known as *leaves*. In the RF, a number of decision trees are trained using a randomly selected subset of the train data ('bootstrapping') and the prediction of all the trees is averaged to reach the final result. Also, the features are always randomly permuted at each split. These two sources of randomness in the RF prevent the typical problem of overfitting from too complicated decision trees.

In the basic analysis of *cta-lstchain*, and the one carried on in this thesis, we use a source independent approach where we do not assume what is the true position of the source (which presumably will be close to the center of the camera, where the telescope is pointing). For that reason, the RFs for energy and disp reconstruction are trained using a set of MC simulated  $\gamma$  events triggering the LST1, with diffuse arrival directions distributed in a  $5^\circ$  radius field of view (FoV). The set of simulated data is divided in two sets, one for training and other for testing. The features used for the splitting of the tree nodes are  $\log_{10}(\text{intensity})$ , *width*, *length*, *x*, *y*, *psi*, *phi*, *width/length*, *skewness*, *kurtosis*, *r*, *time gradient*, *intercept*, *leakage* and *number of islands*, where *x*, *y* and *r* are the coordinates and module of the vector from center of gravity of the Hillas ellipse to the center of the camera. The trained RF is used later to reconstruct the desired values (energy and disp) in the test data. For energy reconstruction, we actually reconstruct the  $\log_{10}(E)$ . In the case of the disp vector, we reconstruct the two components of the vector (*disp\_dx*, *disp\_dy*) using the same RF.

For the implementation of the RFs, we use the Python package *scikit-learn* [189], a machine learning package which offers a large amount of tools for predictive data analysis. The class *RandomForestRegressor* allow an easy training of the RFs, which can be saved to be used later to fit any set of test data with the same format as the training. This class has a set of parameters that can be modified by the user to optimize the performance of the predictions. In *cta-lstchain* these parameters can be modified by a configuration file. The most relevant parameters and their default values in *cta-lstchain* are shown in table 4.1.

#### 4.2.4 $\gamma$ -hadron separation

The majority of Cherenkov showers produced in the atmosphere are actually not produced by  $\gamma$ -rays, but by cosmic hadrons (mainly protons). These events trigger the telescopes  $\sim 10^4$  times more than  $\gamma$ -rays, therefore it is necessary a very efficient background rejection method to discard hadronic showers and analyze only  $\gamma$  events. The methods for  $\gamma$ -hadron separation in general rely on the morphological differences between the kind of showers produced by the two kinds of primaries, and temporal

Parameter name	Value for regression	Value for classification	Description
n_estimators	150	100	Number of trees in the forest
criterion	mse	gini	Function to measure the quality of a split
max_depth	50	100	Maximum depth of the tree
min_samples_split	2	2	Minimum number of samples required to split an internal node
min_samples_leaf	2	2	Minimum number of samples to be at a leaf node
max_features	all	all	Number of features to consider when looking for the best split
random_state	42	42	Control the randomness of the bootstrapping and the sampling of features
n_jobs	4	4	Number of jobs to run in parallel

Table 4.1: Some parameters that can be configured for *RandomForestRegressor* and *RandomForestClassifier* classes, with the default values used in *cta-lstchain*.

data. This job is much more efficient in stereo mode, because  $\gamma$ -ray showers which trigger different telescopes will produce images in the cameras with a Hillas ellipse pointing towards the source position, while hadronic showers will produce much less correlated images. In mono mode we can only rely on the morphological features of the images, knowing that hadronic shower images will be much more extended, without a clear definite shape and with a higher number of islands than  $\gamma$  showers. The task of  $\gamma$ -hadron separation is done in *cta-lstchain* with a RF classifier, which follows similar principles as the RF regressor explained in the previous section. Instead of calculating the value of a variable, it decides between a given number of classes to which each events belongs. In this case, its only a two classes problem:  $\gamma$ s or hadrons. The best splitting criterion for classification is calculated in terms of the so-called gini index. The gini index or gini impurity is a measure of how often a randomly chosen event would be incorrectly classified if it was classified randomly following the distribution of classes. The formula for the Gini index  $I_G$  calculated for a set of events with  $J$  classes is:

$$I_G(p) = 1 - \sum_{i=1}^J p_i^2 \quad (4.5)$$

Where  $p_i$  is the probability of an event belonging to the class  $i$  to be correctly classified. The Gini index go from 0 to 1, where 0 means that all the events of a subset have been classified to one class, and 1 that the events of the subset are randomly distributed along all the possible classes. The splitting decision will be made minimizing the value of the Gini index.

The training set for the  $\gamma$ -hadron classifier will consist on two sets of MC simulated events, one of diffuse gammas  $\gamma$ s and one of protons, with arrival directions coming from a  $10^\circ$  FoV. Usually, the set of hadronic events used for training is taken from real background events recorded with the telescope when pointing to a direction in the sky without any  $\gamma$ -ray source, because the simulation of proton showers has a lot of uncertainties (see section 3.4.1). However, as by the time this thesis was written there were not enough real data from LST1 to build a big enough background data set, all the calculations have been made using MC simulations.

The features used for the splitting of the classifiers are the same from the ones used for the regressors of the previous section, but adding the reconstructed energies and disp vector. To do so, the original  $\gamma$  events set is splitted in a training set for the regressor, and a test set, to which the energy and disp vector are reconstructed. The regressors are also used to reconstruct the energy and disp vector of the set of proton events. Afterwards, this new set of  $\gamma$  and proton events, with reconstructed energy and disp is divided again in a training and test set to build the RF classifier. The classifier is implemented using the *RandomForestClassifier* class from *scikit-learn* which input parameters are listed in table 4.1

## 4.3 Sensitivity of the LST1

The sensitivity of a telescope is defined as the minimum flux of  $\gamma$ -rays over background that should be detected for a statistically significant detection. Using the simulated MC data and the analysis techniques explained in section 4.2 we have calculated the differential sensitivity of LST1 in mono mode.

The sensitivity is calculated for the detection of a point source after 50 hours of observations. To do so, we are using the Li&Ma method, extensively described in [190], but here I will summarize the basic concept.

We need to calculate the significance of detection of a source, meaning that we need a way to evaluate the statistical reliability of an observational result. A typical observation in  $\gamma$ -ray astronomy will consist on the pointing to a region where it is supposed to exist a source, recording  $N_{on}$  counts in a time  $t_{on}$ . Then, to evaluate the background, a region without sources will be observed, recording  $N_{off}$  counts in a time  $t_{off}$ . If the ratio between the observation time of the on and off regions is  $\alpha = t_{on}/t_{off}$  then the number of background photons in the on region will be estimated by  $\hat{N}_B = \alpha N_{off}$  and the probable number of photons contributed by the source is  $N_S = N_{on} - \alpha N_{off}$ . The significance can be estimated in terms of the likelihood ratio method, where we test the 'null hypotheses', being the hypotheses where no source exists at all and all the excess counts detected in the on region are due to fluctuations in the background, therefore  $N_{on}$  will follow a Poisson distribution with variance equal to that of the background  $\langle N_B \rangle$ . The likelihood ratio can be

written as:

$$\lambda = \frac{L(X|E_0, \hat{T}_c)}{L(X|\hat{E}, \hat{T})} \quad (4.6)$$

Where X are the observed data and  $(\hat{E}, \hat{T})$  are the maximum likelihood estimation of the unknown parameters. In the null hypotheses,  $E = E_0$  and  $T = \hat{T}_c$  are the parameters for the conditional maximum likelihood estimation. In our case, the unknown parameters will be  $N_S, N_B$  where in the null hypothesis  $N_S = 0$ .  
The maximum likelihood ratio can be derived as:

$$\lambda = \left[ \frac{\alpha}{1 + \alpha} \left( \frac{N_{on} + N_{off}}{N_{on}} \right) \right]^{N_{on}} \left[ \frac{1}{1 + \alpha} \left( \frac{N_{on} + N_{off}}{N_{off}} \right) \right]^{N_{off}} \quad (4.7)$$

If the null hypothesis is true, and  $N_{on}, N_{off} \gtrsim 10$ , by the theorem exposed in [190], the quantity  $-2\ln\lambda$  will asymptotically follow a  $\chi^2$  distribution with one degree of freedom. Therefore  $\sqrt{-2\ln\lambda}$  will be equivalent to the absolute value of a standard normal variable, so we can take it as the significance:

$$S = \sqrt{-2\ln\lambda} \quad (4.8)$$

Typically, a detection is claimed when the significance  $S$  is equal to 5 ( $5\sigma$  detection). To calculate the sensitivity of LST1 we need to know the number of excess counts from a hypothetical source  $N_S$  that will lead to  $S = 5$  for  $\alpha = 1/5$ .

To perform this calculation, we need to estimate the number of background (proton) events ( $N_B = \alpha N_{off}$ ) that will be left after analyzing the data and doing the  $\gamma$ -hadron separation. The steps followed are described in the next sections.

### 4.3.1 Reweighting

The MC simulations of Extensive Air Showers (EAS) used for this work were simulated as if the particles ( $\gamma$ s or protons) followed a power law spectrum :

$$\frac{dN}{dE} = KE^a \quad (4.9)$$

with a spectral index  $a = -2$ . However, we want to give the sensitivity with respect to the true spectrum of protons, and typically, the spectrum of the Crab nebula is used for the  $\gamma$ -rays. We need to transform the distribution of simulated events from number of events per energy to a rate of events (events per unit time) per energy which follow the desired spectral shapw. We will calculate a spectral weight  $w(E)$  for each event, which will depend on its true energy.

Suppose that  $N$  MC events have been generated in the energy range  $(E_1, E_2)$ , following

the power law from 4.9, with isotropically distributed directions in a solid angle  $\Omega$  and impact parameters uniformly distributed in a circular area  $A$ , orthogonal to the incident direction of the particles. The quantity  $K$  will be:

$$K = \frac{N(a+1)}{E_2^{a+1} - E_1^{a+1}} \quad (4.10)$$

We want to change the shape of this spectrum, and get a new differential spectrum of the shape:

$$\frac{dF}{dE(E)} = \frac{dF}{dE(E_0)} \cdot f(E/E_0) \quad (4.11)$$

Where  $\frac{dF}{dE(E_0)}$  is a normalization factor referring to an arbitrary energy  $E_0$ , which should be between  $E_1$  and  $E_2$ , with units  $s^{-1}sr^{-1}m^{-2}TeV^{-1}$  and  $f$  is a function that satisfies  $f(E = E_0) = 1$ . In our case,  $f$  will simply be the new power law. To correct the  $dN/dE$  simulated spectrum to the desired power law, we should multiply it by  $(E/E_0)^{-a}$ , so it will become flat, and then by  $f(E/E_0)$  to get the correct form. Weighting by these two factors, the corrected number of MC events  $N'$  will be the integral:

$$N' = \int_{E_1}^{E_2} \left( \frac{E}{E_0} \right)^{-a} f(E/E_0) dE = \int_{E_1}^{E_2} KE_0^a f(E/E_0) dE \quad (4.12)$$

We need to transform the number of events to a rate (in Hz), in order to calculate the sensitivity for a certain observation time. The total rate calculated in the energy range  $E_1, E_2$  will be:

$$R = \int_{E_2}^{E_1} \frac{dF}{dE} dEd\Omega dA \quad (4.13)$$

Therefore, the final weight  $w(E)$  for which the spectrum of each event should be multiplied is:

$$w(E) = \left( \frac{E}{E_0} \right)^{-a} \cdot f(E/E_0) \cdot \frac{N'}{R} \quad (4.14)$$

Where  $a = -2$  is the spectral index of the simulated events,  $E_0$  is taken as 1 TeV and  $f(E/E_0)$  would depend on the spectral shape to be reproduced. For  $\gamma$  events we take the spectrum of the Crab nebula measured by HEGRA [191]:

$$\left( \frac{dF}{dE} \right)_{Crab} = 2.83 \cdot 10^{-14} \left( \frac{E}{1TeV} \right)^{-2.62} GeV^{-1}cm^{-2}s^{-1} \quad (4.15)$$

And for protons, we use the results from the BESS spectrometer [192]:

$$\left(\frac{dF}{dE}\right)_{Crab} = 9.6 \cdot 10^{-9} \left(\frac{E}{1TeV}\right)^{-2.7} GeV^{-1}cm^{-2}s^{-1} \quad (4.16)$$

The values of the differential sensitivity will be given for a certain number of energy bins, therefore, we must calculate the number of weighted events in each energy bin and multiply them by the observation time. This will give us the quantities  $N_S$  and  $N_B$ . To calculate the sensitivity we only need  $N_B$ , which will be the number of weighted proton events divided by the factor  $\alpha = 1/5$ .

### 4.3.2 Cut optimization

To obtain the best possible sensitivity, instead of using all the weighted proton events, we can use the two parameters *gammaness* and  $\theta^2$  to perform cuts that will reject the majority of the background.

*Gammaness* is a number between 0 and 1 assigned by the RF classifier to make the decision on the  $\gamma$ -hadron separation. Events close to 1 will be more  $\gamma$ -like, and events close to 0 will be more proton-like.  $\theta^2$  is the angle between the reconstructed direction of the event and the true assumed direction of the source. Events with a high  $\theta^2$  are most likely to be proton events, while  $\gamma$ s will have a  $\theta^2$  close to 0. For protons, To optimize the cuts in these parameters, we define several bins in *gammaness* and  $\theta^2$ , calculate the number of weighted proton events left after the cuts in each bin and then use this quantity as  $N_B$  for the sensitivity calculation. For each energy bin, we will select the combination of cuts which provides the best sensitivity. We require that after the cuts, at least 10 events of  $\gamma$ s and protons should remain in the energy bin.

### 4.3.3 Expected LST1 Performance

The analysis methods described before were used to compute the expected performance of the LST1 in mono mode for the observation of a point source, being the analysis source independent (meaning no assumption on the source position is made). In this section, the results on energy and angular resolution,  $\gamma$ -hadron separation and sensitivity are discussed.

#### Data

The data used for the analysis is a set of MC simulations produced specifically for the LST1 in the northern CTA site. The primaries produced were  $\gamma$ s as a point source with an offset of  $0.4^\circ$  from the center of the camera, diffuse  $\gamma$ s, protons and electrons, but for the results given in this thesis, electrons were not included. The injection of particles were splitted in North and South, but only the South production has been used here. The zenith angle assumed was  $20^\circ$ , the spectral index of the particle spectra was -2. A summary of the main features of the production is given in table 4.2.

	$\gamma$ (PS) offset = 0.4°	$\gamma$ diffuse	electron	proton
Energy Range	5 GeV - 50 TeV	5 GeV - 50 TeV	5 GeV - 5 TeV	10 GeV - 100 TeV
Viewcone	0 °	10°	10°	15 °
Core Range	1000 m	1000	1000 m	2500
Input Events	South: $3 \cdot 10^7$ North: $3 \cdot 10^7$	South: $5 \cdot 10^8$ North: $5 \cdot 10^8$	South: $6 \cdot 10^8$ North: $6 \cdot 10^8$	South: $5 \cdot 10^9$ North: $5 \cdot 10^9$
Triggered Events	South: $1.08 \cdot 10^6$ South: $9.60 \cdot 10^5$	South: $1.22 \cdot 10^6$ South: $1.11 \cdot 10^6$	South: $1.18 \cdot 10^6$ South: $1.04 \cdot 10^6$	South: $8.25 \cdot 10^5$ South: $8.10 \cdot 10^5$

Table 4.2: Summary of the MC production dedicated to the LST1

After calibrating and parameterizing the data, using three sets of cleaning parameters to study the effect on cleaning in the analysis, the diffuse  $\gamma$  events were used to train the RF regressors. After, a subset of diffuse  $\gamma$ s and the hadron events to which the energy and direction was reconstructed, were used to train the RF classifier for  $\gamma$ -hadron separation. The point source  $\gamma$ s have been used to produce the performance results. A filter in intensity  $> 300$  phe, and leakage  $< 0.2$  was applied to the reconstructed events.

### Energy resolution

The energy resolution give information on the preciseness of the energy reconstruction. It is defined as the 68th percentile of the relative error  $\Delta E/E = E_{reco} - E_{true}/E_{true}$ . If the relative error follows a normal distribution, the 68th percentile is equivalent to one  $\sigma$ . The results on energy resolution are shown in figure 4.1

### Angular resolution

The angular resolution is calculated in a similar way as the energy resolution, but in this case the relative error shown in figure 4.2 refers to the angular difference between the true direction of the source and the reconstructed direction.

### $\gamma$ -hadron separation

The performance in  $\gamma$ -hadron separation can be studied in terms of the receiver operating characteristic (ROC) curve of the RF classifier. The ROC curve illustrated the diagnostic ability of a binary classifier as its discrimination threshold is varied. It is produced plotting the true positive rate(the rate of  $\gamma$ s correctly classified as gammas) versus the false positive rate (the rate of protons incorrectly classified as  $\gamma$ s) at several thresholds (gammaness). A value of 1 in true positive rate, while 0 in the false positive rate would mean a perfect classification. The closest of the ROC curve to a diagonal, the more similar to an uniformly random distribution is the classification. For this result, a subset of protons were used to test the RF classifier together with the point-like  $\gamma$ s. Result is shown in figure 4.3.

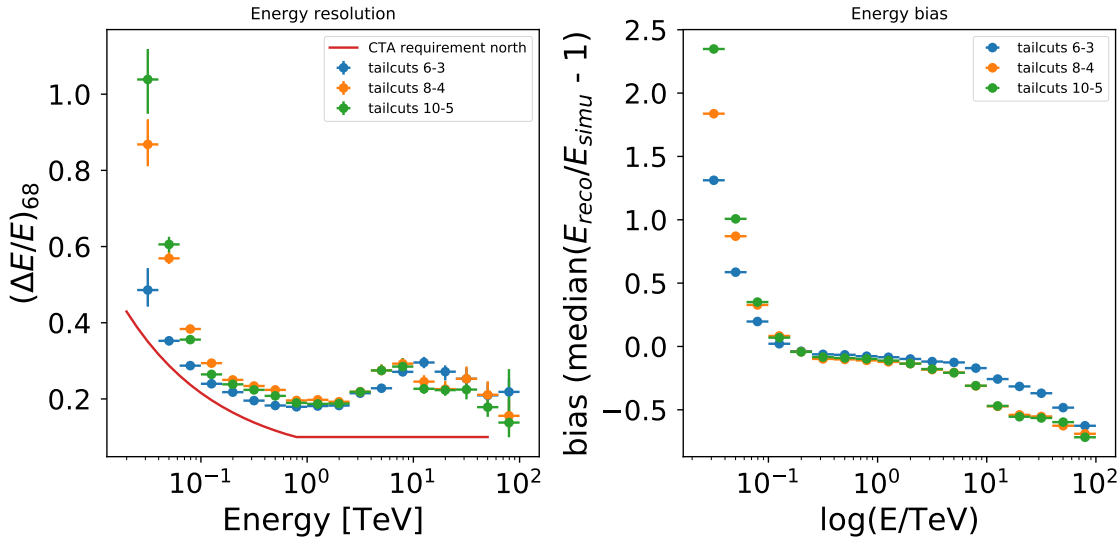


Figure 4.1: Energy resolution plots for the LST1 analysis applied to a MC production of point-like  $\gamma$  events, for three different sets of cleaning parameters (low level-high level threshold in number of photoelectrons). As a reference, the energy resolution requirement for CTA-north is also shown. The energy resolution plot of the *left* has been bias corrected.

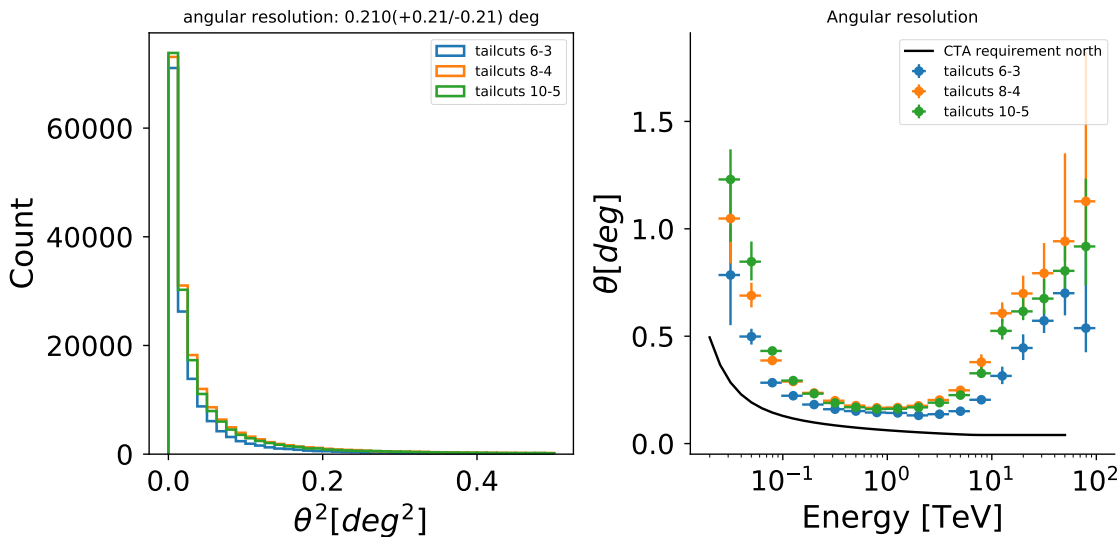


Figure 4.2: *Left:*  $\theta^2$  plot for the MC simulated  $\gamma$  point-like events, using three sets of cleaning parameters. *Right:* Angular resolution as a function of reconstructed energy.

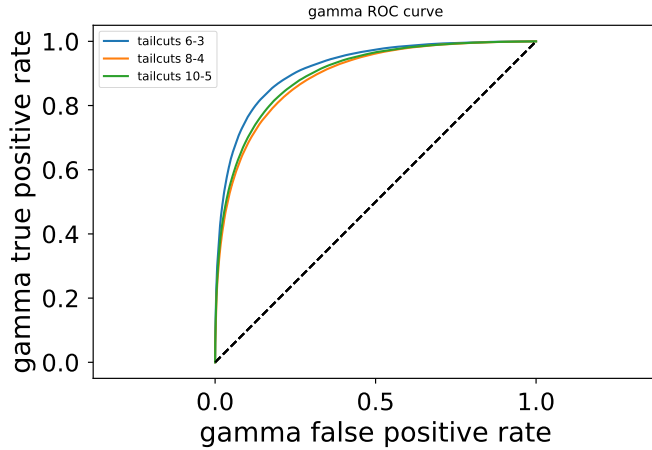


Figure 4.3: ROC curve of the RF classifier applied to point-like gamma and diffuse proton events, for three different sets of cleaning parameters.

### Effective Area

The effective area calculated for the LST1, for the detection of showers from a point source is shown in figure 4.4.

### Sensitivity

For the calculation of the sensitivity, a subset of proton events was used as background (off) events. The point-like  $\gamma$  events were used together with the protons to calculate the cuts in gammaness and  $\theta_2$  which provided the best sensitivity in each of the 20 energy bins taken. To do so, the sensitivity was calculated for 10 cuts in gammaness and in  $\theta_2$  for each energy. The combination of cuts giving the lower value in sensitivity, keeping a minimum of 10  $\gamma$  and proton events in the bin (both before and after reweighting), was selected. The resulting sensitivity curve is shown in picture 4.5.

## 4.4 Expectation-Maximization method for Hillas Parameters calculation without cleaning

As explained in section 4.2.2, cleaning methods often require the adjust of some parametrs, which have to be done 'by hand', trying to find a balance between a good enough background supression without loosing too much information from the shower. The cleaning parameters affect particularly the analysis of low energy showers. In the tailcuts method, too strong cleaning thresholds tend to eliminate too many pixels of the already small low energy showers, making the task of  $\gamma$ -hadron separation much more difficult. Also, losing the ellipse shape of  $\gamma$  showers lead to wrong calculation of Hillas parameters and consequently of the disp vector.

For all these reasons, with the aim on research for new analysis methods which could improve the performance of LST I have developed a method of image parameterization

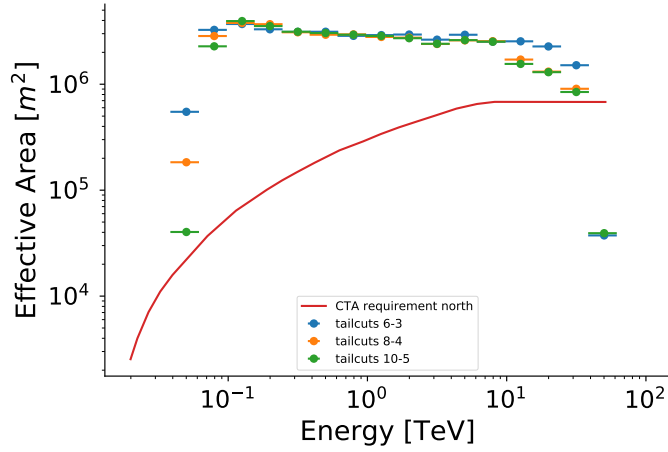


Figure 4.4: Effective area per energy bin for the MC simulated  $\gamma$  point-like events, using three sets of cleaning parameters.

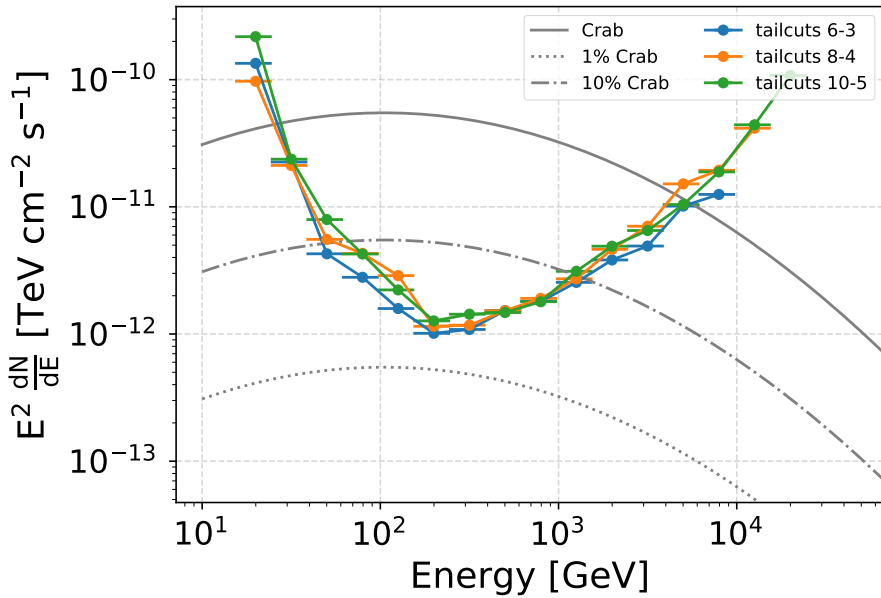


Figure 4.5: Sensitivity plot for 50h of observation of a point-like  $\gamma$ -ray source with a Crab-like spectrum, obtained by selecting the cuts in gammaness and  $\theta_2$  which provided the best differential sensitivity per energy bin. As a reference, the spectra of Crab, 10% of Crab and 1 % of Crab emission are shown.

which do not require a previous cleaning. It is based in the Expectation-Maximization (EM) algorithm, where recursively the light content in each pixel is assigned to be part of the shower or the background. In the next sections, I will briefly summarize the basic concepts of the EM method and how it can be applied to images of showers. Then I will show some results comparing the EM with the classic cleaning method.

#### 4.4.1 The Expectation-Maximization algorithm

The EM algorithm [193] is an iterative method for calculating maximum likelihood estimates of model parameters, where the model depends on unobserved data or latent variables. These latent variables would be those that cannot be observed in the data set, but still can influence other random variables. The algorithm will iterate until finding the model parameters and hidden variables that converge to a maximum likelihood estimation.

Given a statistical model which has generated a set of  $X$  observed data points, which depends on a set of latent variables  $Z$  and unknown parameters  $\theta$ , the basic iteration of the EM consist on two steps:

- **Expectation:** Creates an expectation function  $Q(\theta|\theta^{(t)})$ , which is the evaluation of the log-likelihood with the current estimate of the model parameters  $\theta^{(t)}$ , meaning it calculate the latent variables  $Z$ .

$$Q(\theta|\theta^{(t)}) = E_{Z|X,\theta^{(t)}} \quad (4.17)$$

- **Maximization:** Maximizes the log-likelihood function found in the previous step to find a new set of estimated parameters.

$$\theta^{(t+1)} = \text{argmax} Q(\theta|\theta^{(t)}) \quad (4.18)$$

A common problem that has been successfully solved by the EM algorithm is the mixture models problem, where there is a set of data which has been produced by several density distribution functions, but is impossible to know which distribution has produced each data point. This distinction between distributions would be the latent variable. This is the particular case we face with shower images. We have a distribution of light in the pixels of the camera, and we know that some photoelectrons in each pixel belong to Cherenkov light, and others belong to background light from the night sky. We want to know the fraction of light in each pixel which belongs to each of the distributions.

We assume that the Cherenkov light will follow a bidimensional gaussian distribution, which will therefore produce the elliptical shape in the image, and the background is simply a two dimensional constant distribution. The parameters of the model will be the usual gaussian parameters (mean and standard deviation in two dimensions)  $\{x_0, y_0, \sigma_{xx}, \sigma_{yy}, \sigma_{xy}\}$  and the latent variables will be the fraction of photoelectrons from the Cherenkov shower  $n_{Ch}/n$  and from the background  $n_{bkg}/n$  in each pixel with  $n$  total photoelectrons.

What we need to know is the number of photoelectrons belonging to each distribution:

$$N_i = \sum_{pixels} P(pixel/i) \cdot N \quad (4.19)$$

Where  $N_i$  is the number of photoelectrons produced by the model  $i$ ,  $N$  is the total number of photoelectrons in the image and  $P(pixel/i)$  is the probability of a photoelectron in the pixel to have been produced by the model  $i$ .

Using the Bayes theorem:

$$P(pixel/i) = \frac{P_i(pixel) \cdot P_i}{P(pixel)} \quad (4.20)$$

Where  $P_i(pixel)$  is the probability of a photoelectron from the model  $i$  to fall in the pixel,  $P_i$  is the probability of a photoelectron to be produced by the model  $i$  and  $P(pixel)$  is the probability of a photoelectron to fall in the pixel. This last probability will actually be:

$$P(pixel) = \sum_i P_i \cdot P_i(pixel) \quad (4.21)$$

Where probabilities  $P_i = (P_{Ch}, P_{Bkg})$  are equal to the fraction of photoelectrons in the image belonging to the shower(background) with respect to the total number of photoelectrons. The probabilities  $P_i(pixel)$  can be written as:

$$\begin{aligned} P_{Ch}(pixel) &= BiGaus(x_0, y_0, \sigma_{xx}, \sigma_{yy}, \sigma_{xy}) \cdot A_{pixel} \\ P_{bkg}(pixel) &= A_{pixel}/A_{total} \end{aligned} \quad (4.22)$$

Where  $A_{pixel}$  is the area of the pixel and  $A_{total}$  the sum of the areas of all pixels.

The loop in the EM to solve this problem will go as follows:

1. We make an initial assumption of the gaussian parameters. Because the bidimensional gaussian corresponds to the Hillas ellipse, the means of the distribution will coincide with the center of gravity of the ellipse, which will be close to the pixel with higher charge. To avoid committing a mistake choosing the initial value due to an outlier pixel, we take the initial means of the gaussian ( $x_0, y_0$ ) as the coordinates of the baricenter of the three more luminous pixels. The initial values of the standard deviations are set to arbitrary high values  $\sigma_{xx} = 20000$ ,  $\sigma_{yy} = 20000$ ,  $\sigma_{xy} = 0$ . Also we assume an initial estimation of the fraction of the light belonging to the shower and background as 50% of the total number of photoelectrons for each.
2. Expectation: Using the previous estimation of gaussian parameters and fractions of photoelectrons, we solve equation 4.20 and obtain the distributions of the shower and the background, that is to say, for each pixel we calculate the number of photoelectrons belonging to the shower and to the background.

3. Maximization: Using the distributions from previous steps, we calculate the parameters of the bidimensional gaussian corresponding to the Cherenkov light distribution, and the fraction of the total photoelectrons produced by each distribution (which is simply the sum of all shower and background pixels content respectively). The new gaussian parameters will be:

$$\begin{aligned}
 mean_x &= \frac{1}{N} \sum_{pixels} n_{Ch} x_{pix} \\
 mean_y &= \frac{1}{N} \sum_{pixels} n_{Ch} y_{pix} \\
 \sigma_{xx} &= \frac{1}{N} \sum_{pixels} n_{Ch} x_{pix}^2 - mean_x^2 \\
 \sigma_{yy} &= \frac{1}{N} \sum_{pixels} n_{Ch} y_{pix}^2 - mean_y^2 \\
 \sigma_{xy} &= \frac{1}{N} \sum_{pixels} n_{Ch} x_{pix}^2 y_{pix}^2 - mean_x mean_y
 \end{aligned} \tag{4.23}$$

4. Steps 2 and 3 are repeated until convergence.

The EM method was used to calculate the hillas parameters of a small subset of the MC production described in section 4.3.3 ( $\sim 20k$  events of diffuse  $\gamma$ s and protons for training the RFs, and  $\sim 200k$  events of point-like gammas for testing the results). These parameters were used to do the energy and direction reconstruction and the  $\gamma$ -hadron classification. The results, compared to the ones obtained using the tailcuts cleaning and parameterization method are shown in the next section.

#### 4.4.2 Comparison of EM without cleaning and tailcuts cleaning

In this section, results on energy resolution, angular resolution and  $\gamma$ -hadron separation using the EM method for Hillas parameters calculation without previous cleaning are presented, compared to the results obtained applying the classic method of tailcuts cleaning for three sets of cleaning parameters.

The timing parameters are not included in the features for RF training because its calculation in *ctapipe* has not been made compatible with the EM code developed here.

From figure 4.6 it can be appreciated that the results for the EM method are compatible with the tailcuts cleaning method, reassuring that this is a valid method of Hillas parameterization which allows to go through the step of cleaning which clearly can affect the performance results, as shown in section 4.3.3. The principal current caveat of the method is that it is much more time consuming than the simple tailcuts methods, but taking into account that no time optimization work has been done in the code, great improvements can be expected.

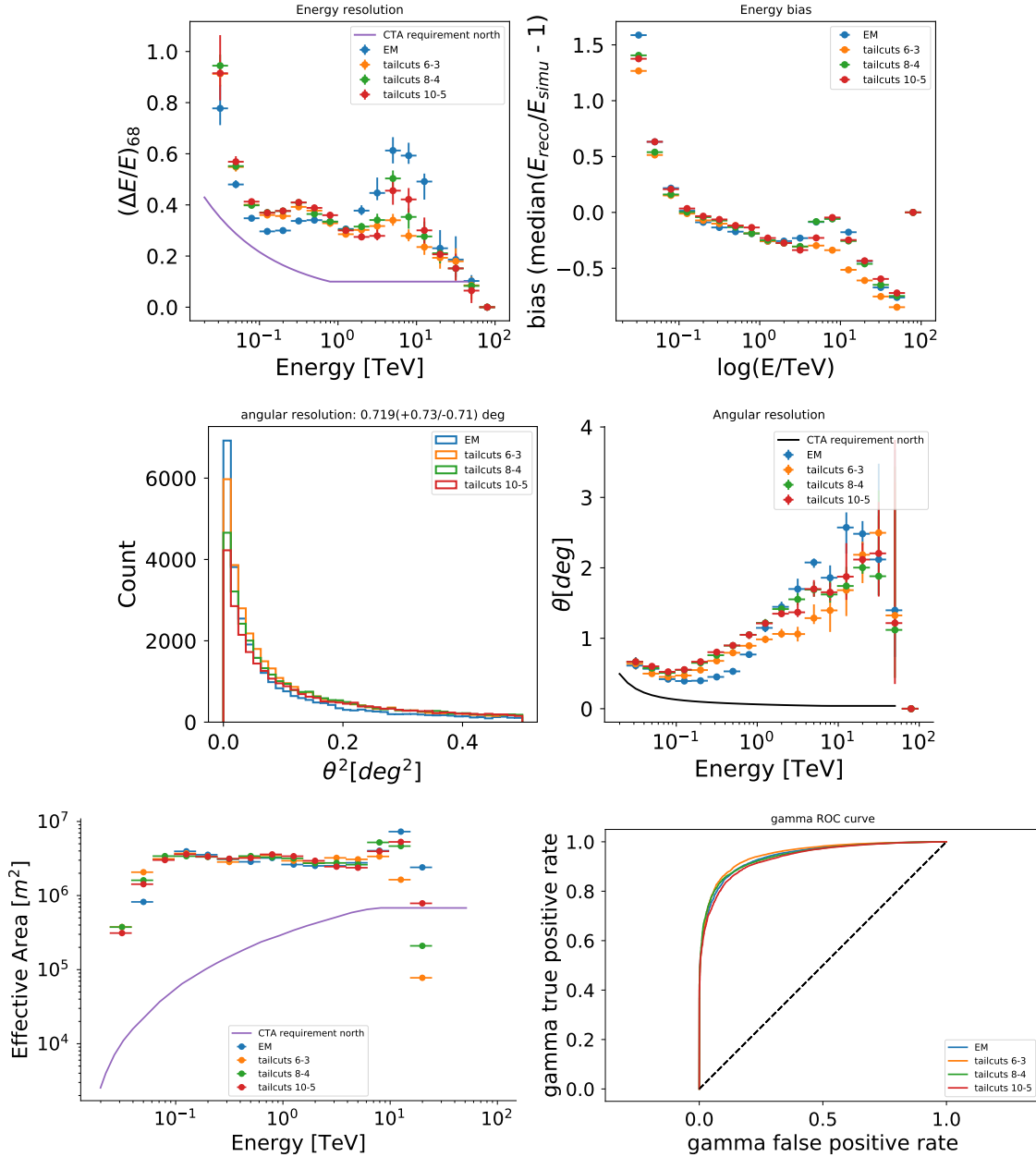


Figure 4.6: Energy resolution (*top*), angular resolution (*middle*), effective area (*bottom-left*) and ROC curve (*bottom-right*) plots for a small subset of events analyzed using the EM method for Hillas parameterization without cleaning, compared to three different subsets of tailcuts cleaning parameters.

## 4.5 Results on real data





## Bibliography

1. Berezhko, E. G. Origin of Galactic Cosmic Rays from Supernova Remnants. *Nuclear Physics B Proceedings Supplements* **256**, 23–35 (Nov. 2014).
2. Gozzini, S. R., Carmona, E., Jankowski, F., Krause, J. & and, I. R. The supernova remnant W51C: a plausible source of galactic cosmic rays? *Journal of Physics: Conference Series* **409**, 012116 (Feb. 2013).
3. Thoudam, S. & Hörandel, J. R. Nearby supernova remnants and the cosmic ray spectral hardening at high energies. *Monthly Notices of the Royal Astronomical Society* **421**, 1209–1214. ISSN: 0035-8711 (Mar. 2012).
4. Thoudam, S. *et al.* Cosmic-ray energy spectrum and composition up to the ankle: the case for a second Galactic component. **595**, A33 (Oct. 2016).
5. Bazilevskaya, G. A. Once again about origin of the solar cosmic rays. *Journal of Physics: Conference Series* **798**, 012034 (Jan. 2017).
6. Podgorny, A. I., Podgorny, I. M., Balabin, Y. V., Meshalkina, N. S. & Vashenyuk. The spectrum of solar relativistic cosmic ray measurements and numerical simulation. *Journal of Physics: Conference Series* **798**, 012027 (Jan. 2017).
7. Castellina, A. & Donato, F. in *Planets, Stars and Stellar Systems: Volume 5: Galactic Structure and Stellar Populations* (eds Oswalt, T. D. & Gilmore, G.) 725–788 (Springer Netherlands, Dordrecht, 2013). doi:10.1007/978-94-007-5612-0\_14. <[https://doi.org/10.1007/978-94-007-5612-0\\_14](https://doi.org/10.1007/978-94-007-5612-0_14)>.
8. Alves Batista, R. *et al.* Open Questions in Cosmic-Ray Research at Ultrahigh Energies. *Frontiers in Astronomy and Space Sciences* **6**, 23. ISSN: 2296-987X (2019).
9. Hanlon, W. F. *Updated cosmic ray spectrum 2015*. <<http://www.physics.utah.edu/~whanlon/spectrum.html>>.

10. Hillas, A. M. The Origin of Ultra-High-Energy Cosmic Rays. *Annual Review of Astronomy and Astrophysics* **22**, 425–444 (1984).
11. Perkins, D. H. *Particle Astrophysics* 2nd ed. (Oxford University Press, 2009).
12. Tatischeff, V. & Gabici, S. Particle Acceleration by Supernova Shocks and Spallogenic Nucleosynthesis of Light Elements. *Annual Review of Nuclear and Particle Science* **68**, 377–404 (Oct. 2018).
13. Hillas, A. M. The Origin of Ultrahigh-Energy Cosmic Rays. *Ann. Rev. Astron. Astrophys.* **22**, 425–444 (1984).
14. Petrosian, V. & Bykov, A. M. Particle Acceleration Mechanisms. **134**, 207–227 (Feb. 2008).
15. Melrose, D. B. Acceleration Mechanisms. *arXiv e-prints*, arXiv:0902.1803 (Feb. 2009).
16. Fermi, E. in, 238–252 (Dec. 1972). ISBN: 9780080167244. doi:10.1016/B978-0-08-016724-4.50024-0.
17. Longair, M. S. *High Energy Astrophysics* 3rd ed. (Cambridge University Press, 2011).
18. Lagage, P. O. & Cesarsky, C. J. The maximum energy of cosmic rays accelerated by supernova shocks. **125**, 249–257 (Sept. 1983).
19. Ramana Murthy, P. V. & Wolfendale, A. W. *Gamma-ray Astronomy* **273** (Apr. 1993).
20. Weekes, T. *Very High Energy Gamma-Ray Astronomy* ISBN: 9781420033199. <<https://books.google.com.ua/books?id=wSTOBgAAQBAJ>> (CRC Press, 2003).
21. Maoz, D. *Astrophysics in a nutshell* <<https://cds.cern.ch/record/1142636>> (Princeton Univ. Press, Princeton, NJ, 2007).
22. Oya Vallejo, I. *Observations of Active Galactic Nuclei with the MAGIC Telescope* PhD thesis (UCM, Madrid, Dept. Phys., 2010). <<https://magiccoll.mpp.mpg.de/publications/theses/I0ya.pdf>>.
23. Harwit, M. *Astrophysical Concepts. Fourth edition* <<https://www.springer.com/gp/book/9781475720198>> (Springer Science Business Media, 2006).
24. Ruderman, M. A. & Sutherland, P. G. Theory of pulsars - Polar caps, sparks, and coherent microwave radiation. *Astrophysical Journal* **196**, 51–72 (Feb. 1975).
25. Aharonian, F. A. *Very high energy cosmic gamma radiation : a crucial window on the extreme Universe* doi:10.1142/4657 (2004).
26. Stecker, F. W. The Production of Cosmic Gamma Rays in Interstellar and Intergalactic Cosmic-Ray Collisions. Iv: Gamma-Ray Production from Cosmic Proton-Antiproton Interactions. *SAO Special Report* **261** (Dec. 1967).

27. Domínguez, A. *et al.* Extragalactic background light inferred from AEGIS galaxy-SED-type fractions. *Monthly Notices of the RAS* **410**, 2556–2578 (Feb. 2011).
28. Franceschini, A. & Rodighiero, G. The extragalactic background light revisited and the cosmic photon-photon opacity. *Astronomy and Astrophysics* **603**, A34 (July 2017).
29. Moralejo, A. *et al.* Measurement of the EBL through a combined likelihood analysis of gamma-ray observations of blazars with the MAGIC telescopes in 35th International Cosmic Ray Conference (ICRC2017) **301** (Jan. 2017), 604. arXiv: 1709.02238 [astro-ph.HE].
30. Andernach, H. & Zwicky, F. English and Spanish Translation of Zwicky's (1933) The Redshift of Extragalactic Nebulae. *arXiv e-prints*, arXiv:1711.01693 (Nov. 2017).
31. Rubin, V. C., Ford, W. K. Jr. & Thonnard, N. Extended rotation curves of high-luminosity spiral galaxies. IV - Systematic dynamical properties, SA through SC. *Astrophysical Journal* **225**, L107–L111 (Nov. 1978).
32. Planck Collaboration *et al.* Planck 2013 results. XVI. Cosmological parameters. *Astronomy and Astrophysics* **571**, A16 (Nov. 2014).
33. Olive, K. A. TASI Lectures on Dark Matter. *arXiv e-prints*, astro-ph/0301505 (Jan. 2003).
34. Lisanti, M. *Lectures on Dark Matter Physics* in *New Frontiers in Fields and Strings (TASI 2015)* (Jan. 2017), 399–446. doi:10.1142/9789813149441\_0007. arXiv: 1603.03797 [hep-ph].
35. Kravtsov, A. V., Klypin, A. A., Bullock, J. S. & Primack, J. R. The Cores of Dark Matter-dominated Galaxies: Theory versus Observations. *Astrophysical Journal* **502**, 48–58 (July 1998).
36. Hernquist, L. An analytical model for spherical galaxies and bulges. *Astrophysical Journal* **356**, 359–364 (June 1990).
37. Zhao, H. Analytical models for galactic nuclei. *Monthly Notices of the RAS* **278**, 488–496 (Jan. 1996).
38. Navarro, J. F., Frenk, C. S. & White, S. D. M. The Structure of Cold Dark Matter Halos. *Astrophysical Journal* **462**, 563 (May 1996).
39. Einasto, J. On the Construction of a Composite Model for the Galaxy and on the Determination of the System of Galactic Parameters. *Trudy Astrofizicheskogo Instituta Alma-Ata* **5**, 87–100 (Jan. 1965).
40. Wakely, S. P. & Horan, D. TeVCat: An online catalog for Very High Energy Gamma-Ray Astronomy. *International Cosmic Ray Conference* **3**, 1341–1344 (2008).

41. Aliu, E. *et al.* Observation of Pulsed  $\gamma$ -Rays Above 25 GeV from the Crab Pulsar with MAGIC. *Science* **322**, 1221 (Nov. 2008).
42. Kuiper, L. *et al.* The Crab pulsar in the 0.75–30 MeV range as seen by CGRO COMPTEL. A coherent high-energy picture from soft X-rays up to high-energy gamma-rays. *Astronomy and Astrophysics* **378**, 918–935 (Nov. 2001).
43. McCann, A. Observations of the Crab Pulsar with VERITAS. *arXiv e-prints*, arXiv:1303.0275 (Mar. 2013).
44. Abdo, A. A. *et al.* Fermi Large Area Telescope Observations of the Crab Pulsar And Nebula. **708**, 1254–1267 (Jan. 2010).
45. Hirotani, K. High Energy Emission from Rotation-Powered Pulsars: Outer-gap vs. Slot-gap Models. *arXiv e-prints*, arXiv:0809.1283 (Sept. 2008).
46. Gajdus, M. *The Vela pulsar in very high energy gamma-rays with H.E.S.S. II* PhD thesis (Humboldt-Universität zu Berlin, Mathematisch-Naturwissenschaftliche Fakultät, 2016). doi:<http://dx.doi.org/10.18452/17610>.
47. Chandrasekhar, S. The Maximum Mass of Ideal White Dwarfs. *Astrophysical Journal* **74**, 81 (July 1931).
48. Osterbrock, D. E. & Ferland, G. J. *Astrophysics of gaseous nebulae and active galactic nuclei* (2006).
49. Weiler, K. W. & Sramek, R. A. Supernovae and supernova remnants. *Annual Review of Astron and Astrophys* **26**, 295–341 (Jan. 1988).
50. Becker Tjus, J., Eichmann, B., Kroll, M. & Nierstenhöfer, N. Gamma-ray emitting supernova remnants as the origin of Galactic cosmic rays? *Astroparticle Physics* **81**, 1–11 (Aug. 2016).
51. Cristofari, P., Gabici, S., Terrier, R. & Humensky, T. B. On the search for Galactic supernova remnant PeVatrons with current TeV instruments. **479**, 3415–3421 (Sept. 2018).
52. Gaensler, B. M. & Slane, P. O. The Evolution and Structure of Pulsar Wind Nebulae. *Annual Review of Astron and Astrophys* **44**, 17–47 (Sept. 2006).
53. H. E. S. S. Collaboration *et al.* HESS J1818-154, a new composite supernova remnant discovered in TeV gamma rays and X-rays. **562**, A40 (Feb. 2014).
54. Hewitt, J. W. & Lemoine-Goumard, M. Observations of supernova remnants and pulsar wind nebulae at gamma-ray energies. *Comptes Rendus Physique* **16**, 674–685 (Aug. 2015).
55. Dubus, G., Guillard, N., Petrucci, P.-O. & Martin, P. Sizing up the population of gamma-ray binaries. **608**, A59 (Dec. 2017).
56. Dubus, G. Gamma-ray binaries and related systems. *Astronomy and Astrophysics Reviews* **21**, 64 (Aug. 2013).

57. *Classical Novae* 2nd ed. doi:10.1017/CBO9780511536168 (Cambridge University Press, 2008).
58. Abdo, A. A., Ackermann, M., Ajello, M., Atwood & Fermi LAT Collaboration. Gamma-Ray Emission Concurrent with the Nova in the Symbiotic Binary V407 Cygni. *Science* **329**, 817–821 (Aug. 2010).
59. Ackermann, M. *et al.* Fermi establishes classical novae as a distinct class of gamma-ray sources. *Science* **345**, 554–558 (Aug. 2014).
60. Sitarek, J. & Bednarek, W. GeV-TeV gamma rays and neutrinos from the Nova V407 Cygni. *Physical Review D* **86**, 063011 (Sept. 2012).
61. Albert, J. *et al.* Observation of Gamma Rays from the Galactic Center with the MAGIC Telescope. **638**, L101–L104 (Feb. 2006).
62. H. E. S. S. Collaboration *et al.* The H.E.S.S. Galactic plane survey. **612**, A1 (Apr. 2018).
63. Archer, A. *et al.* TeV Gamma-Ray Observations of the Galactic Center Ridge by VERITAS. **821**, 129 (Apr. 2016).
64. Goldwurm, A. *An Overview of the High-Energy Emission from the Galactic Center in The Galactic Center: a Window to the Nuclear Environment of Disk Galaxies* (eds Morris, M. R., Wang, Q. D. & Yuan, F.) **439** (May 2011), 391. arXiv: 1007.4174 [astro-ph.HE].
65. Goldwurm, A. High energy activity of the super-massive black hole at the Galactic Center. *Comptes Rendus Physique* **8**, 35–44 (Jan. 2007).
66. Su, M., Slatyer, T. R. & Finkbeiner, D. P. Giant Gamma-ray Bubbles from Fermi-LAT: Active Galactic Nucleus Activity or Bipolar Galactic Wind? *Astrophysical Journal* **724**, 1044–1082 (Dec. 2010).
67. Ackermann, M. *et al.* The Spectrum and Morphology of the Fermi Bubbles. *Astrophysical Journal* **793**, 64 (Sept. 2014).
68. Abdo, A. A. *et al.* A population of gamma-ray emitting globular clusters seen with the Fermi Large Area Telescope. *Astronomy and Astrophysics* **524**, A75 (Dec. 2010).
69. H. E. S. S. Collaboration *et al.* Search for very-high-energy  $\gamma$ -ray emission from Galactic globular clusters with H.E.S.S. *Astronomy and Astrophysics* **551**, A26 (Mar. 2013).
70. Freire, P. C. C. *et al.* Fermi Detection of a Luminous -Ray Pulsar in a Globular Cluster. *Science* **334**, 1107–1110. ISSN: 0036-8075 (2011).
71. Wu, J. H. K. *et al.* SEARCH FOR PULSED  $\gamma$ -RAY EMISSION FROM GLOBULAR CLUSTER M28. *The Astrophysical Journal* **765**, L47 (Feb. 2013).
72. Tam, P.-H. T., Hui, C. Y. & Kong, A. K. H. Gamma-ray Emission from Globular Clusters. *Journal of Astronomy and Space Sciences* **33**, 1–11 (Mar. 2016).

73. Urry, C. M. & Padovani, P. Unified Schemes for Radio-Loud Active Galactic Nuclei. *Publications of the Astronomical Society of the Pacific* **107**, 803 (Sept. 1995).
74. Dermer, C. D. & Giebels, B. Active galactic nuclei at gamma-ray energies. *Comptes Rendus Physique* **17**, 594–616 (June 2016).
75. Madejski, G. G. & Sikora, M. Gamma-Ray Observations of Active Galactic Nuclei. **54**, 725–760 (Sept. 2016).
76. Wilson, A. S. & Colbert, E. J. M. The Difference between Radio-loud and Radio-quiet Active Galaxies. **438**, 62 (Jan. 1995).
77. Urry, C. M. & Padovani, P. Unified Schemes for Radio-Loud Active Galactic Nuclei. **107**, 803 (Sept. 1995).
78. Piran, T. The physics of gamma-ray bursts. *Reviews of Modern Physics* **76**, 1143–1210 (Oct. 2004).
79. Kouveliotou, C. *et al.* Identification of two classes of gamma-ray bursts. *Astrophysical Journal* **413**, L101–L104 (Aug. 1993).
80. Piran, T. Gamma-ray bursts and the fireball model. *Physics Reports* **314**, 575–667 (June 1999).
81. Ghirlanda, G., Bernardini, M., Calderone, G. & D’Avanzo, P. Are short Gamma Ray Bursts similar to long ones? *Journal of High Energy Astrophysics* **7**. Swift 10 Years of Discovery, a novel approach to Time Domain Astronomy, 81 –89. ISSN: 2214-4048 (2015).
82. .
83. Ajello, M. *et al.* Fermi-LAT Observations of LIGO/Virgo Event GW170817. **861**, 85 (July 2018).
84. Mirzoyan, R. First time detection of a GRB at sub-TeV energies; MAGIC detects the GRB 190114C. *The Astronomer’s Telegram* **12390** (Jan. 2019).
85. Ohm, S. Starburst galaxies as seen by gamma-ray telescopes. *Comptes Rendus Physique* **17**, 585–593 (June 2016).
86. Acero, F. *et al.* Detection of Gamma Rays from a Starburst Galaxy. *Science* **326**, 1080 (Nov. 2009).
87. VERITAS Collaboration *et al.* A connection between star formation activity and cosmic rays in the starburst galaxy M82. *Nature* **462**, 770–772 (Dec. 2009).
88. Abdo, A. A. *et al.* Detection of Gamma-Ray Emission from the Starburst Galaxies M82 and NGC 253 with the Large Area Telescope on Fermi. *Astrophysical Journal* **709**, L152–L157 (Feb. 2010).
89. Brunetti, G. Gamma rays from galaxy clusters. *AIP Conference Proceedings* **1792**, 020009 (2017).

90. Brunetti, G. & Jones, T. W. Cosmic Rays in Galaxy Clusters and Their Nonthermal Emission. *International Journal of Modern Physics D* **23**, 1430007–98 (Mar. 2014).
91. Ackermann, M. *et al.* GeV Gamma-ray Flux Upper Limits from Clusters of Galaxies. *Astrophysical Journal* **717**, L71–L78 (July 2010).
92. Aleksić, J. *et al.* Constraining cosmic rays and magnetic fields in the Perseus galaxy cluster with TeV observations by the MAGIC telescopes. *Astronomy and Astrophysics* **541**, A99 (May 2012).
93. Xi, S.-Q. *et al.* Detection of gamma-ray emission from the Coma cluster with Fermi Large Area Telescope and tentative evidence for an extended spatial structure. *Physical Review D* **98**, 063006 (Sept. 2018).
94. Czerny, B. *et al.* Astronomical Distance Determination in the Space Age. Secondary Distance Indicators. *Space Science Reviews* **214**, 32 (Feb. 2018).
95. Rezaeikh, S., Javadi, A., Khosroshahi, H. & van Loon, J. T. The star formation history of the Magellanic Clouds derived from long-period variable star counts. *Monthly Notices of the RAS* **445**, 2214–2222 (Dec. 2014).
96. Robitaille, T. P. & Whitney, B. A. The Present-Day Star Formation Rate of the Milky Way Determined from Spitzer-Detected Young Stellar Objects. *Astrophysical Journal* **710**, L11–L15 (Feb. 2010).
97. Sreekumar, P. *et al.* Observations of the Large Magellanic Cloud in High-Energy Gamma Rays. *Astrophysical Journal* **400**, L67 (Dec. 1992).
98. Abdo, A. A. *et al.* Detection of the Small Magellanic Cloud in gamma-rays with Fermi/LAT. *Astronomy and Astrophysics* **523**, A46 (Nov. 2010).
99. Abdo, A. A. *et al.* Observations of the Large Magellanic Cloud with Fermi. *Astronomy and Astrophysics* **512**, A7 (Mar. 2010).
100. Ackermann, M. *et al.* Deep view of the Large Magellanic Cloud with six years of Fermi-LAT observations. *Astronomy and Astrophysics* **586**, A71 (Feb. 2016).
101. Corbet, R. H. D. *et al.* A Luminous Gamma-ray Binary in the Large Magellanic Cloud. *Astrophysical Journal* **829**, 105 (Oct. 2016).
102. H. E. S. S. Collaboration *et al.* The exceptionally powerful TeV  $\gamma$ -ray emitters in the Large Magellanic Cloud. *Science* **347**, 406–412 (Jan. 2015).
103. Komin, N. *et al.* H.E.S.S. observations of the Large Magellanic Cloud. *arXiv e-prints*, arXiv:1201.0639 (Jan. 2012).
104. Ackermann, M. *et al.* Observations of M31 and M33 with the Fermi Large Area Telescope: A Galactic Center Excess in Andromeda? *Astrophysical Journal* **836**, 208 (Feb. 2017).
105. Navarro, J. F. The Structure of Cold Dark Matter Halos. *Symposium - International Astronomical Union* **171**, 255–258 (1996).

106. Cherenkov Telescope Array Consortium *et al.* *Science with the Cherenkov Telescope Array* doi:10.1142/10986 (2019).
107. Abramowski, A. *et al.* Search for a Dark Matter Annihilation Signal from the Galactic Center Halo with H.E.S.S. *Physical Review Letters* **106**, 161301 (Apr. 2011).
108. Aharonian, F. *et al.* HESS Observations of the Galactic Center Region and Their Possible Dark Matter Interpretation. *Physical Review Letters* **97**, 221102 (Dec. 2006).
109. Ackermann, M. *et al.* The Fermi Galactic Center GeV Excess and Implications for Dark Matter. *Astrophysical Journal* **840**, 43 (May 2017).
110. Kuhlen, M, Diemand, J, Madau, P & Zemp, M. The Via Lactea INCITE simulation: galactic dark matter substructure at high resolution. *Journal of Physics: Conference Series* **125**, 012008 (July 2008).
111. Simon, J. D. & Geha, M. The Kinematics of the Ultra-faint Milky Way Satellites: Solving the Missing Satellite Problem. *Astrophysical Journal* **670**, 313–331 (Nov. 2007).
112. Abdo, A. A. *et al.* Observations of Milky Way Dwarf Spheroidal Galaxies with the Fermi-Large Area Telescope Detector and Constraints on Dark Matter Models. *Astrophysical Journal* **712**, 147–158 (Mar. 2010).
113. Abramowski, A. *et al.* Search for dark matter annihilation signatures in H.E.S.S. observations of dwarf spheroidal galaxies. *Physical Review D* **90**, 112012 (Dec. 2014).
114. Ahnen, M. L. *et al.* Indirect dark matter searches in the dwarf satellite galaxy Ursa Major II with the MAGIC telescopes. *Journal of Cosmology and Astroparticle Physics* **2018**, 009 (Mar. 2018).
115. Archambault, S. *et al.* Dark matter constraints from a joint analysis of dwarf Spheroidal galaxy observations with VERITAS. *Physical Review D* **95**, 082001 (Apr. 2017).
116. Oakes, L. *Combined Dark Matter Searches Towards Dwarf Spheroidal Galaxies with Fermi-LAT, HAWC, HESS, MAGIC and VERITAS* in *36th International Cosmic Ray Conference (ICRC2019)* **36** (July 2019), 539. arXiv: 1909.06310 [astro-ph.HE].
117. Cirelli, M., Moulin, E., Panci, P., Serpico, P. D. & Viana, A. Gamma ray constraints on decaying dark matter. *Physical Review D* **86**, 083506 (Oct. 2012).
118. Huang, X., Vertongen, G. & Weniger, C. Probing dark matter decay and annihilation with Fermi LAT observations of nearby galaxy clusters. *Journal of Cosmology and Astroparticle Physics* **2012**, 042 (Jan. 2012).

119. Ackermann, M. *et al.* Constraints on dark matter annihilation in clusters of galaxies with the Fermi large area telescope. *Journal of Cosmology and Astroparticle Physics* **2010**, 025 (May 2010).
120. Abramowski, A. *et al.* Search for Dark Matter Annihilation Signals from the Fornax Galaxy Cluster with H.E.S.S. *Astrophysical Journal* **750**, 123 (May 2012).
121. Acciari, V. A. *et al.* Constraining dark matter lifetime with a deep gamma-ray survey of the Perseus galaxy cluster with MAGIC. *Physics of the Dark Universe* **22**, 38–47 (Dec. 2018).
122. van der Marel, R. P. *The Large Magellanic Cloud: structure and kinematics* in *The Local Group as an Astrophysical Laboratory* (eds Livio, M. & Brown, T. M.) **17** (Jan. 2006), 47–71. arXiv: astro-ph/0404192 [astro-ph].
123. Sofue, Y. Dark Bulge, Exponential Disk, and Massive Halo in the Large Magellanic Cloud. *Publications of the Astronomical Society of Japan* **51**, 445–448. ISSN: 0004-6264 (Aug. 1999).
124. Buckley, M. R. *et al.* Search for gamma-ray emission from dark matter annihilation in the large magellanic cloud with the fermi large area telescope. *Physical Review D* **91**, 102001 (May 2015).
125. *IBIS homepage* <https://www.cosmos.esa.int/web/integral/instruments-ibis>.
126. *INTEGRAL homepage* <https://sci.esa.int/web/integral/home>.
127. Atwood, W. B. *et al.* The Large Area Telescope on the Fermi Gamma-Ray Space Telescope Mission. *Nature* **697**, 1071–1102 (June 2009).
128. Ackermann, M. *et al.* Detection of the Characteristic Pion-Decay Signature in Supernova Remnants. *Science* **339**, 807–811 (Feb. 2013).
129. Ackermann, M. *et al.* Fermi-LAT Observations of the Gamma-Ray Burst GRB 130427A. *Science* **343**, 42–47 (Jan. 2014).
130. Goldstein, A. *et al.* An Ordinary Short Gamma-Ray Burst with Extraordinary Implications: Fermi-GBM Detection of GRB 170817A. *The Astrophysical Journal* **848**, L14 (Oct. 2017).
131. Heitler, W. *Quantum theory of radiation* (1954).
132. Rossi, B. & Greisen, K. Cosmic-Ray Theory. *Rev. Mod. Phys.* **13**, 240–309 (4 Oct. 1941).
133. Vallejo, I. O. *Observation of active galactic [sic] nuclei with the Magic telescope* Tesis de la Universidad Complutense de Madrid, Facultad de Ciencias Físicas, Departamento de Física Atómica, Molecular y Nuclear, leída el 23-06-2010. PhD thesis (Madrid, Oct. 2010). <<https://eprints.ucm.es/11431/>>.

134. Collado, T. H. *Sensitivity studies for the Cherenkov Telescope Array* Tesis inédita de la Universidad Complutense de Madrid, Facultad de Ciencias Físicas, Departamento de Física Atómica, Molecular y Nuclear, leída el 28-09-2015. Madrid, Jan. 2016. <<https://eprints.ucm.es/35143/>>.
135. Gaisser, T. K., Engel, R. & Resconi, E. *Cosmic Rays and Particle Physics* (June 2016).
136. Jelley, J. *Čerenkov radiation, and its applications* <<https://books.google.es/books?id=uzzRAAAAMAAJ>> (Pergamon Press, 1958).
137. Borione, A. *et al.* CASA-MIA: A precision” EAS detector. [Cyg X-3; Her X-1; M1; NGC 1952; PSR 0531+21]. doi:10.1063/1.43832 (June 1993).
138. Di Sciascio, G. & LHAASO Collaboration. The LHAASO experiment: From Gamma-Ray Astronomy to Cosmic Rays. *Nuclear and Particle Physics Proceedings* **279**, 166–173 (Oct. 2016).
139. Huo, X. A. *et al.* *Tibet-AS*  $\gamma$  Experiment in *International Cosmic Ray Conference* **2** (Jan. 1990), 427.
140. Fonseca, V. The HEGRA experiment (High Energy Gamma Ray Array). *Nuclear Physics B - Proceedings Supplements* **28**, 409 –412. ISSN: 0920-5632 (1992).
141. Di Sciascio, G. A.-Y. C. *Latest results from the ARGO-YBJ experiment* in *Journal of Physics Conference Series* **632** (Aug. 2015), 012089. doi:10.1088/1742-6596/632/1/012089. arXiv: 1503.09102 [astro-ph.HE].
142. Mostafá, M. A. The High-Altitude Water Cherenkov Observatory. *Brazilian Journal of Physics* **44**, 571–580 (Oct. 2014).
143. Arqueros, F. *et al.* The Wide Angle Air Cherenkov Detector AIROBICC at La Palma (Aug. 1996).
144. Hillas, A. M. *Cerenkov light images of EAS produced by primary gamma* in *19th International Cosmic Ray Conference (ICRC19), Volume 3* (ed Jones, F. C.) **3** (Aug. 1985).
145. de Naurois, M. Analysis methods for Atmospheric Cerenkov Telescopes. *arXiv e-prints*, astro-ph/0607247 (July 2006).
146. de Naurois, M. & Mazin, D. Ground-based detectors in very-high-energy gamma-ray astronomy. *Comptes Rendus Physique* **16**, 610–627 (Aug. 2015).
147. Kildea, J. *et al.* The Whipple Observatory 10 m gamma-ray telescope, 1997-2006. English (US). *Astroparticle Physics* **28**, 182–195. ISSN: 0927-6505 (Oct. 2007).
148. Cortina, J. *Highlights of the MAGIC telescopes* in *International Cosmic Ray Conference* **11** (Jan. 2011), 147. doi:10.7529/ICRC2011/V12/H12. arXiv: 1110.4747 [astro-ph.HE].
149. Pühlhofer, G. H.E.S.S. highlights. *arXiv e-prints*, arXiv:1801.06074 (Jan. 2018).

150. Furniss, A. *Recent Highlights from the VERITAS Gamma-ray Observatory* in *American Astronomical Society Meeting Abstracts #233* **233** (Jan. 2019), 433.04.
151. *MAGIC homepage* <https://magic.mpp.mpg.de/>.
152. *CTA Performance* <https://www.cta-observatory.org/science/cta-performance/>.
153. *CTA Observatory site* <https://www.cta-observatory.org/>.
154. Acharya, B. *et al.* Introducing the CTA concept. *Astroparticle Physics* **43**. Seeing the High-Energy Universe with the Cherenkov Telescope Array - The Science Explored with the CTA, 3 –18. ISSN: 0927-6505 (2013).
155. Bernlöhr, K. *et al.* Monte Carlo design studies for the Cherenkov Telescope Array. *Astroparticle Physics* **43**, 171–188 (Mar. 2013).
156. Hassan, T. *et al.* Monte Carlo performance studies for the site selection of the Cherenkov Telescope Array. *Astroparticle Physics* **93**, 76–85 (July 2017).
157. Maier, G. *et al.* *Performance of the Cherenkov Telescope Array* in *35th International Cosmic Ray Conference (ICRC2017)* **301** (Jan. 2017), 846. arXiv: 1709.01381 [astro-ph.IM].
158. Ambrosi, G. *et al.* The Cherenkov Telescope Array Large Size Telescope. *arXiv e-prints*, arXiv:1307.4565 (July 2013).
159. Mazin, D., Cortina, J. & Teshima, M. *Large size telescope report* in *6th International Symposium on High Energy Gamma-Ray Astronomy* **1792** (Jan. 2017), 080001. doi:10.1063/1.4969022. arXiv: 1610.04403 [astro-ph.IM].
160. Delgado, C. *et al.* Mechanics and cooling system for the camera of the Large Size Telescopes of the Cherenkov Telescope Array (CTA). *arXiv e-prints*, arXiv:1307.4540 (July 2013).
161. Nieto, D. *et al.* Prototype 9.7 m Schwarzschild-Couder telescope for the Cherenkov Telescope Array: status of the optical system. *arXiv e-prints*, arXiv:1709.06324 (Sept. 2017).
162. Glicenstein, J. F. *Status of the Davies Cotton and Schwarzschild-Coude Medium Sized Telescopes for the Cherenkov Telescope Array* in *36th International Cosmic Ray Conference (ICRC2019)* **36** (July 2019), 269. arXiv: 1907.08455 [astro-ph.IM].
163. Garczarczyk, M., Schlenstedt, S., Oakes, L., Schwanke, U. & the MST Team. Status of the Medium-Sized Telescope for the Cherenkov Telescope Array. *arXiv e-prints*, arXiv:1509.01361 (Sept. 2015).

164. Barrio, J. Status of the large size telescopes and medium size telescopes for the Cherenkov Telescope Array observatory. *Nuclear Instruments and Methods in Physics Research Section A: Accelerators, Spectrometers, Detectors and Associated Equipment*. ISSN: 0168-9002. doi:<https://doi.org/10.1016/j.nima.2018.11.047>. <<http://www.sciencedirect.com/science/article/pii/S016890021831622X>> (2018).
165. Maccarone, M. C. & Astri Project, C. *ASTRI for the Cherenkov Telescope Array* in *35th International Cosmic Ray Conference (ICRC2017)* **301** (Jan. 2017), 855. arXiv: 1709.03078 [astro-ph.IM].
166. Tibaldo, L. *et al.* *The gamma-ray Cherenkov telescope for the Cherenkov telescope array* in *6th International Symposium on High Energy Gamma-Ray Astronomy* **1792** (Jan. 2017), 080004. doi:10.1063/1.4969025. arXiv: 1610.01398 [astro-ph.IM].
167. Samarai, I. A. *et al.* *Performance of a small size telescope (SST-1M) camera for gamma-ray astronomy with the Cherenkov Telescope Array* in *35th International Cosmic Ray Conference (ICRC2017)* **301** (Jan. 2017), 758. arXiv: 1709.03914 [astro-ph.IM].
168. White, R. & Schoorlemmer, H. A Compact High Energy Camera (CHEC) for the Gamma-ray Cherenkov Telescope of the Cherenkov Telescope Array. *arXiv e-prints*, arXiv:1709.05799 (Sept. 2017).
169. Pareschi, G. *et al.* The dual-mirror Small Size Telescope for the Cherenkov Telescope Array. *arXiv e-prints*, arXiv:1307.4962 (July 2013).
170. Funk, S. *et al.* *TARGET: A digitizing and trigger ASIC for the Cherenkov telescope array* in *6th International Symposium on High Energy Gamma-Ray Astronomy* **1792** (Jan. 2017), 080012. doi:10.1063/1.4969033. arXiv: 1610.01536 [astro-ph.IM].
171. Heck, D., Knapp, J., Capdevielle, J. N., Schatz, G. & Thouw, T. *CORSIKA: a Monte Carlo code to simulate extensive air showers*. (1998).
172. Klages, H. *et al.* The Kascade experiment. *Nuclear Physics B - Proceedings Supplements* **52**, 92 –102. ISSN: 0920-5632 (1997).
173. Ostapchenko, S. QGSJET-II: towards reliable description of very high energy hadronic interactions. *Nuclear Physics B Proceedings Supplements* **151**, 143–146 (2006).
174. Schmidt, F. & Knapp, J. *CORSIKA Shower Images*
175. Bernlöhr, K. Simulation of imaging atmospheric Cherenkov telescopes with CORSIKA and sim\_telarray. *Astroparticle Physics* **30**, 149–158 (Oct. 2008).
176. *Ctpipe webpage* <https://cta-observatory.github.io/ctpipe/index.html>.

177. Contreras, J. L. *et al.* *Data model issues in the Cherenkov Telescope Array project* in *34th International Cosmic Ray Conference (ICRC2015)* **34** (2015), 960. arXiv: 1508.07584 [astro-ph.IM].
178. Knödlseder, J. *et al.* GammaLib and ctools. A software framework for the analysis of astronomical gamma-ray data. **593**, A1 (2016).
179. Iori, M. *et al.* Design of a prototype device to calibrate the Large Size Telescope camera of the Cherenkov Telescope Array. *arXiv e-prints*, arXiv:1508.06752 (Aug. 2015).
180. Palatiello, M., Iori, M., Cassol, F., Cauz, D. & Ferrarotto, F. Performance of the INFN Camera calibration device of the first Large Size Telescope in the Cherenkov Telescope Array. *arXiv e-prints*, arXiv:1909.08475 (Sept. 2019).
181. Mirzoyan, R. *On the Calibration Accuracy of Light Sensors in Atmospheric Cherenkov Fluorescence and Neutrino Experiments* in *International Cosmic Ray Conference* **7** (Jan. 1997), 265.
182. Parsons, R. D. & Ohm, S. Background Rejection in Atmospheric Cherenkov Telescopes using Recurrent Convolutional Neural Networks. *arXiv e-prints*, arXiv:1910.09435 (Oct. 2019).
183. Shayduk, M. & Consortium, C. *Optimized Next-neighbour Image Cleaning Method for Cherenkov Telescopes* in *International Cosmic Ray Conference* **33** (2013), 3000. arXiv: 1307.4939 [astro-ph.IM].
184. Shayduk, M., Hengstebeck, T., Kalekin, O. R., Pavel, N. A. & Schweizer, T. *A New Image Cleaning Method for the MAGIC Telescope* in (2005).
185. Lessard, R., Cayón, L., Sembroski, G. & Gaidos, J. Wavelet Imaging Cleaning Method for Atmospheric Cherenkov Telescopes. *Astroparticle Physics* **17**. doi:10.1016/S0927-6505(01)00173-6 (Oct. 2001).
186. HEGRA Collaboration: A. Daum. First Results on the Performance of the HEGRA IACT Array. *arXiv e-prints*, astro-ph/9704098 (Apr. 1997).
187. Fomin, V. P. *et al.* New methods of atmospheric Cherenkov imaging for gamma-ray astronomy. I. The false source method. *Astroparticle Physics* **2**, 137–150 (May 1994).
188. Domingo-Santamaría, E. *The DISP analysis method for point-like or extended gamma source searches/studies with the MAGIC Telescope* in (2005).
189. Pedregosa, F. *et al.* Scikit-learn: Machine Learning in Python. *Journal of Machine Learning Research* **12**, 2825–2830 (2011).
190. Li, T. P. & Ma, Y. Q. Analysis methods for results in gamma-ray astronomy. **272**, 317–324 (Sept. 1983).
191. Aharonian, F. *et al.* The Crab Nebula and Pulsar between 500 GeV and 80 TeV: Observations with the HEGRA Stereoscopic Air Cerenkov Telescopes. **614**, 897–913 (Oct. 2004).

192. Sanuki, T. *et al.* Precise Measurement of Cosmic-Ray Proton and Helium Spectra with the BESS Spectrometer. **545**, 1135–1142 (Dec. 2000).
193. Dempster, A. P., Laird, N. M. & Rubin, D. B. Maximum Likelihood from Incomplete Data via the EM Algorithm. *Journal of the Royal Statistical Society. Series B (Methodological)* **39**, 1–38. ISSN: 00359246 (1977).